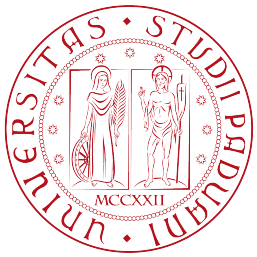

DIPARTIMENTO DI INGEGNERIA DELL'INFORMAZIONE

CORSO DI LAUREA MAGISTRALE IN INGEGNERIA ELETTRONICA

Synergistic effects of total ionizing dose and displacement damage on bipolar and BiCMOS circuits in high energy physics applications

University Supervisor:
Prof. Alessandro Paccagnella
University Co-supervisor:
Dott. Stefano Bonaldo
CERN Supervisors:
Dott. Rudy Ferraro
Dott. Salvatore Danzeca

Student:
Gabriele Andreetta
Number:
2053121

Academic Year 2023/2024

Date: 3 September 2024

Contents

Abstract

English

At CERN, the functionality of the accelerators complex depends significantly on the reliability of electronic control devices. The environment inside the structures hosting particle accelerators is particularly hostile to electronic components due to the presence of ionizing and non-ionizing radiation, as well as high-energy particles, which degrade the performance of devices. Ionizing radiation induces charge trapping in gate oxide and dielectric materials with possible formation of interface traps at the oxide/semiconductor interface. Non-ionizing radiation, such as neutrons, displaces semiconductor atoms within the crystal lattice, thus generating punctual or cluster of defects. Additionally, high-energy particles induce the formation of charge in sensitive regions of devices, which can lead to single-event effects. In these challenging environments, the high demand for components and the prohibitive cost of rad-hard solutions have led to the widespread use of Commercial Off-The-Shelf (COTS) systems. However, these systems must be qualified to ensure their tolerance to radiation.

In certain applications, bipolar devices are preferred over CMOS devices due to their resilience to latchup, a destructive event that compromises the functionality of CMOS systems. Nonetheless, bipolar devices suffer from displacement damage, which is typically negligible in MOSFETs. Consequently, the combination of ionizing and non-ionizing radiation can produce synergistic effects in bipolar devices, where the overall damage cannot be predicted by simply summing the individual contributions of each radiation type. These effects complicate the qualification of highly distributed systems within the Large Hadron Collider (LHC), as radiation levels vary significantly in terms of the ratio between displacement damage and total ionizing dose.

In this thesis I investigate the synergistic effects of ionizing and non-ionizing radiation on various types of bipolar and BiCMOS integrated circuits. I also explore the impact of these effects on the radiation qualification of components for highly distributed systems in the LHC.

Italiano

Al CERN, la funzionalità del complesso di acceleratori dipende in modo significativo dall'affidabilità dei dispositivi elettronici di controllo. L'ambiente all'interno delle strutture che ospitano gli acceleratori di particelle è particolarmente ostile ai componenti elettronici a causa della presenza di radiazioni ionizzanti e non ionizzanti, nonché di particelle ad alta energia, che degradano le prestazioni dei dispositivi. Le radiazioni ionizzanti inducono intrappolamento di carica nell'ossido di gate e nei materiali dielettrici con possibile formazione di trappole all'interfaccia tra ossido e semiconduttore. Le radiazioni non ionizzanti, come i neutroni, spostano gli atomi dei semiconduttori all'interno del reticolo cristallino, generando così difetti puntuali o a grappolo. Inoltre, le particelle ad alta energia inducono la formazione di cariche nelle regioni sensibili dei dispositivi, il che può portare a effetti da evento singolo. In questi ambienti difficili, l'elevata domanda di componenti e il costo proibitivo delle soluzioni rad-hard hanno portato all'uso diffuso di sistemi COTS (Commercial Off-The-Shelf). Tuttavia, questi sistemi devono essere qualificati per garantire la loro tolleranza alle radiazioni.
In alcune applicazioni, i dispositivi bipolari sono preferiti rispetto ai dispositivi CMOS a causa della loro resistenza ai latchup, eventi distruttivi che compromettono la funzionalità dei sistemi CMOS. Tuttavia, i dispositivi bipolari soffrono di danni da spostamento, che in genere sono trascurabili nei MOSFET. Di conseguenza, la combinazione di radiazioni ionizzanti e non ionizzanti può produrre effetti sinergici nei dispositivi bipolari, dove il danno complessivo non può essere previsto semplicemente sommando i contributi individuali di ciascun tipo di radiazione. Questi effetti complicano la qualificazione di sistemi altamente distribuiti all'interno del Large Hadron Collider (LHC), poiché i livelli di radiazione variano significativamente in termini di rapporto tra danno da spostamento e dose ionizzante.
In questa tesi mi propongo di indagare gli effetti sinergici delle radiazioni ionizzanti e non ionizzanti su vari tipi di circuiti integrati bipolari e BiCMOS. Inoltre miro a esplorare l'impatto di questi effetti sulla qualificazione dei componenti per i sistemi altamente distribuiti nell'LHC.

Introduction

At the European Organization for Nuclear Research (CERN), scientists and engineers are working at the boundaries of the physics research, the huge system of particle accelerators allows the scientist to push the limit of the knowledge exploring the elementary particles that constitute the universe.
From its foundation in 1954, CERN has continuously expanded its number of accelerators to further investigate the secrets of the nuclear and subnuclear physics. The current state of the accelerators complex is shown in Figure 1.

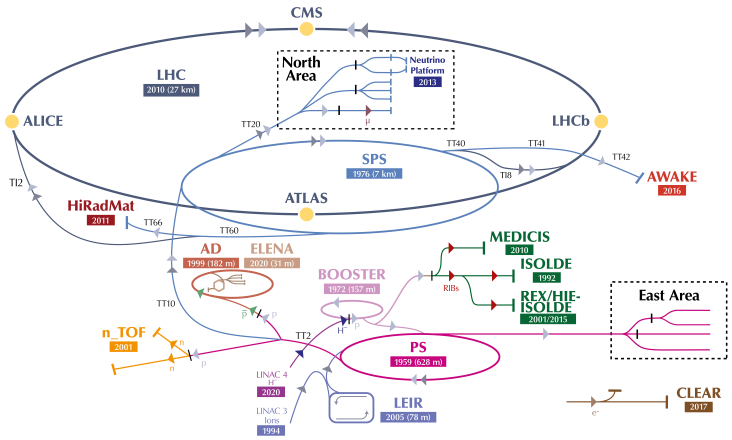

Figure 1: CERN accelerators complex.

The Large Hadron Collider represents the most important and powerful accelerator of CERN. It was inaugurated in 2008 and, with a circumference of 27 km, it can held 7 TeV of proton beam energy, resulting in 14 TeV collision energy. One of the objectives of the LHC was the demonstration of the Higgs Boson existence. In 2012 the analysis of the data coming from the two main experiments, ATLAS and CMS, leads to the Higgs Boson discover and to the Nobel Price in Physics for Peter Higgs and François Englert.
From 2026 to 2028 there will be a long shutdown during which all the systems and experiments of the LHC will be updated to handle the High Luminosity LHC update (HL-LHC). The increase of the luminosity consists in the increase of the number of collisions maintaining the same beam energy [1], as a consequence, more events will be detected.
But there is another ambitious upgrade of the accelerators complex that the CERN community wants to push forward: the Future Circular Collider (FCC). In these years the feasibility studies for the FCC are been carried out. This accelerator, with a 90.7 km circumference, is aimed at producing Higgs bosons and holding even higher energy beams (up to 100 TeV of collision energy). After the council of member states permission, it will be built in the French-Swiss border [2].

Because of the proton and ion beams accelerated inside the pipes of the LHC, the environ-

ment of the tunnels is highly radioactive. Beam-beam collisions and beam losses (maily due to beam-gas interactions) create debris and make the environment full of neutrons, hadrons and ions. As a consequence, electronic systems located in the tunnel and close to the interaction points are subjected to ionizing and non-ionizing radiations that lead to the degradation of the components. For this reason, in the last years a lot of efforts have been made to develop solid radiation hardness qualification procedure to assess the degradation profiles of components and systems and to make sure that the systems installed in the LHC are radiation tolerant.
While electronic devices in CMOS technology are intrinsically tolerant to the cumulative effects of non-ionizing radiations, they are subjected to both cumulative effects and single event effects of ionizing radiations. Therefore, they are sensitive to latchups: destructive single events caused by high energy particles. For this reason, in certain applications the bipolar technology is still used. In fact, bipolar devices are intrinsically tolerant to single event effects and to destructive events. On the other hand, they are sensitive to both ionizing and non-ionizing cumulative effects and to their synergy.
This issue gains more importance considering the distributed nature of the systems in the LHC. Since the radiation levels inside the LHC can vary enormously along the circumference of the accelerator, electronic systems can be subjected to different radiation levels in terms of total dose accumulated and ratio between ionizing dose (TID) and non-ionizing dose (DDEF). For example, the locations close to the experiments are very radioactive, in those locations only rad-hard devices can survive. While in the tunnel (locations called ARCS) the radiation levels are lower and qualified Commercial Off-The-Shelf (COTS) devices can be used. Concerning the ratio, there are points in the LHC where, for the same amount of total ionizing dose, the displacement damage (in terms of equivalent 1MeV neutron fluence) is ten times higher.
Thus, during qualification of bipolar devices, considering only one scenario in terms of DDEF/TID or taking into account only one major contributor for the damage and applying margins are not representative of the real degradation in operation, it can lead to discard COTS that could be used in the accelerator systems or, in the worst case, to the qualification of devices that will not tolerate the particular environment in which they will operate.

Within this context, my thesis aims at achieving two main objectives. The first is to demonstrate the sensitivity of bipolar and BiCMOS integrated circuits to synergistic effects of TID and DD by evaluating the responses of the devices when exposed to mixed radiation fields with controlled DDEF/TID ratios. The second objective is to explore the impact of this sensitivity to the CERN radiation hardness assurance.

This work is structured in the following chapters: in the first chapter the radiation effects to electronics are discussed and the synergistic TID/DD effects are introduced. The second chapter is focused on the CERN radiation environment highlighting the variability of the radiation levels around the LHC, a brief explanation of the CERN radiation hardness assurance (RHA) procedure is provided and finally the components I selected for the study are discussed. The third chapter is about the test campaigns organization: the selection of the test circuits, the production of the boards I designed, the explanation of the irradiation facilities and the test setups I prepared. In the fourth chapter I analyze the test results and the impact of the synergistic effects on the RHA.

Chapter 1

Radiation Effects on Electronics

The performances of electronic systems are strongly affected by radiations, the effects in the devices depends on multiple factors: the type and the energy of the impinging particles, the material of the device and the technology.
This chapter will provide the basic concepts underlying the radiation effects on electronic devices, from the types of radiation-matter interactions to the different effects of those interactions inside the devices.

1.1 Radiation Matter Interaction

The first factors that determine the effects of radiations in electronic devices are the energy and the type of impinging particles. Particles can be divided into three groups: photons, electrically charged particles and neutrons. The different possible interactions are illustrated in Figure 1.1 [3].
There are three main interacting mechanisms between photons and matter:

- Photoelectric effect: all the energy of the photon is transferred to an electron that is ejected from the atom.
- Compton effect: if the energy of the photon is higher than the energy needed for the ejection of the electron, the electron is ejected, but the photon is scattered with the remaining energy.
- Pair production: if the photon has high energy ($> 1\ MeV$) and passes close to the nucleus, the photon may release all the energy in the production of an electron-positron pair.

Neutral particles interact with matter in four ways:

- Absorption: if the incident neutron has low energy (i.e. thermal neutrons $25\ meV$), it can be absorbed by the nucleus of the interacting atom that became excited, the atom de-excitation causes the emission of photons.
- Fission: the energetic neutron causes the splitting of a nucleus of the material, this reaction releases a large amount of energy and causes the emission of fragments, neutrons and photons.
- Inelastic scattering: the collision between a neutron and a nucleus results in the scattering of both elements.

- Elastic scattering: the incident neutron is absorbed by the recoiling nucleus, which emits a neutron with a lower kinetic energy that leaves in an excited state, and then emits one or more photons.

Finally, charge particles interact mainly in three ways:

- Bremsstrahlung: if an electron passes close to the nucleus it is deflected and part of its kinetic energy is transformed to photon emission.
- Ionization: the coulombic interaction between the charged particle and the electron of the atom causes the ejection of the electron from its orbital.
- Excitation: if the energy of the charged particle is not enough to eject the electron, but it is enough to make it move in different atomic shells, the electron is excited and then the de-excitation causes the photon emission.

In addition to these last mechanisms, heavy charged particles, such as ions or protons, are involved also in nuclear interactions. Furthermore, secondary particles, photons, fragments or neutrons, can interact with matter causing a cascade of interactions.

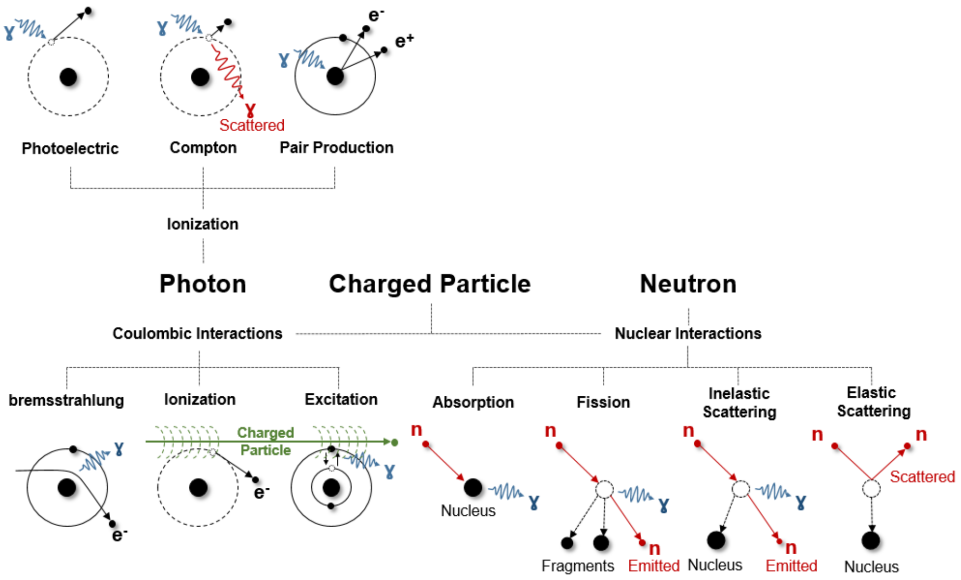

Figure 1.1: Radiation-matter interactions [3]

The result of all these interactions is the energy transfer from the impinging particle to the material and can be defined ionizing or non-ionizing depending on the mechanisms involved. The Ionizing Energy Transfer (IEL), or Linear Energy Transfer (LET), and the Non-Ionizing Energy Loss (NIEL) are used to quantify the energy loss along the particle's path due to ionizing and non-ionizing interactions respectively. LET and NIEL are reported in Equations 1.1 and 1.2.

$$LET = \frac{1}{\rho}\frac{dE}{dx}\bigg|_e \left[\frac{MeV \cdot cm^2}{g}\right] \tag{1.1}$$

$$NIEL = \frac{1}{\rho}\frac{dE}{dx}\bigg|_n \left[\frac{MeV \cdot cm^2}{g}\right] \tag{1.2}$$

1.2 Radiation Effects on Electronics

The effects of the ionizing and non-ionizing energy transfers inside a semiconductor device can be further divided into two categories: cumulative effects and Single Event Effects (SEEs). Cumulative effects cause a gradual drift of the performances, while the SEEs are stochastic effects that in some situation can cause the permanent damage of the device. In this paragraph all these effects will be discussed, with a particular focus on the cumulative effects that are the main object of this thesis.

1.2.1 Total Ionizing Dose

The Total Ionizing Dose (TID) is a cumulative effect defined as the amount of energy absorbed per unit of mass due to coulombic interactions and it is measured in gray (Gy). One gray is equivalent to one joule absorbed in one kilogram of matter. However, in the space sector another unit of measurement is commonly used: the rad, which corresponds to 0.01 Gy.

$$TID = \left.\frac{dE}{dm}\right|_e [Gy] \tag{1.3}$$

Since TID depends only on the energy released by the particles in the medium, it depends on the particles Linear Energy Transfer. In a radiation field composed by many particles, the total dose is calculated with Equation 1.4. It is equal to the sum of the contributions of each particle type obtained by multiplying the LET by the number of particles per unit of area (fluence, Φ) evaluated in the entire energy spectrum of the particle.

$$TID = \sum_p \int LET(p,E)\frac{d\Phi(p,E)}{dE}dE\ [Gy] \tag{1.4}$$

The degradation due to TID, depicted in Figure 1.2, is a consequence of the ionization of the oxide materials in the electronic devices and the consequent charge trapping inside the oxide. When a charged particle passes through the oxide a large number of electron-hole pairs are generated, if the oxide is subjected to electric fields, the electrons and the holes are separated and positive charges are trapped in the oxide. Trapping of positive charges happens due to the lower diffusion velocity of the holes and the presence of defects in the oxide. In fact, it occurs mainly in presence of oxygen vacancies where the Si-Si bond is weak and can trap holes creating a positive charged E' center.

In addition, the radiation can release the hydrogen ions whose presence is due to oxidation

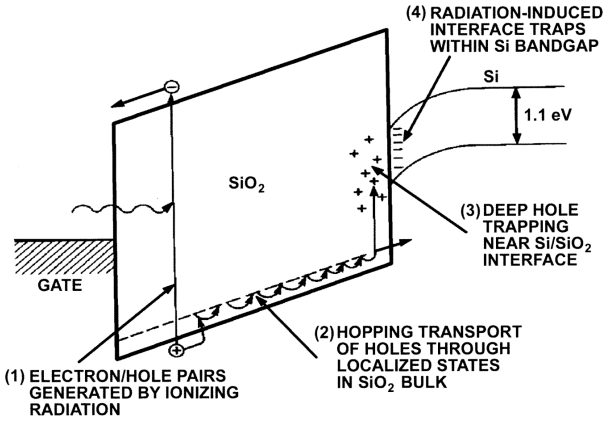

Figure 1.2: Effects of the ionizing radiation in MOS structure: charge production and trapping in the oxide and interface state generation [4].

processes. If these ions reach the interface between oxide and semiconductor they are captured by the passivation (Si-H bond) causing the release of H_2 molecules and the creation of the Pb center. Those traps, that constitute the interface states, are amphoteric defects: the charge polarity depends on the energy of the defect with respect to the Fermi level.

In MOS devices, the trapped positive charges have different effects depending on their position in the device. If the positive charges are accumulated in the gate oxide the result is the negative shift of the threshold voltage. In nMOS devices the positive charges push the substrate into depletion, reducing the threshold voltage of the transistor. In pMOS devices the positive charges push the substrate in accumulation, increasing the threshold voltage in absolute value. As a consequence, nMOSFETs exposed to ionizing radiations could remain permanently in conductive state ($V_{TH} < 0\ V$), while pMOSFETs could remain permanently in non-conductive state ($|V_{TH}| > |V_{MAX}|$).
The positive charges trapped in the oxide can recombine with electrons coming from the channel in the process called annealing. There are two mechanisms leading to the recombination: electron tunneling and electron excitation. The first involves charges trapped near the oxide/semiconductor interface. The second happens typically at high temperature, electrons gain enough energy to overcome the barrier and recombine with charges inside the oxide. Electron tunneling makes charge accumulation more difficult in very thin gate oxides, making highly scaled CMOS devices more robust to the effects of TID on threshold voltage shift.
The interface states, on the contrary, have the same effect in nMOSFETs and pMOSFETs: the threshold voltage increase in absolute value. It because the amphoteric traps are charged according to the Fermi level leading to positive charge trapping in pMOS and negative charge trapping in nMOS. The Equation 1.5 describes the threshold voltage degradation due to positive charges trapped in the oxide and interface states.

$$\Delta V_{TH} = -\frac{1}{C_{OX}} \int_{t_{OX}} \rho(x) x \, dx + \frac{Q_{it}}{C_{OX}} \, [V] \tag{1.5}$$

with C_{OX} capacitance of the oxide capacitor, ρ positive charge density inside the oxide and Q_{it} charge associated with the interface states.
Furthermore, since the Fermi level moves during the turning on of the MOS transistor, the

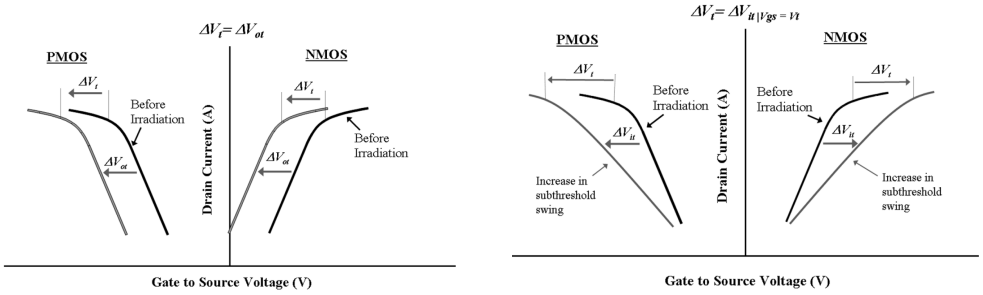

Figure 1.3: MOSFET threshold voltage shift caused by ionizing radiation: (a) trapped charges in the oxide, (b) interface states [5].

amount of charged interface defects increases with the increase of the applied voltage. The combination of this effect and the reduction of the carrier drift velocity due to interface traps leads to the reduction of the slope of $V_G - I_D$ characteristic and, thus, to the reduction of the transconductance. The overall effects in the threshold voltage of the

trapped charges and interface states are visible in Figure 1.3.
The opposing effects of oxide trapped charges and interface states in the nMOSFETs can cause the rebound effect depicted in Figure 1.4. The trapped charges in the oxides that caused the negative shift of the threshold voltage can recombine with the electrons from the channel, while the interface states continue to be created due to hydrogen drift resulting in a final positive shift of the threshold voltage.

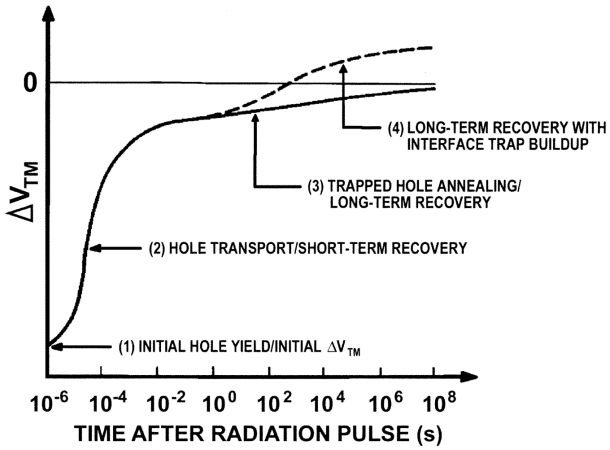

Figure 1.4: Rebound of the threshold voltage in nMOSFETs after irradiation [4].

If the positive charges are accumulated in the isolation oxides as shown in Figure 1.5(a) and (b) or in the buried oxide in the SOI technology, reported in Figure 1.5(c), the result is the reduction of the threshold voltage of the parasitic transistors composed by substrate, drain, source and isolation oxide. This effect leads to parasitic currents in a n-substrate, while in a p-substrate it causes the shrinking of the transistor channel.

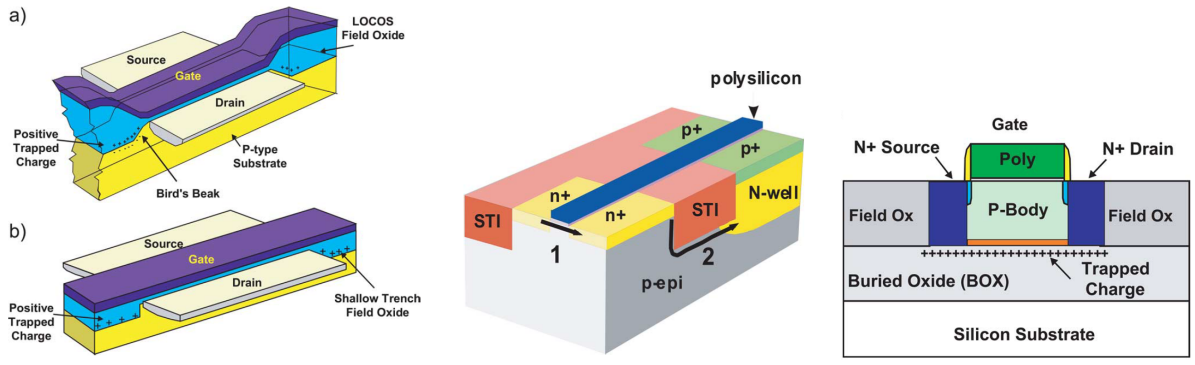

(a) (b) (c)

Figure 1.5: Leakage currents in CMOS technology caused by the trapped positive charge in the isolation oxides (a) within the same device, (b) between different devices and (c) in SOI technology [6].

The effects of the total ionizing dose in bipolar devices are depicted in Figure 1.6(a). The positive charge trapping and the interface states in the isolation oxide between base and emitter cause the increase of the surface recombination velocity and the variation of the surface potential that lead to increased carriers recombination in the base and in the base-emitter depletion region. Consequently, an increasing part of the base current recombines leading to the reduction of the collector current that is driven by the base current that survives the recombination, the result is the reduction of the current gain (Equation 1.6). An example of the relation between TID and gain degradation is visible

in Figure 1.6(b).

$$\frac{1}{h_{FE}} = \frac{1}{h_{FE0}} + \frac{\Delta I_B(TID)}{I_C} \tag{1.6}$$

with h_{FE} final current gain, h_{FE0} initial current gain, I_C collector current and ΔI_B excess base current.
In addition, the charge accumulation in the isolation oxide between base and collector causes the increase of the collector-base leakage current.
The magnitude of the degradation of the BJT parameters depends also on the geometry, lateral and vertical BJTs have different degradation profiles because of the different carriers paths from emitter to collector. In lateral BJTs carriers flow closer to the oxide/semiconductor interface and are more likely subjected to surface recombination [7].

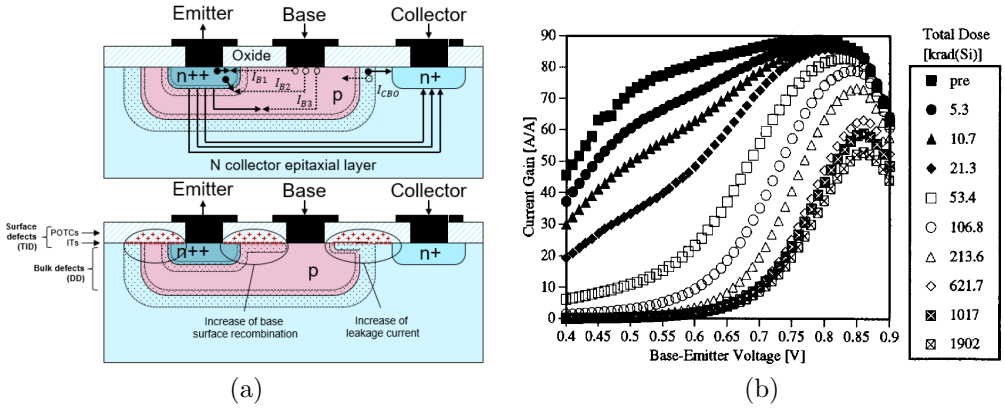

(a) (b)

Figure 1.6: Effects of the ionizing radiations in bipolar transistors. (a) Charge accumulation and interface states in the isolation oxides [3]. (b) Current gain degradation as a function of total dose [8].

Another important issue is the dependency of the base current degradation profile on the BJT type: in NPN transistors the base current increase is superlinear, while in PNP transistors the increase is sublinear. This difference is due to the influence of the oxide trapped charges on the effects of the interface states. In NPN devices, the oxide charges depletes the base leading to the increase of the surface recombination enhancing the effects of interface states. On the contrary, the oxide charges trapped in PNP devices accumulate the base reducing the surface recombination mitigating the effects of the interface states [9]. In both NPN and PNP transistors, the base current increases up to a saturation value, this saturation phenomenon is due to the decrease of the influence of the interface states in the current recombination at high doses. From the Shockley-Read-Hall model for carrier generation and recombination, the recombination peak corresponds to the point at which carrier concentrations are most similar. The accumulation of positive charges in the oxide causes the recombination peak to shift towards the substrate, leading to a decreasing influence of the interface states on the current recombination at high doses [10].

Enhanced Low Dose Rate Effects (ELDRS)

The response of the bipolar devices to ionizing radiation depends also on the rate at which the energy is accumulated in the device, they may exhibit higher degradation when exposed to low dose rate irradiation. ELDRS is an issue for both space and high energy physics applications: the dose rate in operation can be very low, while the qualification process has to be done at higher dose rates due time constraints, resulting in the possible

underestimation of the damage. The Enhancement Factor (EF) is used to quantify the low dose rate sensitivity of a certain parameter of the device, it is the ratio between the low dose rate damage and the high dose rate damage at a fixed accumulated dose.
The typical degradation dependency on the dose rate is visible in Figure 1.7(a), the considered parameter is the excess base current of the bipolar transistor. In these profiles three regions can be identified: low dose rate response (LDR), high dose rate response (HDR) and transition region. The low dose rate response is the flat response on the left of the profile, while the high dose rate one is the flat response on the right with lower magnitude. The transition region is characterized by the reduction of the parameter degradation as the dose rate increases. The difference in magnitude between HDR and LDR and also the transition dose rate is strongly related to the hydrogen concentration inside the oxide [11], as visible in Figure 1.7(b). The high concentration of free holes and trapped holes during the high dose rate irradiation tends to confine the electrons in the oxide, this causes an higher recombination and a consequent reduction of the net positive charge and of hydrogen ions release. It is more accurately described as a Reduced High Dose Rade Sensitivity (RHDRS) [12].

It is interesting to mention that the saturation phenomenon explained previously does

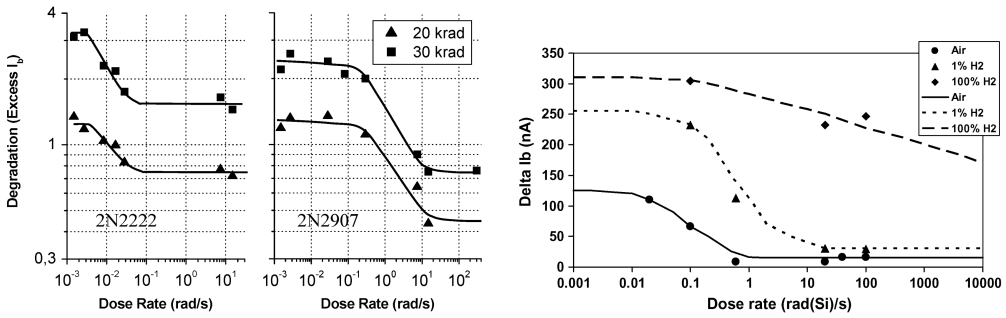

(a) (b)

Figure 1.7: Base current degradation of bipolar transistors as a function of the dose rate evaluated (a) at two values of accumulated dose [13] and (b) at different hydrogen concentrations [11].

not depend on the dose rate, the saturation value of the base current is the same at high and low dose rates [10].

1.2.2 Displacement Damage

The Displacement Damage (DD) is a cumulative effects caused by the non-ionizing energy transfer (NIEL). When an energetic particle penetrates Silicon, the coulombic or nuclear scattering can induce the displacement of Silicon atoms from the crystalline lattice and the creation of the vacancy-interstitial pairs, also called Frenkel defects. The nature of the defects depends on the energy of the atoms displaced directly by the particle that strikes the material (Primary Knock-on Atoms) [14] as schematized in Figure 1.8: for PKAs energies below $1-2\ keV$ only point defects are generated, for energies between $1-2\ keV$ and $12-20\ keV$ PKAs can induce displacement and one cascade (a cluster) of defects is generated, for energies higher than $12-20\ keV$ multiple clusters of defects are generated.

The presence of defects in the Silicon lattice leads to the creation of new energy levels inside the bandgap of the semiconductor [15], the consequences are illustrated in Figure 1.9.

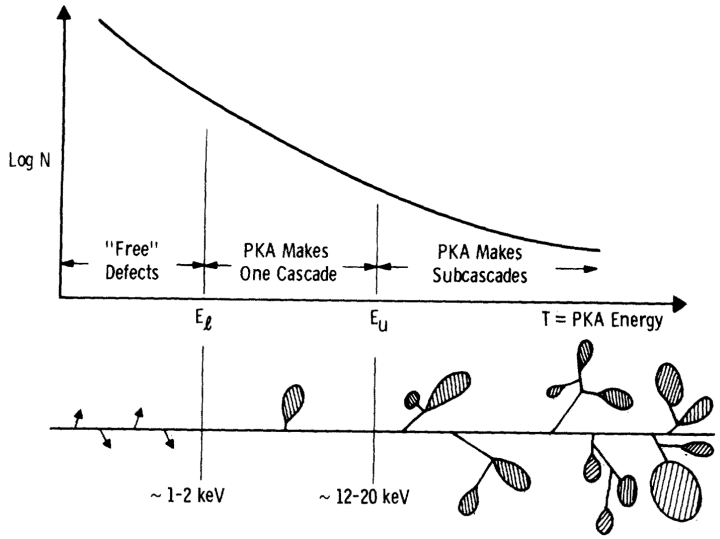

Figure 1.8: Defects creation dependency on the energy of the Primary Knock-on Atoms [14].

- **Carrier generation**: if the energy level is close to midgap, the number of electron-hole pairs generated by thermal excitation increases. It causes the increase of the leakage currents in reverse-biased PN junctions.
- **Carrier recombination**: the traps assist the recombination of carriers (electrons in conduction band and holes in valence band) leading to the reduction of the carrier lifetime. It causes the reduction of the current in the PN junction in forward-biased condition.
- **Carrier trapping**: if the energy level is close to the valence band or the conduction band, the defect can trap temporarily the flowing carriers reducing the Carrier Transfer Efficiency (CTE) in Charge-Coupled Devices (CCD) .
- **Doping compensation**: the defects can introduce acceptor levels that can affect the carriers concentration. At high fluences it can result in the inversion of the semiconductor that changes from n-type to p-type.
- **Carrier tunneling**: under strong electric field, the traps can assist the carriers tunneling leading to leakage current increase.

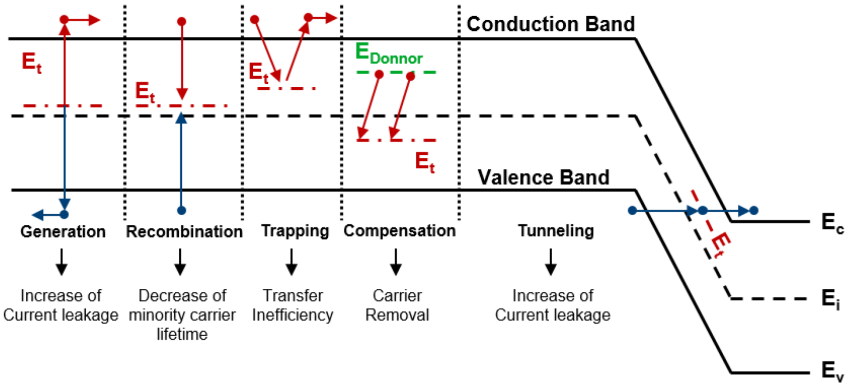

Figure 1.9: Microscopic effects of the defects induced by displacement damage in a semiconductor [3].

The effect of displacement damage in MOS devices is negligible, while it is important in bipolar devices since those devices relies in minority carrier conduction.
The main consequence of displacement damage in bipolar transistor is the reduction of the

current gain [16]: the recombination centers generated by the displacement of the semiconductor atoms lead to the reduction of the minority carrier lifetime and consequently to the increase of the base current. The excess base current is linear with the fluence, as reported in Equation 1.7 [17] and does not saturate.

$$\frac{1}{h_{FE}} = \frac{1}{h_{FE0}} + K \cdot \Phi \tag{1.7}$$

with h_{FE} final current gain of the BJT, h_{FE0} initial current gain, Φ fluence of the particles and K degradation parameter.

NIEL Scaling Hypothesis

The NIEL scaling hypothesis is a powerful theory that rely on the assumption that the displacement damage depends only on the particle Non-Ionizing Energy Loss, it means that two different particles with different energies but with equal NIELs will cause the same amount of defects inside the semiconductor. This assumption has been demonstrate for a large variety of electrical parameters, particles and semiconductors. Figure 1.10 shows the displacement damage cross section $D(E)$, that is proportional to the NIEL, for different particles and energies.

It follows that the comparison between the displacement damage caused by the same

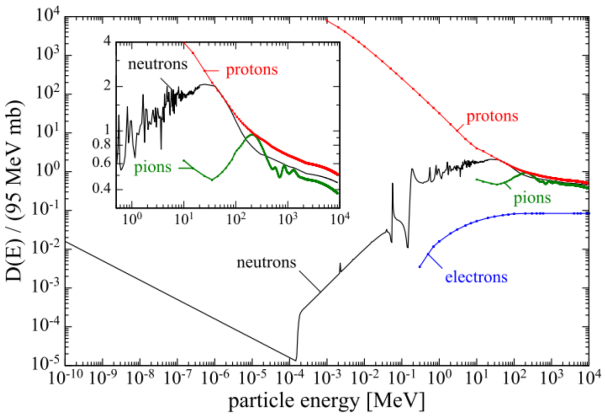

Figure 1.10: Displacement damage cross section as a function of the particle energy for different types of particles.

particle at different energies and also between different particles can be made by comparing only the NIELs. Consequently, it is possible to fold the energy spectrum of a mixed radiation field into one monochromatic radiation fluence [16], the typical reference is the 1 MeV neutron fluence, also called Displacement Damage Equivalent Fluence (DDEF). DDEF is calculated as reported in Equation 1.8: let's consider a radiation field composed by different particle species p, each particle is associated with a spectrum of energies (E) and related fluences $(\Phi(E))$, the damage of each particle is scaled with the damage caused by a 1 MeV-neutron through the NIELs ratio in order to get, for each particle at each energy, the 1 MeV-neutron equivalent damage. The sum of the contributions of all the particles, calculated by integrating in the entire energy spectrum, results in the equivalent fluence.

$$DDEF = \Phi_{n,1MeV} = \sum_p \int \frac{NIEL(p,E)}{NIEL(n,1\ MeV)} \cdot \frac{d\Phi(p,E)}{dE} dE \left[\frac{neutrons}{cm^2}\right] \tag{1.8}$$

1.2.3 Single Event Effects

Single Event Effects (SEEs) are stochastic effects that occurs when energetic particles strike sensible areas of semiconductor devices. Those effects are a consequence of the collection of the charges generated in the path of the particle inside the semiconductor through the ionizing energy transfer (LET).
When a charged particle hits the drain region of a MOSFET in non-conductive state, the large quantity of electron-hole pair generated perturbs the electric potential in the phenomenon called Funneling, also illustrated in Figure 1.11(a). As a consequence, the potential barrier that maintains the MOSFET in non-conductive state can be temporarily removed leading to the the creation of a conductive channel between drain and source as depicted in Figure 1.11(b). This condition in which the MOSFET is temporarily turned on is called Ion Triggered Channeling (ITC) [18].

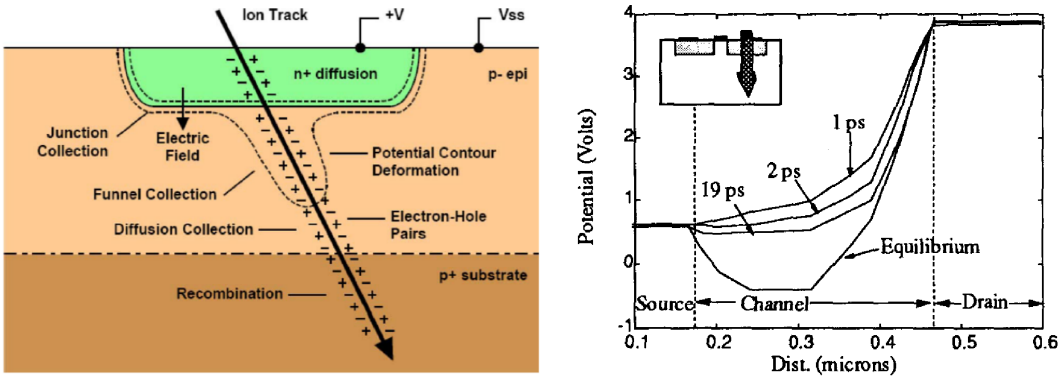

(a) (b)

Figure 1.11: (a) Charge funneling. (b) MOSFET channel potential after the ion impinging in the drain [18]. The time references refer to the passed time after the collision of the ion.

Another potential issue for MOSFETs subjected to ions striking is the triggering of the parasitic BJT structure inside the MOSFET device. In fact, MOSFETs contain an intrinsic bipolar transistor in which the drain and the source are the collector and emitter, while the substrate constitute the base. The type of parasitic transistor depends on the type of MOSFET: NPN in nMOSFETs and PNP in pMOSFETs. When the electron-hole pairs generated by the striking particle are separated, part of the charges flow into the substrate. The resistivity of the semiconductor causes the arise of a voltage drop inside the substrate that can be high enough to activate the parasitic BJT causing the increase of the current and in some cases the permanent damage of the device [19, 20].

Single Event Effects in electronic devices can be divided in the following categories:

- **Single Event Upset** (SEU): it occurs when an ion strikes one of the sensitive parts of a memory cell, for example the drain of one off state MOSFET, the ion can cause the temporary turn on of the MOSFET leading to the state change of the entire memory cell.
- **Single Event Transient** (SET): it is a temporary potential change caused ion striking that propagates in a circuit.
- **Single Event Latchup** (SEL): it is a potentially destructive event, it arises when the parasitic SCR structure (PNPN) in CMOS technology is activated. The PNPN structure has a positive feedback that results in the short-circuit if the device: when

the bottom NPN bipolar transistor is turned ON, current in the top PN junction starts to flow. That current causes the top PNP BJT to go in conduction.

- **Single Event Burnout** (SEB): it occurs in power MOSFETs when the charges generated by the ion turns on the parasitic BJT causing a short-circuit between drain and source.
- **Single Event Gate Rupture** (SEGR): if the charges generated by the passage of the ion accumulate under the gate oxide before being collected by the substrate contact, the electric field inside the oxide can be higher than the critical field, causing the dielectric rapture.

The quantification of the probability of encountering a single event effect is given by the cross-section. Since the SEEs are due to single particles strike, the cross-section is calculated by dividing the number of events by the fluence of the particles at which the device is exposed.

$$\sigma = \frac{N_{SEE}}{\Phi} \; [cm^2] \tag{1.9}$$

with N_{SEE} is the number of single event effects encountered during irradiation and Φ is the fluence of the particles.
As mentioned before, single event effects are strongly related to the number of electron-hole pairs generated by the impinging particles and, thus, to their LET. For this reason, the çross-section is a function of the LET and it can usually be fitted with a Weibull curve.The Weibull curve is depicted in Figure 1.12 and reported in Equation 1.10.

$$\sigma = \sigma_{sat} \left[1 - e^{\left(\frac{LET - LET_{TH}}{w} \right)^s} \right] \tag{1.10}$$

with σ_{sat} saturation cross-section, LET_{TH} threshold LET, w and s fitting parameters.
Only σ_{sat} and LET_{TH} have a physical interpretation: LET_{TH} is the minimum LET that a particles must have to generate enough charges to induce a single event effect. σ_{sat} is the maximum probability to have single event effects and it is correlated with the sensible area of the device.

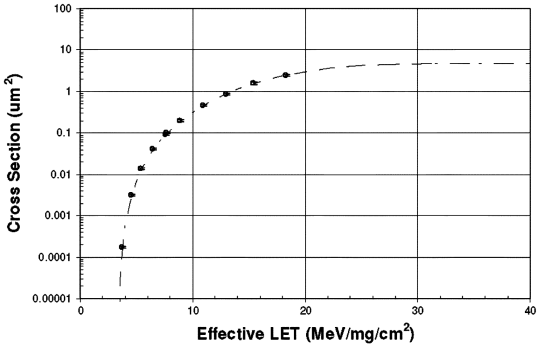

Figure 1.12: Weibull fit of the cross-section as a function of the LET of the impinging particles [21].

1.2.4 Synergistic TID-DD effects

In mixed field environments, where the radiation is a mix of charged particles and neutrons, the devices are subjected to both total ionizing dose and displacement damage. Since bipolar devices are affected by both ionizing and non-ionizing radiation, the degradation of their performances is due to the combination of TID and DD. There are evidences

that in general the overall degradation cannot be assessed by summing the degradation due to TID and the degradation due to DD. The presence of synergistic TID-DD effects can appear both as enhancement or decrease of the device overall degradation.
There are two ways to face this problem: single-transistor (or physical) perspective and circuit-level perspective.
In [22] and [23] the synergy between TID and DD in the single transistor degradation is explored. The proposed explanation to the inequality between the sum of the responses to X-rays irradiation (pure TID) and neutron irradiation (pure DD) is explained with the impact of the oxide and interface traps induced by TID on the recombination rate increase due to bulk defects. The result of this interaction is the reduced degradation of the input bias current of the LM124 depicted in Figure 1.13(a).

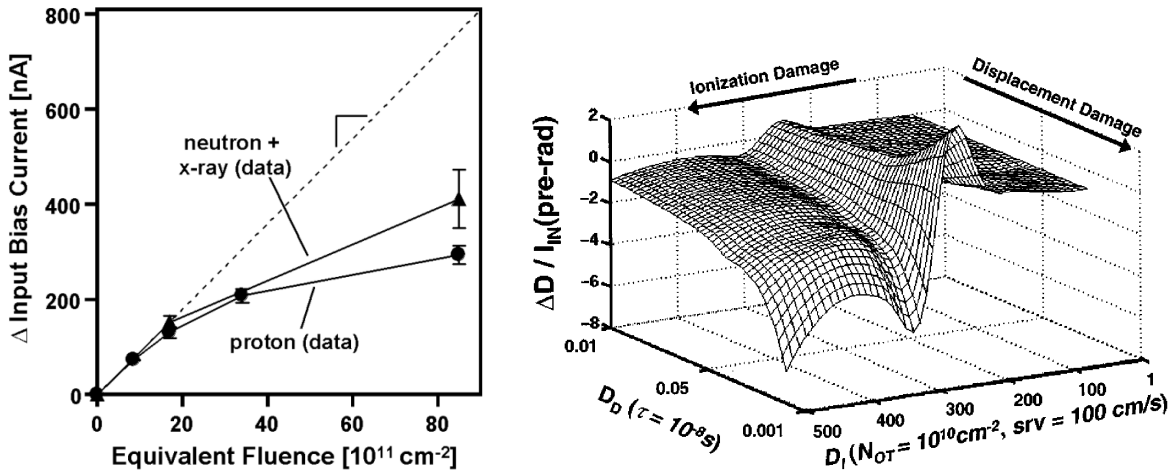

(a) (b)

Figure 1.13: (a) Evidence of synergistic TID-DD effects in the input bias current of the LM124 irradiated with protons [23]. (b) Simulation of the response to combined TID-DD, it exhibits a strongly non-linear behaviour [22].

This model is supported by the simulations of the bias current increase in different TID-DD scenarios. The ionizing radiation effects is modeled as increase surface recombination velocity for the interface states and interface sheet charge for the oxide traps, while bulk damage is modeled as carrier lifetime reduction. The result is the strongly non-linear response to combined TID-DD visible in Figure 1.13(b). As proposed by the authors, the base current recombination due to the reduction of the carrier lifetime due to bulk defects depends also on the carriers concentrations through the Shockley-Read-Hall formula. The impact of the charges trapped in the oxide on the carriers concentrations leads to the non-linear behaviour of the combined TID-DD response.

$$I_{B,bulk} \simeq \frac{q}{\tau} \int_{V_B} \frac{n_b(N_{OX}) \cdot p_b(N_{OX})}{n_b(N_{OX}) + p_b(N_{OX})} dV \tag{1.11}$$

Equation 1.11 describes the bulk recombination current of a BJT derived by the Shockley-Read-Hall model, the displacement damage affects the carrier lifetime τ, while the oxide trapped charges N_{OX} have an impact on the carriers concentrations n_b and p_b [23].

The response is even more complex in a circuit-level perspective. In fact, the relations between components inside an integrated circuit can be non-trivial and non-linear and the different sensitivities to TID and DD of the internal components make the response to mixed radiations very complex. In this case, even if all the internal components have additive TID and DD contributions to the damage, the response is made unpredictable

by the circuit as a whole.
Figures 1.14 shows the response to mixed field of an operational amplifier. The overall degradation of the three parameters open loop gain, input offset voltage and input bias current (in black) cannot be predicted by summing the responses to gamma irradiation (in red) and neutron irradiation (in blue). In this particular case the degradation in the mixed-field environment is higher than the sum of the two contributions.

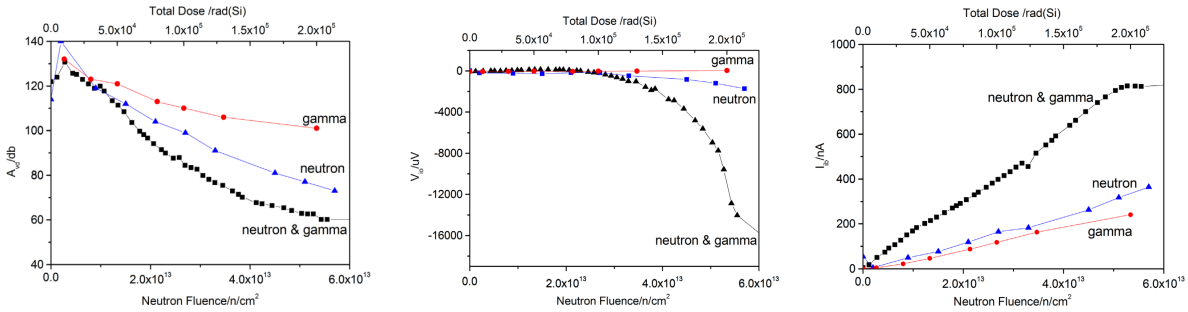

Figure 1.14: Evidence of synergistic TID-DD effects in the (a) Open Loop Gain, (b) input offset voltage and (c) input bias current degradation of the operational amplifier OP07 [24]. The overall degradation in mixed-field environment (black) is higher than the sum of gamma degradation (red) and neutron degradation (blue).

In the particular case of the input bias current, the linearity of the response allows the extraction of an enhancement factor calculated in Equation 1.12.

$$\eta = \frac{K(\Phi, D)}{K(\Phi) + K(D)} \simeq 1.5 \tag{1.12}$$

with Φ neutron fluence, D total ionizing dose and K slope of the degradation profile. The result highlights the fact that the degradation of the input bias current caused by the combination of TID and DD is 50% higher than the sum of the two separate contributions [24].

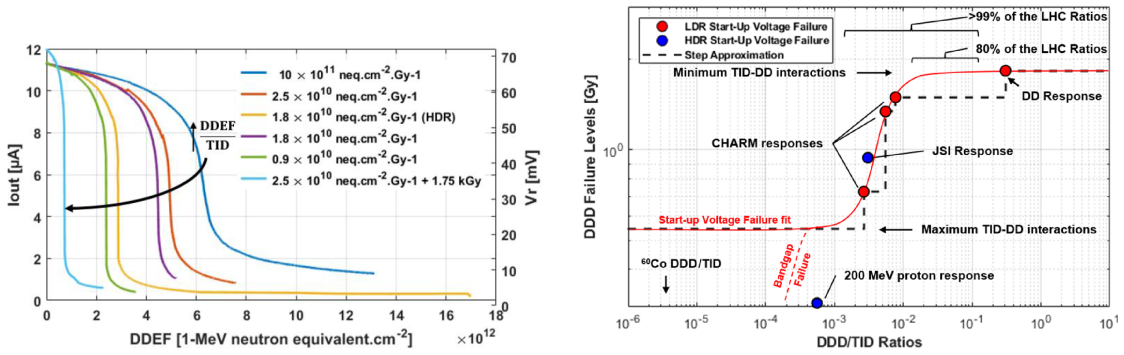

Figure 1.15: Synergistic TID-DD effects in the current reference LM334 degradation profiles [25]. In this case it is possible to extract a relation between degradation and DDEF/TID ratio.

In [26] and [25] the impact of the combined TID-DD effects on the electrical characteristics of the current reference LM334 are studied. Since the response of the device to irradiation is strongly dependent on the ratio DDEF/TID (as visible in Figure 1.15), the first paper proposes an alternative qualification methodology to assess the response of that particular device to the LHC environment, taking into account the DDEF/TID ratios the devices

are subjected to.
In [25] the simulation of the internal components degradation leaded to a deeper comprehension of how TID and DD interact in the overall response. In particular, both TID and DD cause gain degradation of the transistor, resulting in the reduction of the voltage reference. In this, the saturation of the degradation due to TID plays a crucial role in determining the difference between the response due to the TID alone and that in the mixed field. Furthermore, displacement damage causes the onset of collector-emitter leakage currents which lead to the start-up voltage increase. And finally, it was shown that the effect of the DD is enhanced by the gain degradation due to the TID.
The result is a complex behaviour of the current reference that depends on TID, DD and also on the ratio DDEF/TID.

The literature in the field of synergistic effects is still limited, more studies are needed to deeply understand the mechanisms and the impact on the qualification in mixed radiation environments.

Chapter 2

Qualification of Analog Electronic Devices and Systems at CERN

As already mentioned in the introduction, the functionality of the CERN accelerators complex strongly rely on the tolerance of electronic components to radiations. The unexpected degradation of one or more components due to cumulative effects or single event effects induced in sensitive areas can lead to beam dumps, condition in which the particle beam is stopped in a fixed target whose purpose is to absorb all the beam energy. But in the worst case these effects caused by radiations can damage the accelerator. An example of potentially destructive event is the failure of the quench protection system, this system is aimed at detecting whether superconductive magnets start to become conductive and, in that occasion, it releases all the energy of the magnets on power resistances and turns off the power to the magnets. If this system fails, the transition from superconductive to conductive state become fatal for the magnet, all the energy stored in the magnetic field is dissipated by the resistance of the magnet itself leading to the heating of the magnet and to its permanent damage.
These are only two examples of the importance of the reliability at CERN, for this reason, a lot of effort has been put to develop a radiation hardness qualification procedure.
In this chapter the LHC radiation environment is introduced, highlighting the challenges of this particular environment, a brief explanation of the CERN qualification procedure is provided and finally the selection of the components for the research study is discussed.

2.1 LHC Radiation Environment

Among all the CERN accelerators, the Large Hadron Collider is the bigger and powerful one, the vast majority of the electronic systems designed at CERN are ultimately installed in the LHC. For this reason, characterizing the LHC radiation environment through simulations and on-site measurements is of fundamental importance to understand the radiation levels to which electronic systems are subjected.
LHC is divided in eight octant as depicted in Figure 2.1, four of those regions host the main CERN experiments: ATLAS, CMS, LHCb and ALICE. In correspondence of the experiments the two proton beams traveling inside the vacuum pipes in opposite directions collide and generate the elementary particles that are detected by the huge system detectors.

The large amount of secondary particles generated in the beams collision makes the so called Interaction Points (IP) the most radioactive locations of the entire LHC.

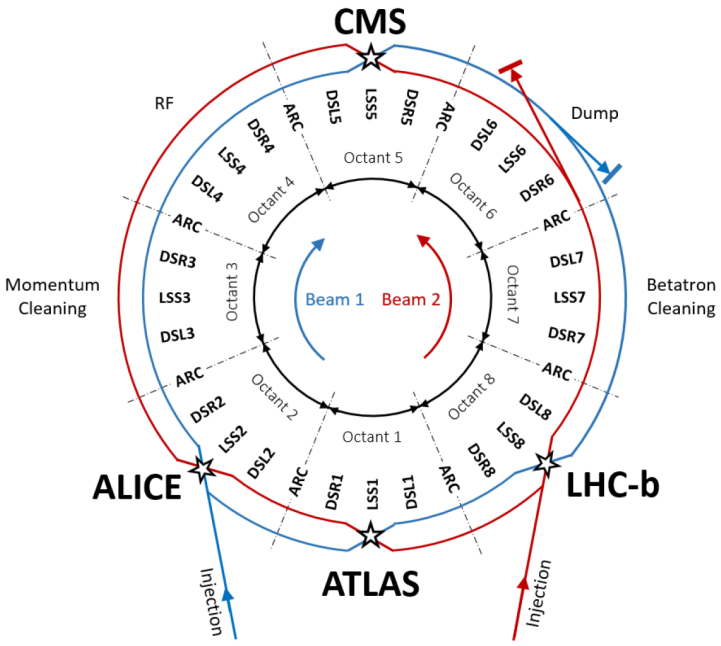

Figure 2.1: LHC structure [26].

To better understand the distribution of the radiation levels in the LHC let's consider the structure of and octant hosting an Interaction Point represented in Figure 2.2(a) and the corresponding radiation levels in Figure 2.2(b). The octant can be divided in two sections: the arc region, and the Long Straight Section (LSS). In the arcs the beams travel inside the vacuum tubes kept at $-271.3\ ^oC$ to guarantee the superconductivity of the magnets, while in the LSS the beams collide. The junction between arc and LSS is the dispersion suppressor used for reducing the dispersion of the beam. As can be noted in Figure 2.2(b), the radiation levels become lower and lower as we move from the Interaction Point towards the arcs.

In the Insertion Regions the annual ionizing dose can be as large as 10 kGy, in the

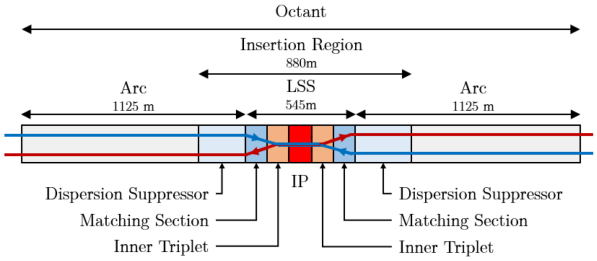

(a)

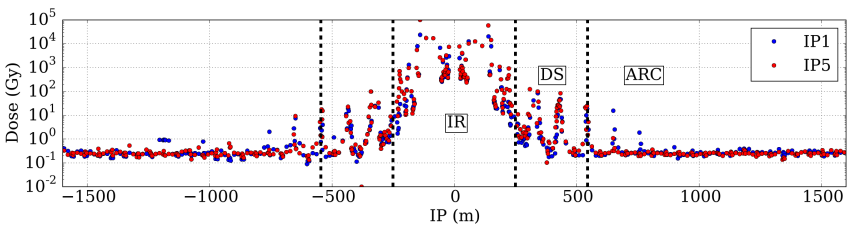

(b)

Figure 2.2: (a) Structure of an octant of the LHC [3]. (b) Radiation level distribution of the octants hosting the interaction points 1 and 5 during the 2016 proton-proton run [1].

DS the peak can reach 100 Gy/yr, while in the arcs, where the main cause of radiation

is the beam-gas interactions due to the residual gas particles inside the vacuum tubes, the radiation levels are usually below 1 Gy/yr. Therefore, in IR and DS the use of Commercial-Off-The-Shelf (COTS) devices is impossible, the doses are too high to be tolerate, only rad-hard devices can be installed. On the contrary, arc regions can host COTS-based systems [1].

Furthermore, the difference in radiation levels between the points of the LHC is not only a difference in magnitude, but also in the composition of the radiation field and in particular in the ionizing and non ionizing dose ratio. Figures 2.3(a) and (b) show the ionizing (TID) and non-ionizing (DDEF) radiation levels as a function of the distance from the interaction point and the corresponding DDEF/TID ratio.

The ratio between DDEF and TID is strongly variable with the distance from the

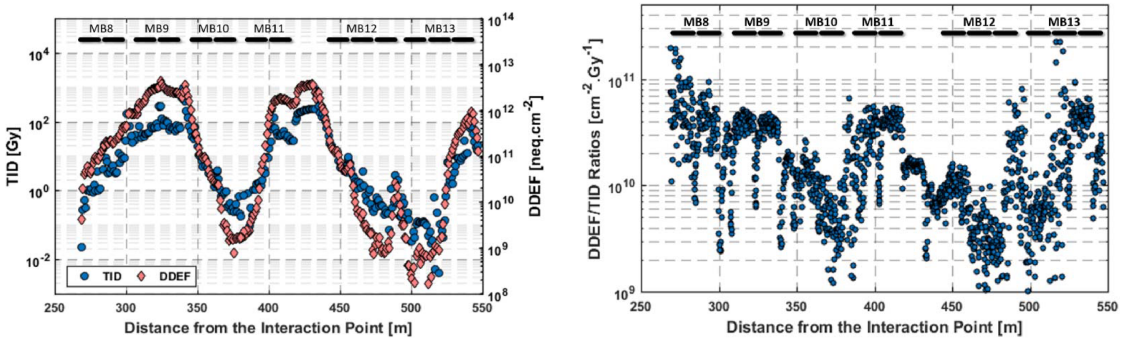

(a) (b)

Figure 2.3: Radiation environment near the interaction points 1 and 5: (a) radiation levels and (b) ratio between displacement damage and total ionizing dose [26].

interaction points between $1 \cdot 10^9$ and $1 \cdot 10^{11}$ and this variability is not restricted to the specific points shown in those figures. As can be seen in Figure 2.4, the DDEF/TID variability can be extended to the entire LHC and it covers a wide range: an electronic system distributed in the LHC can be subjected to a hundreds of times difference in displacement damage while absorbing the same ionizing dose.

This environment poses some challenges in the qualification procedure: since the LHC

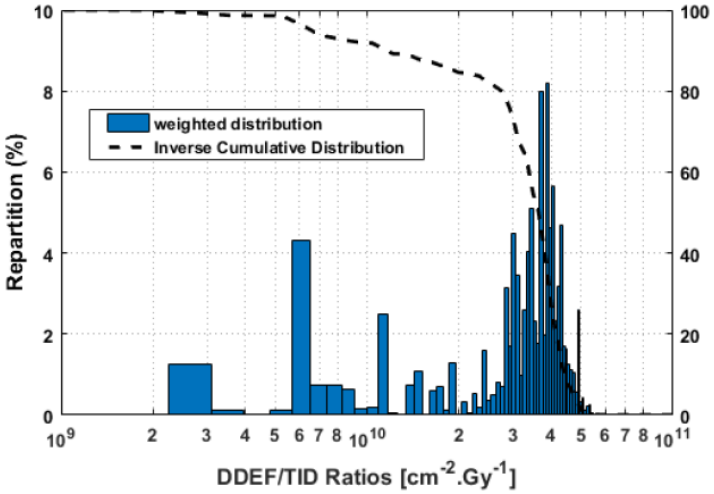

Figure 2.4: Distribution of the DDEF/TID ratio in the LHC [26].

environment is highly variable both in terms of radiation levels and in terms of the ratio between ionizing and non-ionizing dose, the electronic systems installed in the LHC will

be affected by the radiation in very different ways depending on where they are placed. In presence of synergistic TID-DD effects, the response to radiation can be very hard to predict and the result of the qualification procedure may only be applicable to some specific LHC locations.

2.2 CERN Devices Qualification

As explained before, there are some locations of the LHC where it is impossible to place COTS-based systems due to the very high annual dose. In the other locations, where the use of COTS devices is possible, such components must be qualified to ensure their tolerance to the radiation levels to which they are subjected.
For this reason, the electronic systems designed in the CERN AcceleraTor Sector (ATS) follow a specific Radiation Hardness Assurance (RHA) procedure divided in six phases depicted in Figure 2.5.

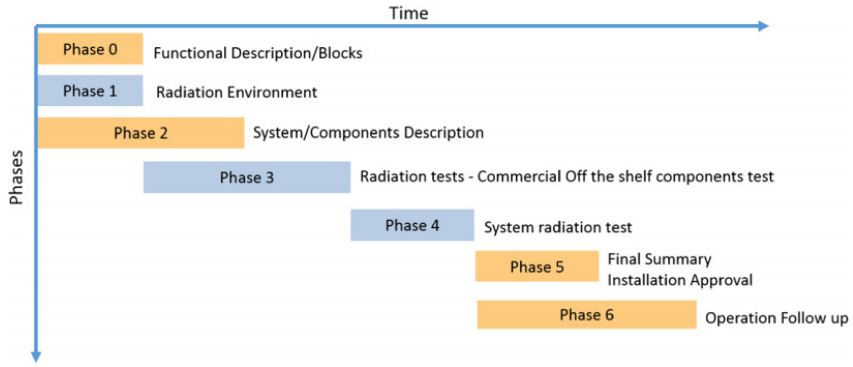

Figure 2.5: Radiation Hardness Assurance (RHA) process diagram of electronic systems designed at CERN [27].

In the phase 0 the functionality of the system in the accelerator is described, at the same time the phase 1 focuses on the identification of the radiation environment in which the system will be installed. The description of the radiation levels is performed using FLUKA simulations [28], Radiation MONitoring (RadMON) [29] and Beam Loss Monitoring (BLM) [30] systems. In this phase the system radiation requirements are established according to the project's target reliability. In the phase 2 the development of the system starts and the radiation requirements are applied trying to prevent the failures with mitigation techniques. Critical components are identified during this phase. In the phase 3 each component of the system is tested to assess its sensitivity to radiation, these results are used to extrapolate the overall sensitivity of the system. The entire system undergoes a radiation test to evaluate its real performances in the phase 4. If the system respects the initial requirements it is approved for the installation during phase 5. Finally, in the phase 6, after the commissioning, the system is monitored during its operations and anomalies or faults are reported.
If the system fails at one of these phases the procedure has to be repeated from phase 2: the system must be designed again or the failed component has to be substituted, then all the tests are repeated.

One of the most important phases of the RHA, and the focus of my thesis, is the component-level qualification included in the phase 3 of the process. In this phase, the radiation tolerance of the components that have been selected for the specific system is evaluated. First, the test radiation field is chosen according to the type of component:

bipolar, CMOS or BiCMOS. As explained in the previous chapter, since bipolar and BiCMOS devices suffer both TID and DD, the test must be performed in a mixed TID-DD field facility, on the contrary, CMOS devices can be tested only for TID with gamma or X-rays due to their insensitivity to DD. Concerning SEE testing, it is not necessary for bipolar or SOI technology, while it is performed for CMOS devices. The test facility is chosen according to the type of test and the radiation field. Figure 2.6 shows a summary of the types of devices, the types of tests to which they can be subjected and the corresponding facilities used by the CERN Radiation Working Group (RadWG) for the qualification of the components.

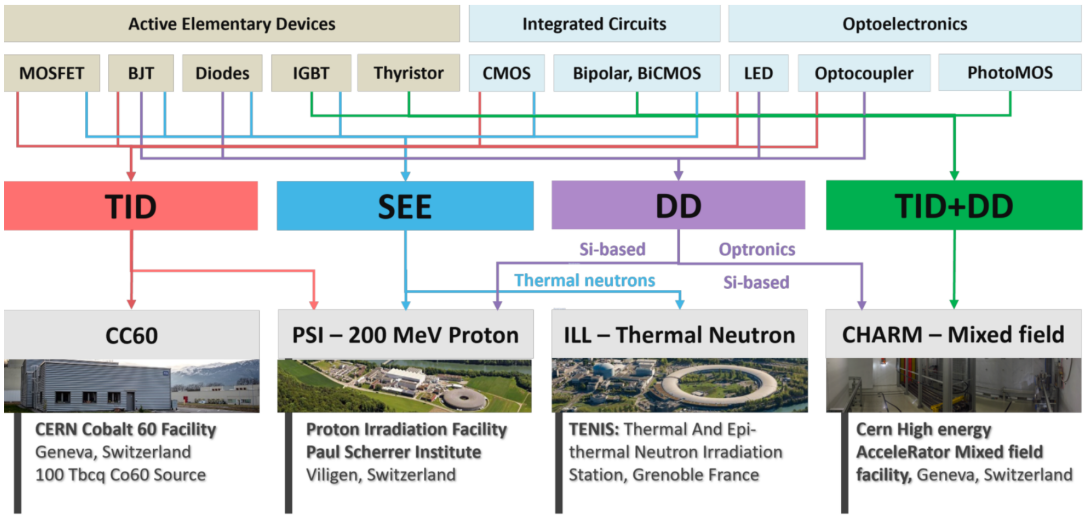

Figure 2.6: Diagram showing the different types of tests that can be performed according to the device type, and corresponding test facility [27].

The test of the components is performed in the worst case bias condition foreseen by the project and measuring the parameters that are known to be sensitive to radiation. Let's consider the MOSFET test as an example: the main parameter affected by radiation is the threshold voltage caused by the separation and trapping of the charges generated by ionization in the gate oxide. Since the charge separation depends positively on the electric field applied to the gate, the worst case scenario, that leads to the maximization of the threshold voltage shift, consists in the application of the maximum gate voltage foreseen by the project specifications. The same considerations are made for all the devices.
Another key factor to take into consideration is the lot-to-lot variability of the responses under irradiation caused by process variation during manufacturing. To avoid unexpected behaviour of the components in operation, two lots are usually tested: a qualification lot to understand if the component is a good candidate for the project, and the production lot to guarantee its radiation tolerance in operation. For highly distributed systems, in which the number of deployed components can be very high, a single production lot can be insufficient. In those cases all the production lots should be qualified.
Highly distributed systems pose another challenge to the radiation qualification: the high variability of the ratio between ionizing and non-ionizing dose around the LHC could make a single radiation test non-exhaustive for the qualification. In fact, if the devices are sensitive to synergistic TID-DD effects, the response will be strongly related to the LHC location and a single test could lead to the underestimation or overestimation of the degradation.
A solution to face this problem was proposed in [26]: the devices should be tested at several DDEF/TID ratios covering the entire LHC spectrum to extract the failure level

according to the radiation requirements. This failure level will depend on the DDEF/TID ratio and will be used to calculate the mean lifetime.

$$\text{Lifetime}(x) = \frac{\lambda(R_{DDEF/TID}(x))}{R_{level}(x)}\ [years] \tag{2.1}$$

with x location in the LHC, $R_{DDEF/TID}(x)$ ratio DDEF/TID, λ failure level according to the ratio DDEF/TID and $R_{level}(x)$ annual radiation levels.
This methodology is effective but not yet implemented due to the high number of tests and resources needed to perform a single qualification.

2.3 Components Selection for the study

As mentioned in the first chapter, devices potentially sensitive to synergistic effects are those made in bipolar or BiCMOS technology due to their sensitivity to ionizing and non-ionizing dose. For this reason, I chose the candidates for the study from the list of bipolar and BiCMOS references already tested from the CERN Radiation Working Group that exhibited evident degradation [31]. There are mainly three facilities where the RadWG tests devices for cumulative effects: CERN Cobalt 60 facility (CC60), CERN High energy AcceleRator Mixed-field facility (CHARM) and Paul Scherrer Institut Proton Irradiation Facility (PSI). In the next chapter the facilities that are used for this study (CC60 and CHARM) will be described, for the moment it is important to underline that CC60 is used to perform pure TID tests, while CHARM and PSI for combined TID-DD tests. In addition, CHARM has an higher ratio DDEF/TID than PSI: for the same amount of total ionizing dose, the components at CHARM are subjected to more than three times more displacement damage than PSI. In order to be sure to select components that exhibit strong degradation at CHARM (the main facility used for this study), I selected only bipolar and BiCMOS devices that degraded at CC60 or PSI. The assumption is that the higher the DDEF value, the greater the total degradation of the component.
For the study six types of components are selected:

- operational amplifiers
- instrumentation amplifiers
- voltage regulators
- voltage references
- insulated gate bipolar transistors (IGBTs)
- photoMOS

In the following paragraphs an explanation of the behaviour under irradiation is provided for all the type of devices and the choice of the references is motivated with the results of previous radiation tests.

2.3.1 Operational Amplifiers

Operational amplifiers are integrated circuits that amplify the voltage difference between their two inputs and they are characterized by high gain, low output resistance and high input resistance. However, they also exhibits some non-idealities, such as input bias current and input offset voltage. The input bias current is the base current required to bias

the transistors in the amplifier's input stage, ensuring they have a non-zero collector current. In BiCMOS amplifiers, which typically feature a CMOS input stage, the input bias current is nearly zero. The input offset voltage arises from process variations, causing slight differences in internal transistors that are supposed to be identical.
The behaviour of the operational amplifiers under radiation has been studied deeply in literature, but only few studies has been carried out to asses the synergistic effects of TID and DD. The parameters affected by ionizing and non-ionizing radiations are the input bias current, the input offset voltage, the supply current and the open loop gain [23,24,32–37]. The four operational amplifiers selected for the study are summarized in Table 2.1. The **AD829** was tested at PSI (200 MeV proton beam) and showed a strong degradation of the input bias current and the supply current. The degradation of the supply current can be a symptom of gain degradation: the current gain degradation of the internal transistors due to radiation leads to the amplifier gain degradation and can also lead to the decrease of the transistors collector current constituting the supply current. The **LM358AD**, similarly to the AD829, was tested at PSI and exhibited a strong degradation of the input bias current, in addition, it showed input offset voltage degradation and also output voltage degradation. The decrease of the output voltage was measured with the amplifier in follower configuration, the result could be due to the decrease of the offset voltage. Figures 2.7(a) and (b) show the typical behaviour of the input bias current and input offset voltage of the operational amplifiers under irradiation.

On the contrary, the BiCMOS amplifier **MAX4238** didn't exhibit bias current degradation or a linear offset voltage degradation when tested at PSI, it showed an abrupt degradation of the input offset voltage as visible in Figure 2.8, which is reflected in the output voltage.

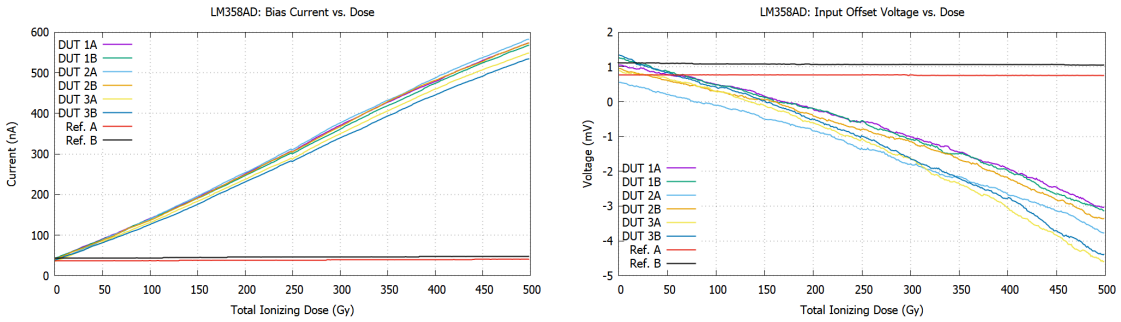

(a) (b)

Figure 2.7: Response of the operational amplifier LM358AD to 200 MeV proton beam: (a) input bias current and (b) input offset voltage.

The last operational amplifier, the **LT1013**, is a bipolar amplifier that was used as auxiliary amplifier in a BJT test board. The response of the board under gamma irradiation at Cobalt 60 was not coherent with the BJTs response. The wrong behaviour was due to the malfunctioning of the amplifiers that at some point stopped working properly giving a fixed output voltage whatever input voltage was applied. A symptom of the malfunctioning and the possible decrease of the open loop gain, as in the case of the AD829, was the decrease of the supply current depicted in Figure 2.9.

2.3.2 Instrumentation Amplifiers

Instrumentation amplifiers are precise closed loop differential amplifiers with adjustable gain. The feedback network that set the gain of the amplifier is usually internal to the IC

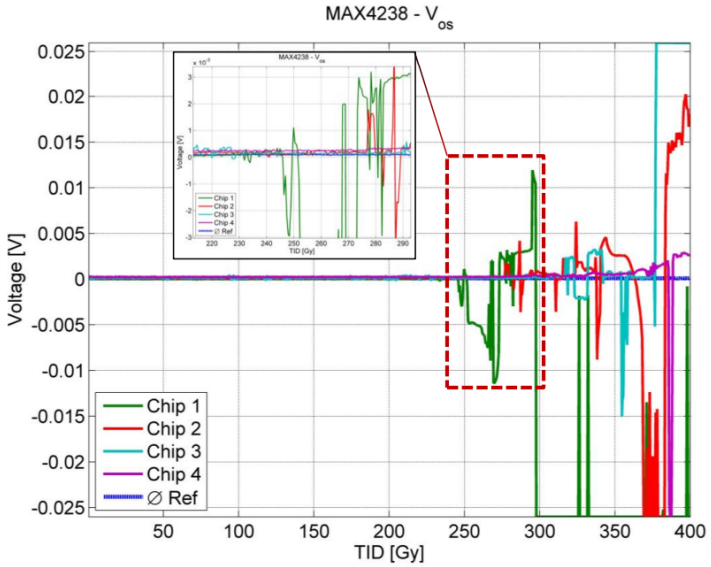

Figure 2.8: Input offset voltage degradation of the operational amplifier MAX4238 exposed to 200 MeV proton beam.

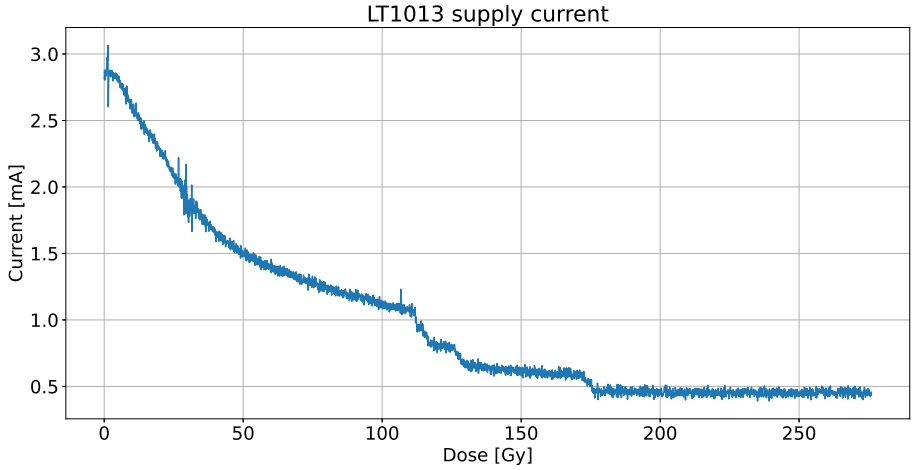

Figure 2.9: Supply current degradation of the operational amplifier LT1013 exposed to gamma irradiation.

allowing a precise gain. In addition, they are characterized by high input resistance, high common mode rejection and low output resistance and, similarly to operational amplifiers, they exhibit input bias current and input offset voltage.
The parameters of the instrumentation amplifiers affected by radiation are the offset voltage and the differential gain [38, 39]. The bias current is likely affected by radiation since the input stage of the instrumentation amplifiers is equivalent to the input stage of the operational amplifiers.
The four instrumentation amplifiers selected for the study are visible in Table 2.1. The **INA326** is a CMOS device that was tested at CHARM and PSI. The selection of this component for the study is driven by the unexpected results obtained in those two tests: while at PSI (Figure 2.10 left) the output voltage degraded after 300Gy, at CHARM it didn't degrade even at 500Gy (Figure 2.10 right). Since the CHARM environment is more rich of neutrons than PSI, it was expected to degrade more at CHARM. This behaviour can be due to synergistic effects of TID-DD, in particular to a moderation of the effects of the displacement damage, but it can also be due to dose rate effects, in fact the dose rate at PSI ($\sim$ 800 Gy/h) is more than two order of magnitude higher than CHARM ($\sim 5\ Gy/h$).

The last three devices, **AD621**, **AD8420** and **MAX4208**, exhibited output voltage

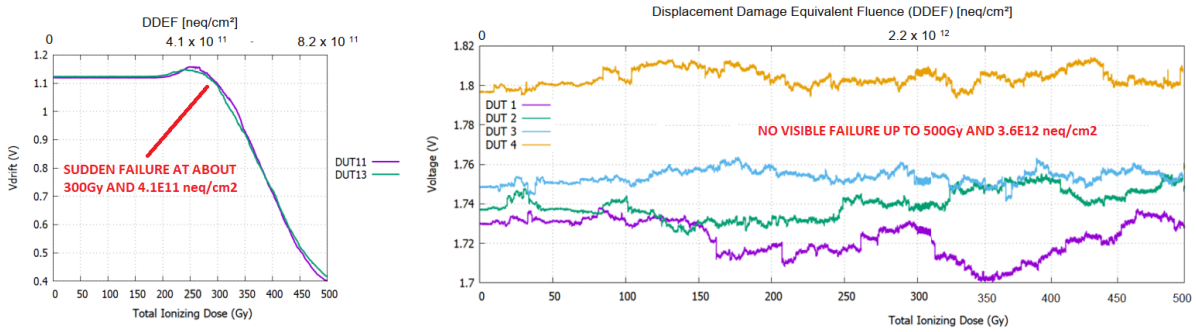

Figure 2.10: Difference in degradation profile of the instrumentation amplifiers INA326 at PSI (left) and CHARM (right).

degradation after 200Gy, 300Gy and 400Gy respectively. The AD621 and MAX4208 were tested at Cobalt 60, while the AD8420 was tested at CHARM.

2.3.3 Voltage Regulators

Voltage regulators are devices designed to maintain a constant output voltage regardless of changes in input voltage or load conditions. However, for linear voltage regulators, the input voltage must be above a threshold for the regulator to work, named start-up voltage. Their operating principle is based on the comparison between an internal voltage reference and the output voltage in a feedback loop which results in the stabilization of the output voltage. The feedback network can be internal or external resulting in fixed or adjustable voltage regulators.
The radiation affects mainly two parameters of the voltage regulators: the output voltage and the start-up voltage [25, 40–42].
All the six selected regulators, reported in Table 2.1, were tested at PSI and exhibited an output voltage degradation. The behaviour of the output voltage can be various, it can decrease as the cumulated ionizing dose increases, but it can also increase with the TID. In Figures 2.11(a) and (b) two opposite types of degradation are shown. Furthermore, the degradation can be gradual or abrupt, an example of abrupt negative degradation is shown in Figure 2.11(a) after 200Gy. This type of degradation can be due to the increase of the start-up voltage: when the start-up voltage overcome the maximum input voltage, the regulator stops working.
In the particular case of the selected components, the **TSP73033**, the **MAX8881** and the **MIC29302** showed a positive degradation, while the **LM2936**, the **LT1085** and the **LT1763** showed a negative degradation.

2.3.4 Voltage References

Voltage references, similarly to the voltage regulators, are devices that provide a fixed output voltage when biased with a sufficiently high input voltage. But unlike regulators, the references are not adjustable, cannot drive high currents, their output voltage is more precise and less noisy.
Although the voltage references are usually more robust to radiation, they may exhibit output voltage degradation [39, 43, 44].
As can be seen in Table 2.1, only two references are selected. The types of degradation are the same described in the previous paragraph. The output voltage degradation of the

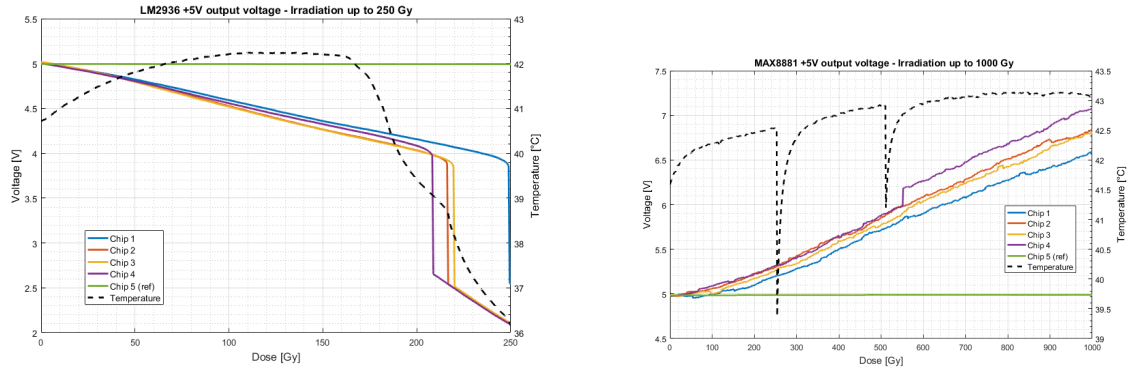

(a) (b)

Figure 2.11: Output voltage degradation of two voltage regulators exposed to 200 MeV proton beam: (a) LM2936 and (b) MAX8881.

MAX6350 was abrupt and negative, while the one of the **ADR435** was gradual and positive.

2.3.5 Insulated Gate Bipolar Transistors (IGBTs)

IGBTs are the simplest devices in BiCMOS technology, as the name suggests, they have the output characteristics of the bipolar transistors while having the input characteristics of the MOSFETs. They can be represented with a MOSFET that drives the base current of a BJT.
The parameters affected by the radiation are the threshold voltage, that involves the input stage of the IGBT, and the current gain [45–47].
The two references selected for the study are summarized in Table 2.1. The old version of the **AUIRG4PH50S** was tested at CNRAD (mixed field radiation) and it exhibited the typical decrease of the threshold voltage depicted in Figure 2.12. As with MOSFETs, the threshold voltage of the IGBTs decreases as the ionizing dose increases, and it is partially restored after some days of annealing. The **IKW15N120BH6** has not yet been tested by RadWG. Its selection is driven by the necessity to qualify it for the CERN project to which it belongs.

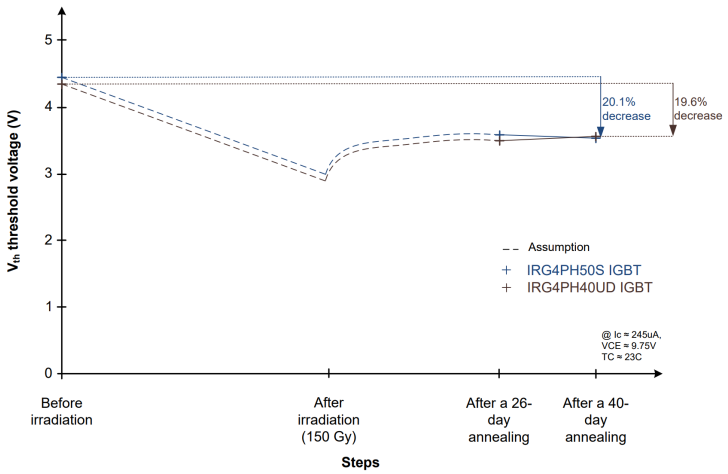

Figure 2.12: Threshold voltage degradation of the IGBT IRG4PH50S exposed to mixed field radiation (CNRAD).

2.3.6 PhotoMOS

PhotoMOS are solid state relays that rely on the same principle of the optocouplers. The input stage is a infrared LED, while the output stage is a MOSFET driven by a photodetector. When sufficient current is supplied to the input LED, the output MOSFET switches to the conductive state acting as a closed switch.
There are no studies that describe the behaviour of the PhotoMOS in radiation environments, only in [48] the increase of the start-up current of the photoMOS is shown as a function of TID and DDEF.
The degradation of the PhotoMOS exposed to radiation is probably due to a combination of the reduction of the emitting efficiency of the LED due to displacement damage and the MOSFET degradation due to ionizing radiation. Figure 2.13 shows the degradation of the input threshold current of the PVS3354 leading to the permanent failure of the device that cannot be turned on anymore.
The four selected references are the reported in Table 2.1. The infrared LED inside three

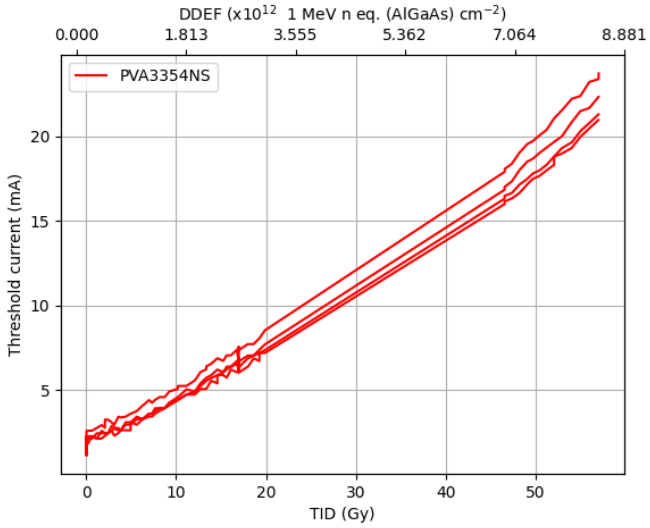

Figure 2.13: Threshold current degradation of the photoMOS PVA3354NS exposed to mixed field radiation (CHARM).

out of four devices (**PVA3354NS**, **VOR1142M4** and **ASSR-1218-003E**) is made of aluminium gallium arsenide (GaAlAs). The material that composes the **AQW210S** LED was not provided by the manufacturer, however, as the case of the IKW15N120BH6, its selection is driven by the necessity to qualify it. The knowledge of the LED material is fundamental to scale the displacement damage equivalent fluence according to that material.

2.3.7 Summary

Table 2.1 summarizes the components chosen for the study, the manufacturer and the technology used to fabricate the ICs. For the PhotoMOS, the "Technology" entry is filled with the LED material, and for the voltage references it is filled with the architecture.
For each device a single lot is procured to reduce the variability in the response.

Type	Reference	Manufacturer	Technology
Operational Amplifier	AD829	Analog Devices	Bipolar
	LM358AD	Texas Instruments	Bipolar
	MAX4238AUT+T	Analog Devices	BiCMOS
	LT1013	Analog Devices	Bipolar
Instrumentation Amplifier	INA326	Texas Instruments	CMOS
	AD621	Analog Devices	Bipolar
	AD8420	Analog Devices	Bipolar
	MAX4208	Analog Devices	BiCMOS
Voltage Reference	MAX6350	Analog Devices	Buried Zener
	ADR435TRZ-EP	Analog Devices	XFET
Voltage Regulator	LM2936MP-5.0	Texas Instruments	Bipolar
	LT1085	Analog Devices	Bipolar
	TPS73033	Texas Instruments	BiCMOS
	MAX8881EUT50	Analog Devices	BiCMOS
	LT1763IS8	Analog Devices	Bipolar
	MIC29302	Microchip	Bipolar
IGBT	AUIRG4PH50S	Infineon	BiCMOS
	IKW15N120BH6	Infineon	BiCMOS
PhotoMOS	PVA3354NS	Infineon	GaAlAs
	AQW210S	Panasonic	—
	VOR1142M4	Vishay Semiconductors	GaAlAs
	ASSR-1218-003E	Broadcom	GaAlAs

Table 2.1: List of the selected components.

Chapter 3

Test Campaigns Organization

3.1 Test Circuits

The first step to evaluate the responses to combined TID-DD effects is the selection of the electrical parameters to be measured and the corresponding test circuits. Table 3.1 summarizes the measured electrical parameters for each type of device.

Component type	**Measured parameter**
Operational Amplifier	Input Bias Current Input Offset Voltage Open Loop Gain
Instrumentation Amplifier	Input Bias Current Input Offset Voltage Output Voltage
Voltage Regulator	Output Voltage Start-up Voltage
Voltage Reference	Output Voltage Start-up Voltage
IGBT	Threshold Voltage Collector and Gate Leakage Currents
PhotoMOS	Threshold Current Drain Leakage Current

Table 3.1: Types of tested components and relative measured parameters.

The following paragraphs will explain the test circuits I designed to measure those devices parameters. The solutions are standard test circuits already used at CERN for the devices qualification, the values of the passive elements are set according to the DUTs specifics.

3.1.1 Input Bias Current

Figure 3.1 shows the test circuit for measurement of the input bias current.
The bias current entering the amplifier's positive input is converted into an input voltage

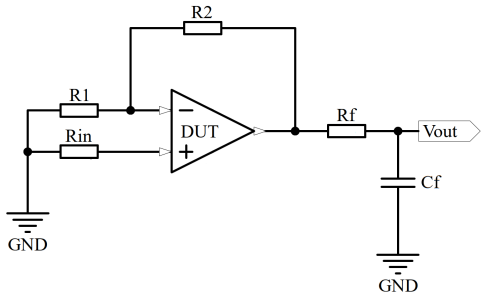

Figure 3.1: Amplifiers input bias current test circuit.

by the resistor R_{in}. This input voltage is then amplified by the DUT, with the amplification factor determined by the resistors R_1 and R_2.

$$\begin{cases} G = 1 + \frac{R_2}{R_1} \\ I_{bias} = \frac{V_{out}}{G \cdot R_{in}} \end{cases} \tag{3.1}$$

The output RC filter is aimed at stabilizing the output voltage reducing the noise.
This test circuit can encounter an issue: if the open loop gain of the amplifier becomes too low, the output voltage decreases and leads to the misinterpretation of the result. In fact, the decrease of the output voltage could be related to the reduction of the input bias current and to an improvement of the performances. To avoid this problem, the open loop gain measurements can be used to correlate the results.
In the case of instrumentation amplifiers the problem is faced by imposing the same gain to the output voltage drift test circuit. In this way it is possible to understand if the behaviour of the bias current test circuit is due to the bias current or to the amplifier gain.

3.1.2 Input Offset Voltage

The test circuit for the input offset voltage measurement is shown in Figure 3.2. The

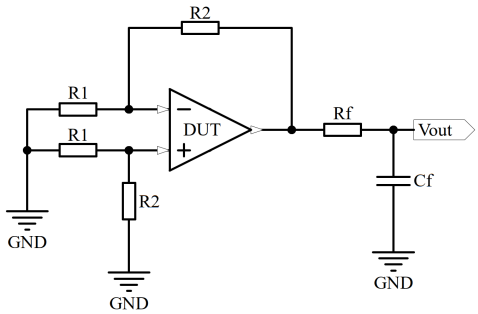

Figure 3.2: Amplifiers input offset voltage test circuit.

offset voltage is amplified by the gain of the amplifier, filtered by the RC circuit and measured at the output. It is very similar to the input bias current test circuit, but in this case the value of the input resistors named R_1 is lower with respect to the R_{in} of the bias current measurement. This is fundamental to have a negligible bias current effect on the measurement of the offset voltage.

$$\begin{cases} G = \frac{R_2}{R_1} \\ V_{offset} = \frac{V_{out}}{G} \end{cases} \tag{3.2}$$

As in the previous case, the behaviour of this test circuit relies on the gain of the device under test. But also in this case, the results can be compared with the open loop gain measurement of the operational amplifiers and with the output voltage drift of the instrumentation amplifiers.

3.1.3 Open Loop Gain

The open loop gain measurement is performed with the test circuit depicted in Figure 3.3. The feedback loop with the auxiliary amplifier (AUX) in integrator configuration forces the output voltage of the DUT to be equal to the input voltage V_{in}. The output voltage of the auxiliary amplifier, that is measured by the acquisition system, must be equal to the voltage at the input of the DUT scaled by a factor set by the resistive feedback network. The open loop gain is calculated from the output voltage of the auxiliary amplifier as follows:

$$A_v^{OL} = \frac{V_{in}}{V_{out} \cdot \frac{R_2}{R_2+R_3}} \tag{3.3}$$

Since the focus of the measurement is the static differential gain, the addition of the output low pass filter does not affect the measurement and stabilizes the voltage reducing the noise.
This circuit is sensitive to the offset voltage that is naturally added to the input voltage leading to the complete wrong calculation of the gain. Let's consider as an example an operational amplifiers with $A_v^{OL} = 100\ dB$ and imposed input voltage $V_{in} = 5\ V$, the DUT input voltage is $V_{out} = V_{in}/A_v^{OL} = 50\ \mu V$. Some micro volts of offset voltage have a big impact on the measurement, this is particularly true during irradiation when the offset voltage is expected to increase.
This problem is faced by performing multiple measurements at different input voltages.

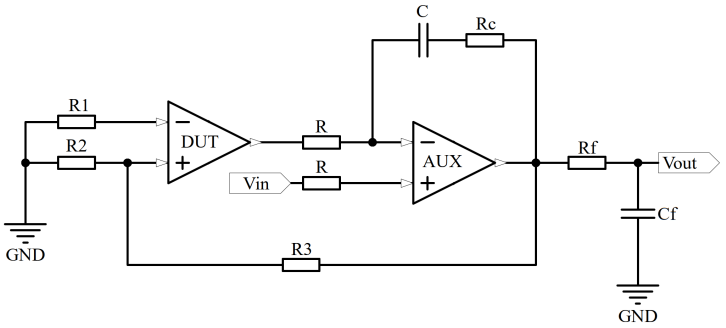

Figure 3.3: Operational amplifiers open loop gain test circuit.

The procedure will be discussed in detail in the chapter 4.

Since the auxiliary amplifier cannot be placed outside the irradiation area, it should be tolerant to mixed field radiation. A good candidate is the OP07 from Analog Devices whose tolerance to mixed fields has been demonstrated in literature: in [24] it was tested in a mixed field facility and the degradation of its parameters (input bias current, input offset voltage and open loop gain) was negligible up to 500 Gy and $2 \times 10^{13}\ 1MeVn - eq/cm^2$. In this particular case, in which it is used as auxiliary amplifier in integrator configuration, the most important parameter is the open loop gain: in order to have a measurement error lower than 1% the gain of the auxiliary amplifier has to be higher than 100 dB and, according to [24], the OP07 complies with this requirement.
The only issue that can arise during the tests at CHARM is the enhanced low dose rate

sensitivity [49]. The OP07 is a bipolar device and it could be affected by ELDRS, the test reported in literature was performed at high dose rate ($> 700\ Gy/h$) while at CHARM and CC60 it will be subjected to dose rates below 10 Gy/h, the expected degradation due to TID could be underestimated. For this reason, a couple of test at Cobalt 60 is proposed specifically to assess the sensitivity of the OP07 to low dose rates. It will be discussed later more in detail.

3.1.4 Output Voltage Drift

The scheme of the test circuit for the output voltage drift measurement is shown in Figure 3.4. The input voltage is fixed at V_{in} and the output voltage is acquired by the DAQ. At constant input voltage, the degradation of the output voltage is directly connected to the degradation of the amplifier parameters. The low pass filter placed at the output of the amplifier is aimed at reducing the noise.
The presented circuit is a simple example of the test circuit to explain its functioning, the real test circuits depend on the specific amplifier. Some amplifiers have a fixed gain, while others need a resistive feedback network to set the gain.

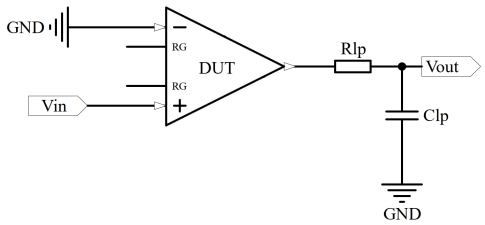

Figure 3.4: Instrumentation amplifiers output voltage drift test circuit.

3.1.5 Output Voltage Drift and Start-up Voltage Drift

The test circuits for the output voltage drift and start-up voltage measurements are shown in Figures 3.5(a) for the adjustable regulators and (b) for the fixed ones, the input voltage is imposed by the PSU and the output voltage is acquired by the DAQ, the measurement are performed at constant output current (fixed load R_{out}). The degradation of the start-up voltage is evaluated by varying the input voltage from 0 V to the maximum input voltage and measuring the output voltage. The start-up occurs when the regulator starts to regulate the output voltage. The input and output capacitance are needed to stabilize the output voltage, they are set based on the manufacturer specifics.

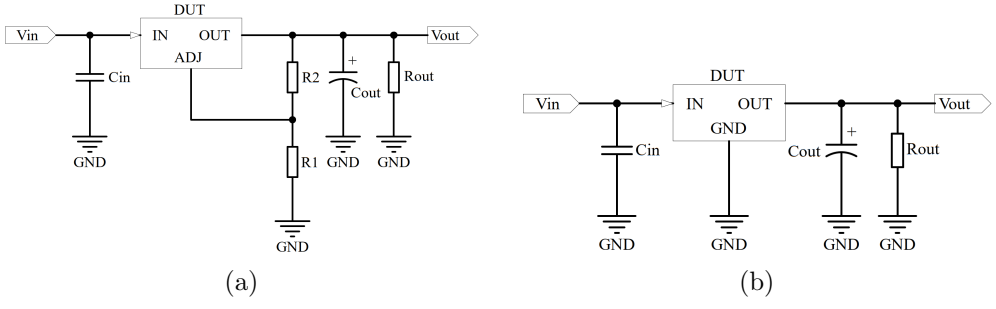

Figure 3.5: Test circtuits for the measurement of the output voltage drift and start-up voltage for (a) adjustable regulators/references and (b) fixed regulators/references.

3.1.6 Threshold Voltage Drift, Collector and Gate Leakage Currents

The test circuit for the IGBT parameters measurement is depicted in Figure 3.6, the threshold voltage is measured by sweeping the input voltage and reading the output current. The leakage currents are measured by measuring the voltage drop across the two resistors R_G and R_C during all the irradiation.

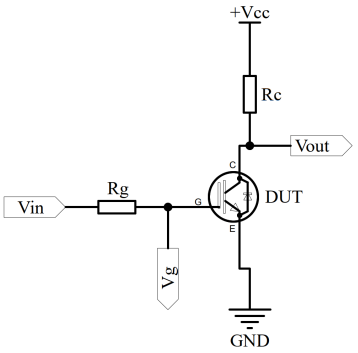

Figure 3.6: IGBT threshold voltage and leakage currents test circuit.

3.1.7 Threshold Current and Drain Leakage Current

Figure 3.7 shows the test circuit for the threshold current and drain current leakage measurements. The drain leakage current is measured through the drain resistor when the input current is set to 0 A. The threshold input current is measured by sweeping the input current and measuring the output current, when the output stage switches on, the drain current reaches its maximum value set by the drain resistor.

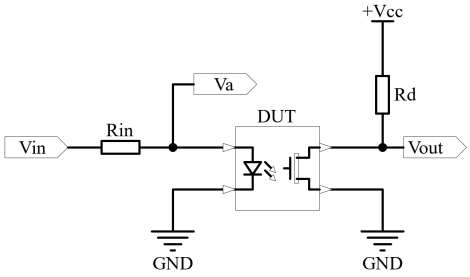

Figure 3.7: PhotoMOS threshold current and leakage current test circuit.

3.2 Test Boards

I designed the test boards taking into account the total number of devices to be tested and the acquisition channel availability. As will be explained later more in details, the maximum number of differential channels is 44. According to these constraints, the boards are organized as in Table 3.2.

The three boards designed for the radiation tests are visible in Figures 3.8(a), (b) and (c): the first one mounts operational amplifiers, three voltage regulators and one voltage reference, the second one mounts the instrumentation amplifiers, the other three voltage

Board	Type of Component	Reference
1	Operational Amplifier	AD829JRZ LM358AD MAX4238AUT+T LT1013
	Voltage Regulator	LM2936MP-5.0 TPS73033 LT1763IS8
	Voltage Reference	MAX6350
2	Instrumentation Amplifier	INA326 AD621 AD8420 MAX4208
	Voltage Regulator	LT1085 MAX8881EUT50 MIC29302
	Voltage Reference	ADR435TRZ-EP
3	IGBT	AUIRG4PH50S IKW15N120BH6
	PhotoMOS	PVA3354NS AQW210S VOR1142M4 ASSR-1218-003E

Table 3.2: Tested components divided into three boards.

regulators and the second voltage reference, the third one mounts the IGBTs and the photoMOS.
For each type of devices, in the corresponding test board, the number of tested components is 5 for each test circuit.
The large number of devices and the limited number of acquisition channels due to the facility constraints pose a challenge in the acquisition of all the parameters. The problem is solved by mounting several relays (white devices in Figures 3.8) that switch the output channels between two different DUTs. In this way the real number of acquisition channels doubles.
All the input voltages, both supply and signals, are provided through the Sub-db25 connectors (in grey in the figures), while the output voltages are acquired through the Sub-db78 connectors (in black in the figures). Unlike the number of output channels that is fixed for all the boards, the number of inputs depends on the devices under test. Boards 1 and 2 need two connectors for the supply voltages because they host simultaneously bipolar and BiCMOS integrated circuits, these types of devices have typically very different ranges of input voltages. BiCMOS devices have lower input/supply voltages, for example the voltage regulator TPS73033 has $5V$ as maximum input voltage, the amplifier MAX4238 has $5V$ as maximum supply voltage, while bipolar devices can withstand higher voltages, for example the amplifier $LT1013$ has supply voltage equal to $12V$. Thus, these boards have six power supply channels (four for the amplifiers and two for the voltage

reference/regulators), one channel for the amplifiers input voltage, and one channel for the relays supply.
The board 3, that mounts IGBTs and PhotoMOS, has only one power supply connector because the input channels are limited to five: PhotoMOS drain voltage and input voltage, IGBTs collector voltage and gate voltage and the relays supply.

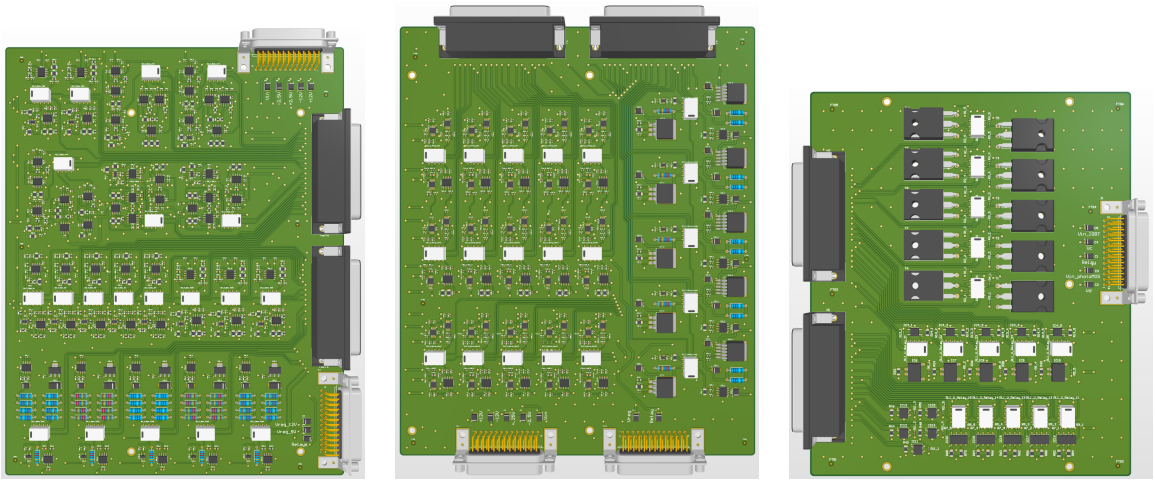

(a) (b) (c)

Figure 3.8: Test boards. (a) Board 1: operational amplifiers, voltage reference and voltage regulators. (b) Board 2: instrumentation amplifiers, voltage reference and voltage regulators. (c) Board 3: IGBTs and photoMOS.

3.2.1 Auxiliary Amplifier OP07 ELDRS

I designed a couple of identical test boards dedicated to the OP07 radiation tests, the 3D view of the board is visible in Figure 3.9. These boards are composed by the same test circuits proposed for the tests of the operational amplifiers: input bias current, input offset voltage and open loop gain.
The Sub-db25 connector, as in the previous boards, is used to provide the input voltages, in particular: power supply and amplifiers input voltage. The Sub-db78 connector is used to acquire the output voltages.

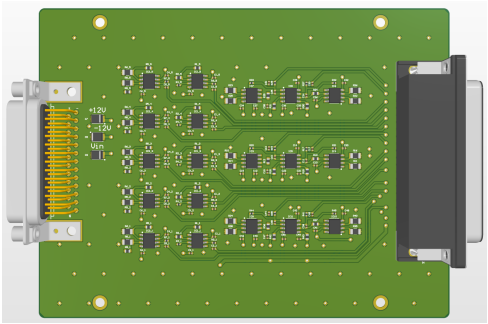

Figure 3.9: Test board for the evaluation of the enhancement low dose rate sensitivity (ELDRS) of the auxiliary amplifier OP07.

3.3 Test Facilities and Planning

The combined effects of total ionizing dose and displacement damage are evaluated by exposing the same device to several radiation environments that differ from each other

in the ratio between DDEF and TID. The test facilities I chose for this purpose are the Cobalt 60 and the CHARM facilities. The first one is used to have a reference on the effects of TID on the devices, while the second one is used to perform the combined TID-DD radiation tests at different DDEF/TID.
This section presents an overview of these test facilities, the planning of the test campaigns and the explanation of the setups.

3.3.1 CHARM Facility

The CERN High energy AcceleRator Mixed-field facility (CHARM) is located in the CERN East Area and it is the main facility used for testing the electronic components and systems in a mixed field radiation environment. Its peculiarities are the large irradiated area and the equivalence between its energy spectrum and the LHC spectrum. These properties allow to test entire systems in a radiation condition that simulates accurately the LHC environment.
The areas of the facility used by the users are mainly three: preparation room, control room and irradiation room. The preparation room is used to prepare the setup that must be installed in the irradiation room and the rack with the equipment that must be placed in the control room. The control room hosts all the racks with the measurement instruments and power suppliers for all the users running a test and, finally, the boards and the systems to be tested are placed in the irradiation room. The connection between the racks in the control room and the test boards in the irradiation room is made through two identical patch panels, one for each room. These two patch panel are connected with approximately 15m of cables.
Figure 3.10(a) is a representation of the CHARM irradiation room. The patch panel

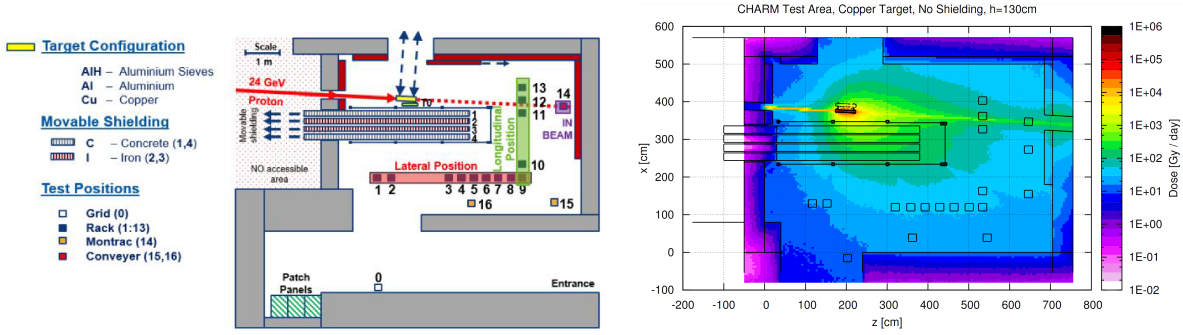

(a) (b)

Figure 3.10: CHARM irradiation room: (a) target, shields and test positions, (b) FLUKA simulations of the radiation field [50].

connected to the control room is located in the bottom left of the figure, the distance between the patch panel and the test position R13 (the green "13" in the figure) is approximately 15 meters and it is the maximum length the cable chain must cover to allow the connection of the test boards in all the positions. The boxes labeled with numbers represent the available test positions: from 1 to 13 the setup is installed on a rack moved with an automated conveyor system, in 15 and 16 it is installed on a mini rack moved by an overhead conveyor, the position 14 is reached by installing the setup in the Montrac that can be moved with a rail system and, finally, point 0 is a grid in which the setups are installed manually. In the center of the room, there are four movable protective shields depicted: the two outer ones are made of concrete, while the two inner ones are made of iron.

Figure 3.10(b) shows the simulation of the radiation field inside the irradiation room in operation: the 24 GeV proton beam coming from the CERN Proton-Synchrotron (PS) enters from the small aperture in the left and hits the target, the beam itself and the debris generated in the collision with the target are responsible of the mixed TID-DD radiation field. The dose rate varies depending on the position: near the target or the beam the dose rate is maximum, while in the more lateral positions (bottom of the figure) the dose rate is minimum. However, every test performed at CHARM can be considered a low dose rate test because the dose rate range goes from approximately 80 Gy/day to approximately 20 Gy/day.

The composition of the radiation environment in terms of ratio DDEF/TID and the dose rate to which the devices under test are subjected can be modified by changing three parameters:

- Material of the target
- Position of the shields
- Position of the devices under test

The effects of these parameters on the DDEF/TID ratio are depicted in Figure 3.11 concerning some target materials and shields configurations [51].
The target material can be Copper (Cu), Aluminum (Al) or Aluminum Sieve (AlH), the interaction between the proton beam and the different materials causes different debris and consequently different radiation environments.
The four shields can be moved independently allowing for various configurations, the effects of the shields are most evident in the lateral test positions for which the shields in position remain exactly between the device under test and the target, as can be seen in Figure 3.11, the test positions close to the beam (R11-R12-R13) are not affected by the introduction of the shields.

Finally, the position inside the irradiation room is crucial to determine the radiation

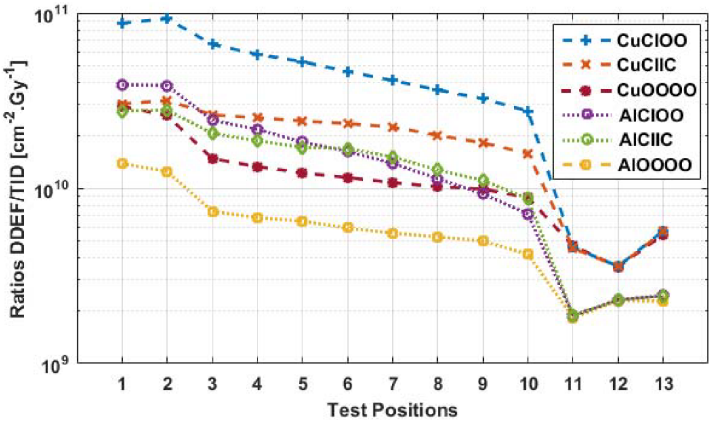

Figure 3.11: Distribution of the ratio DDEF/TID in the different CHARM locations, different target and configurations [26].

levels and DDEF/TID ratio, in fact, the positions close to the beam are subject to an higher dose rate and a low DDEF/TID ratio, while the lateral positions (from R1 to R10) are subject to lower dose rates and higher DDEF/TID ratios.
By exploiting these three methods it is possible to expose the devices under test to wide range of DDEF/TID ratios, from $\sim 10^9$ to $\sim 10^{11}$ $\frac{1MeVn-eq/cm^2}{Gy}$.

3.3.2 Cobalt 60 Facility

The Cobalt 60 facility (CC60) is used at CERN to perform pure TID radiation tests [52]. Figure 3.12 shows the layout of the facility, the sarcophagus in green inside the irradiation area contains the ^{60}Co isotopes that decay releasing gamma rays with energy of 1.172 MeV and 1.332 MeV [27]. In red is highlighted the device under test placed above a moving table. The possibility to move the table allows testing with a wide variety of dose rates: from hundreds of Gy/h to less than 1 Gy/h. The connections between the

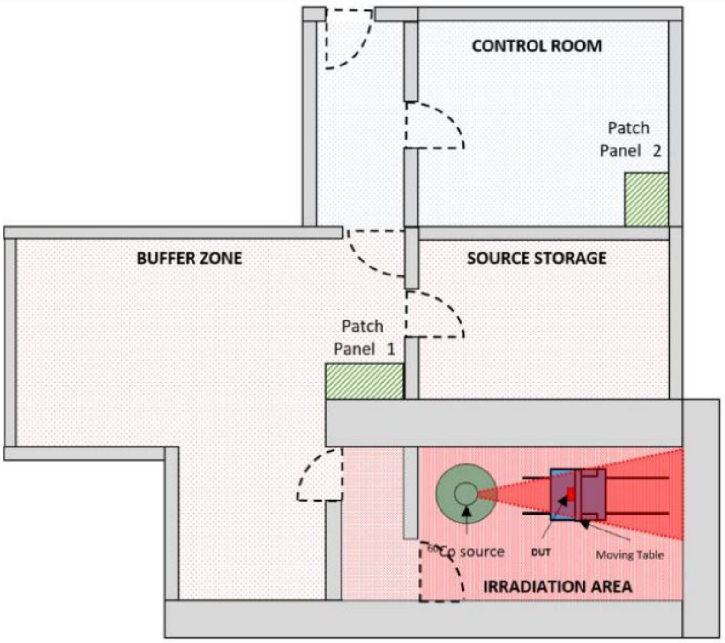

Figure 3.12: Layout of the Cobalt 60 facility [27].

devices in the irradiation room and the equipment are made through the patch panel in the buffer zone. The rack with the measurement instruments is positioned near the patch panel.

3.3.3 Test Campaigns Planning

Enhanced Low Dose Rate Sensitivity OP07

The reliability of the measured data from the test circuit in Figure 3.3 is strongly related to the auxiliary amplifier under mixed field irradiation. As mentioned in the paragraph 3.1.3, OP07 is a good candidate since it has been shown to withstand high radiation levels. To assess the problem of the possible enhanced low dose rate effects, I proposed a couple of test: an High Dose Rate (HDR) test and a Low Dose Rate (LDR) test. These two tests allow determining the degradation levels of the two plateaus of the typical ELDRS characteristic (already explained in Figure 1.7(a)) and the enhancement factor. Table 3.3 summarize the irradiation conditions of the two tests.

The HDR test set the reference for the degradation, the dose rate is in the same order of magnitude of the dose rate used in [24]. The dose rate for the LDR test is chosen to be lower than the CHARM dose rate, for time restrictions the total dose cumulated during the low dose test is lower than the HDR one, but it is sufficient to extrapolate the enhancement factors for the tested parameters.

Test	Dose Rate $\left[\frac{Gy}{h}\right]$	Total Dose $[Gy]$
HDR	230	500
LDR	0.5	240

Table 3.3: Irradiation condition for the Enhanced Low Dose Rate test of the auxiliary amplifier OP07

Pure TID tests

The tests at Cobalt 60 facility are fundamental to fix the degradation profile of all the tested devices in presence of ionizing radiation alone. In fact, gamma radiation can induce charge trapping inside the oxides and interface states, but it cannot induce displacement damage. Consequently, the resulting degradation profiles are associated to the ratio $DDEF/TID = 0$.
I chose the dose rate taking into account three factors:

- CHARM dose rate: the dose rate of the pure TID tests must be close to the CHARM dose rate, otherwise the discrepancies in the results could be attributed to dose rate effects.
- Cumulative ionizing dose: the amount of TID accumulated during the irradiation must be equal to or greater than that accumulated during tests at CHARM.
- Test time: the dose rate has to be high enough to ensure reasonable test duration considering three test boards.

Based on these factors, the chosen dose rate for the pure TID tests at Cobalt 60 facility is 5 Gy/h.
This test is repeated three times, one for each board presented in the section 3.2, to evaluate the TID contribution to the damage of all the studied devices.

Combined TID-DD tests

To assess the combined effects of total ionizing dose and displacement damage, each device is exposed to several tests in different radiation environments in terms of DDEF/TID ratio. As explained previously, at CHARM there are three methods to change the radiation environment to which the DUTs are exposed. Since the facility is used by many users at the same time, the configuration of the target and the shielding must be compatible with all the necessities of the users. For this reason, during all the tests of this study, the configuration is fixed to CuOOOO: the target material is copper and the shields are not moved inside the irradiation room.
The only remaining way to change the radiation environment is the change of test position. The selection of the test position is driven by several restrictions: test time, number test boards and accumulated total dose for each device. Since the total number of test boards is three, three test must be performed in each position, in addition, the first two boards must accumulate approximately 500 Gy, the third one must accumulate approximately 200 Gy and, remembering that the CHARM dose rate goes from ~ 80 Gy/day to ~ 20 Gy/day, the duration of a single test can go from one week to 3-4 weeks. For this reason, I selected three positions to conduct the study: R11, R8 and R1 visible in Figure 3.13.
These three locations are characterized by different dose rates and DDEF/TID ratios as reported in Table 3.4, the farther is the position from the beam trajectory, the lower the dose rate and the higher the DDEF/TID ratio.

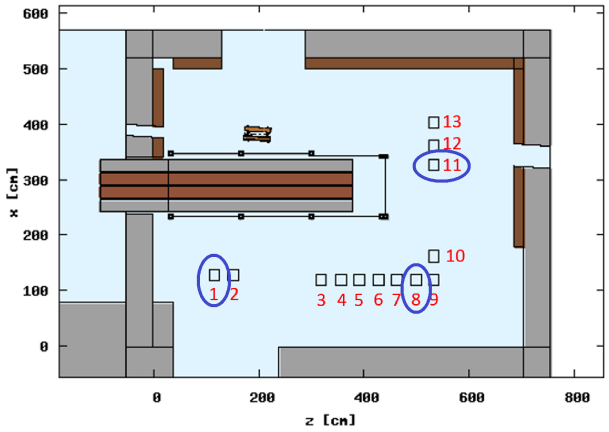

Figure 3.13: Selected test position of the CHARM irradiation room.

Configuration	Position	DDEF/TID $\left[\frac{1MeVn-eq/cm^2}{Gy}\right]$	Dose Rate $\left[\frac{Gy}{day}\right]$
CuOOOO	R11	$6.8 \cdot 10^9$	60
	R8	$9.8 \cdot 10^9$	44
	R1	$2.4 \cdot 10^{10}$	23

Table 3.4: Average dose rates and DDEF/TID ratios measured during the tests in the selected CHARM test positions in the available configuration CuOOOO.

In summary, each reference under test is tested four times: one time at CC60 to fix the TID degradation and three times at CHARM (in different positions) to evaluate the combined TID-DD effects at different ratios DDEF/TID. With the four resulting degradation profiles, it is possible to understand the nature of the degradation, if it is caused only by one of the two contributors (TID or DD), or if it is caused by the combination of TID and DD. In the last case, it is also possible to understand if the devices are sensitive to synergistic TID-DD effects by checking how the two contributions to the damage can be combined to obtain the overall degradation.

3.4 Test Setups

In this section the test setups for the two facilities will be discussed, for each facility only one setup is presented because the setups developed for the same facility are very similar.

3.4.1 CHARM Setups

The setup I prepared and used in the CHARM facility for the tests of the boards 1 and 2 is depicted in Figure 3.14.
The rack placed in the control room is equipped with one MultiDAQ Keysight 34980 with two modules 4924A that allow the connection of four Sub-db78 data acquisition cables, the presence of a second acquisition module gives the opportunity to test two boards at the same time. Since boards 1 and 2 have the same minimum TID requirement ($\sim 500\ Gy$), they are tested at the same time, while the board 3 is tested alone and requires the use of only one data acquisition module. Three power supply units (PSUs), two Keysight N6705B and one Agilent E3631A, are used for the supply and input voltages for the test boards. The first one is used for the power supplies of the amplifiers of boards 1 and 2: two channel for $\pm 12\ V$ (Vc and Ve in figure) and the other two channels for $\pm 2.5\ V$ (Vd

and Vs in figure). The second power supply is used for providing the input voltage to the voltage regulators and references, the supply for the relays and the input voltage for the operational amplifiers (Vreg1, Vreg2, Vin and Vrelay in figure). The third power supply provides only the input voltage for the instrumentation amplifiers (Vin2).
During the test of the board 3 the first PSU is used to provide the drain voltage and the input current to the PhotoMOS and the collector and gate voltages to the IGBTs, the second PSU is used for the relay voltage and the third one is not used.
All the instruments are connected to the PC running the firmware through ethernet cables.

The MultiDAQ is connected to the NE48 connectors of the patch panel in the con-

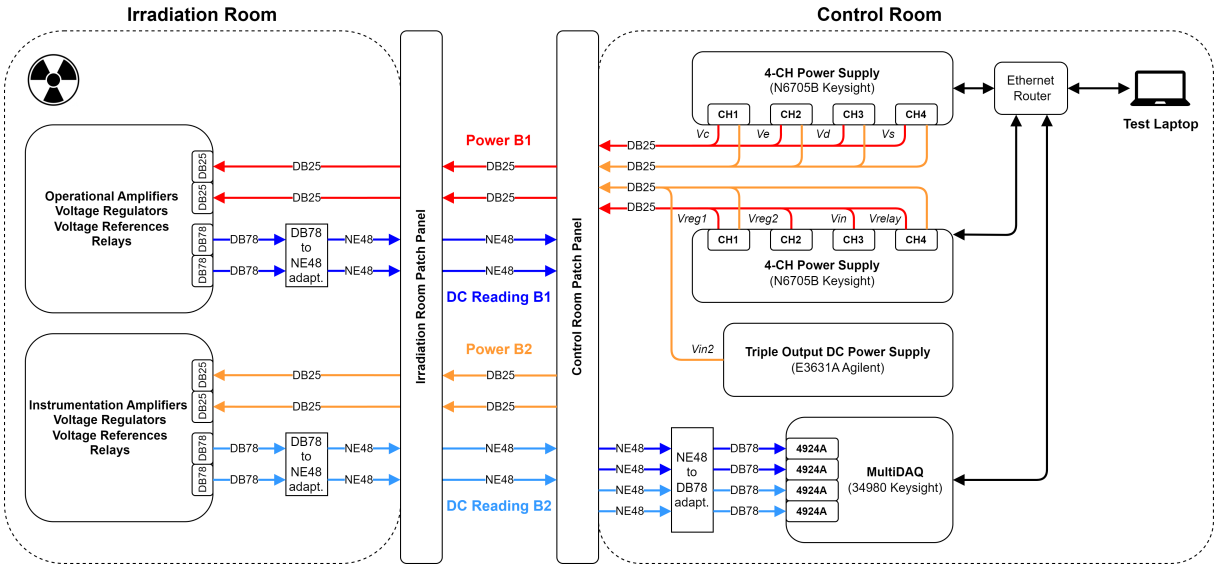

Figure 3.14: Test setup for the first and second boards: operational amplifiers, instrumentation amplifiers, voltage references and voltage regulators.

trol room via four Sub-db78/NE48 adapters, this is the reason of the restriction on the number of acquired channels. A single module of the MultiDAQ can acquire up to 70 differential channels through two Sub-db78 connectors, but the CHARM patch panels are not equipped with this type of connector and the change between Sub-d78 to NE48 is necessary. Each NE48 cable can host 22 acquisition channels, in this adaptation the number of acquired channels for each module is reduced from 70 to 44. Concerning the power suppliers, they are connected to the patch panel with four Sub-db25 cables. Each cable can host up to 6 power channels.
A 15m cable chain for the irradiation room was realized specifically to contains the NE48 and Sub-db25 cables to connect the patch panel in the irradiation room to the rack mounting the test boards. At the end of the chain, the Sub-db25 cables are connected directly to the test boards, while the NE48 cables are connected to NE48/Sub-db78 adapters that are finally connected to the test boards.
From the rack inside the control room to the test boards there are approximately 40 meters of cables.

The test boards are placed in a dedicated standalone rack that can be moved easily inside the irradiation room, the cable chain is placed on the floor and the dosimetry is acquired with a RadMON deported module placed at the center of the plane that contains the boards. Figures 3.15(a), (b) and (c) show the rack inside the CHARM irradiation room in the three test positions R1, R8 and R11. In the pictures the rack hosts the boards 1 and 2, the installation of the board 3 is equivalent. The deported module is visible in

(a) (b) (c)

Figure 3.15: Board 1 and 2 (operational amplifiers, instrumentation amplifiers, voltage references and voltage regulators) inside the CHARM irradiation room: (a) position R1, (b) position R8 and (c) position R11.

Figure 3.15(a) between the two boards.

3.4.2 Cobalt 60 Setups

The setup I prepared for the Cobalt 60 facility is depicted in Figure 3.16. Only one board can be tested at a time and only two PSUs are necessary. The channels of the two PSUs are used in the same way as CHARM, the names associated with the 8 channels shown in the two figures are the same. Since the boards 1 and 2 are not tested at the same time, the channel Vin can be used for the input voltage of both operational amplifiers (board 1) and instrumentation amplifiers (board 2), without the need of a third PSU.
The MultiDAQ is connected to the test board directly with two Sub-db78 cables. The voltages from the PSUs are carried into the irradiation room through coaxial cables that are converted into Sub-db25 near the test board. The instruments are connected to the PC in which the firmware is running via ethernet cables.

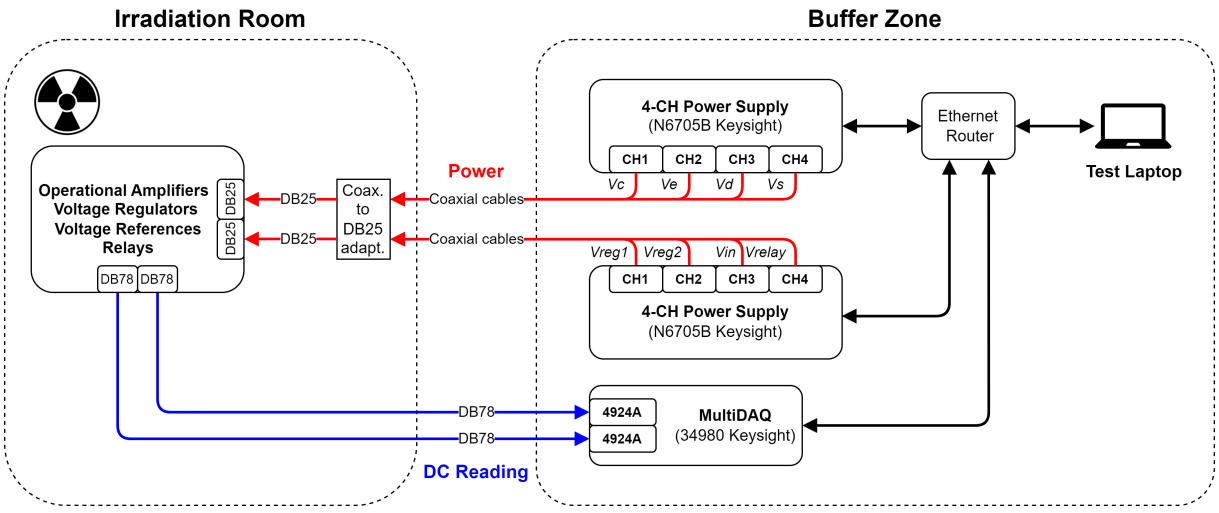

Figure 3.16: Test setup of the first board (operational amplifiers, voltage references and voltage regulators) for the Cobalt 60 facility.

Figures 3.17(a) and (b) and Figure 3.18 show some examples of the test boards placed

inside the CC60 irradiation room. Figure 3.17(a) shows the high dose rate test board positioning inside the irradiation room, the board is very close to the aperture of the sarcophagus to have an high dose rate (230 Gy/h). While the test board positioning for the low dose rate test is depicted in Figure 3.17(b), the board is placed in the corner of the irradiation room in order to receive a very low dose rate (0.5 Gy/h). Figure 3.18 shows an

(a) (b)

Figure 3.17: OP07 ELDRS test board placement inside the CC60 irradiation room. (a) High dose rate irradiation: the board is placed close to the sarcophagus aperture. (b) Low dose rate irradiation: the board is placed in the peripheral wall in front of the sarcophagus aperture.

example of the installation of one of the three test boards developed for the study. The board is approximately in the middle of the irradiation room in front of the sarcophagus aperture. The dose rate is measured before each test with an ionization chamber.

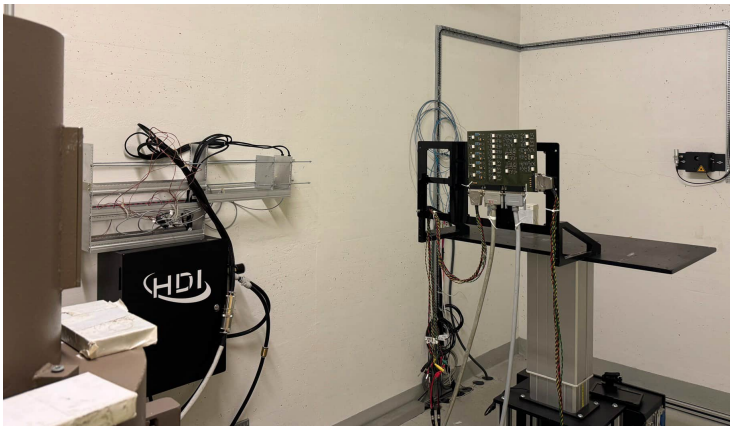

Figure 3.18: Example of test board positioning inside the Cobalt 60 irradiation room.

3.4.3 Data acquisition firmware

The degradation profiles are obtained by automatically measuring the tested parameters with a Python firmware I developed specifically for this purpose. Due to the large number of devices and acquisition channels, the firmware is not realized for the real time plot of the measures. the script takes care of controlling the power supply units (PSUs) and the MultiDAQ in order to impose the input signals and acquire the output voltages.
The basic diagram of the firmware is shown in Figure 3.19. The high level application, a basic graphical user interface (GUI), is used to control the acquisition algorithm that runs in background. The acquisition algorithm is a three state machine in which the state change is triggered by the GUI. The states of the machine are the following:

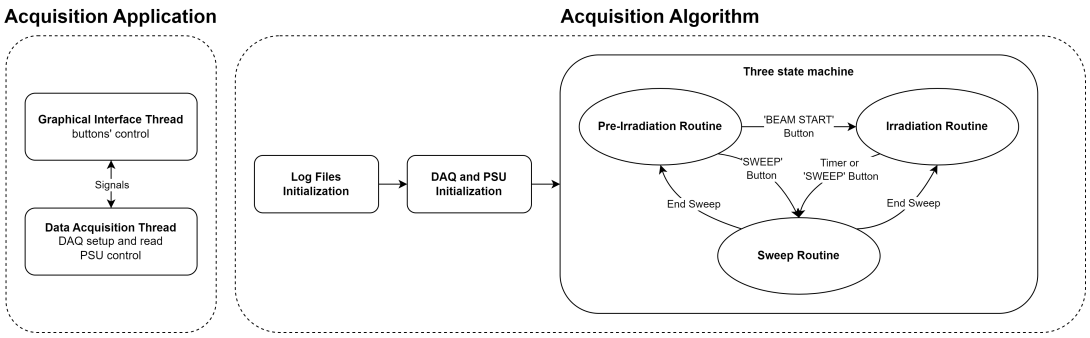

Figure 3.19: Diagram of the data acquisition firmware.

- Pre-irradiation state: the program is started, the power supply is provided to the test boards and the continuous acquisition is started.
- Irradiation state: when the irradiation is started, the continuous acquisition is active and the sweep state is called periodically.
- Sweep state: state in which some input voltages are swept allowing the extrapolation of some devices' parameters (i.e. the threshold voltage of the IGBTs).

Figures 3.20(a), (b) and (c) show the firmware routines of the three states. During

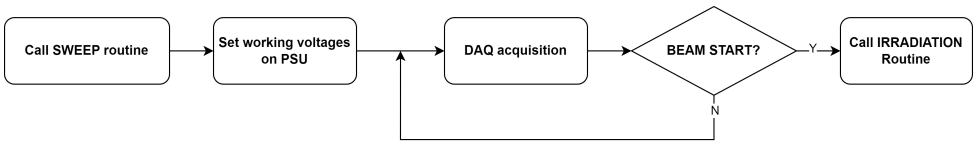

(a)

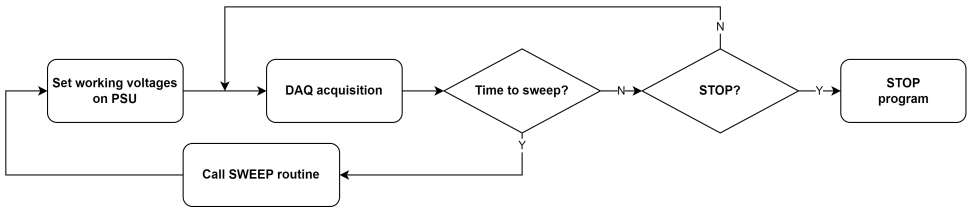

(b)

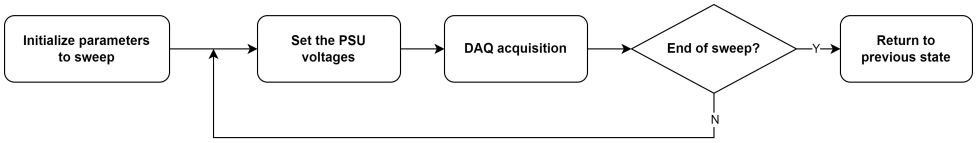

(c)

Figure 3.20: Routines associated to the three states of the firmware: (a) pre-irradiation state, (b) irradiation state and (c) sweep state.

pre-irradiation state the sweep routine is called once and then the measured voltages are acquired continuously until the "Beam Start" button is pressed, this button should be pressed in correspondence of the irradiation start but it is not strictly necessary, it can be pressed before the actual start of irradiation, in fact, in post-processing it is possible to associate the dosimetry measurements with the acquired voltages according to the timestamps. In the irradiation state the acquisition of the voltages continues and the sweep routine is called periodically, the period (in gray) can be chosen by the user, a standard choice is a sweep every 10 Gy. Finally, during the sweep routine the parameters to sweep are set every cycle to have a ramp input, at each step an acquisition

is performed. This procedure allows the extrapolation of some electrical parameters, such as the threshold voltage of the IGBTs or the start-up voltage/current of the voltage regulators and photoMOS respectively.
The result is the acquisition of the entire degradation profile of the devices during the irradiation with the addition of several periodic measurements of parameters that cannot be measured continuously, but which require an input voltage ramp to be extrapolated.

Chapter 4

Test Results and Analysis

This chapter is structured in a first part in which the methods I used during the analysis are explained, subsequently, all the results are discussed by type of devices and, finally, their impact on the CERN RHA are presented. In the following paragraphs, in particular in the combined TID-DD results evaluation, it is important to remember that the positions CC60, R11, R8 and R1 are in ascending order of DDEF/TID ratio: $\frac{DDEF}{TID}\big|_{CC60} < \frac{DDEF}{TID}\big|_{R11} < \frac{DDEF}{TID}\big|_{R8} < \frac{DDEF}{TID}\big|_{R1}$. At same cumulated dose, the devices tested in position R1 are affected by more displacement damage respect to the devices tested in the other positions.
Given the high number of devices and test positions, I analyzed the results at high level, a further in-dept analysis would require the extrapolation and the simulation of all the internal circuits of the devices.

4.1 Methods

4.1.1 Open Loop Gain Extraction

As already mentioned in the subsection 3.1.3, the open loop gain measurement is affected by the input offset voltage of the DUT. The output voltage measured by the MultiDAQ depends on three parameters: the input voltage, the open loop gain and the offset voltage.

$$V_{out} = \left(\frac{V_{in}}{A_v^{OL}} + V_{off} \right) \cdot \frac{R_2 + R_3}{R_2} \tag{4.1}$$

The names of the resistances refer to Figure 3.3.
Consequently, the open loop gain calculus should take into account the offset voltage in the following way.

$$A_v^{OL} = \frac{V_{in}}{V_{out} \cdot \frac{R_2}{R_2+R_3} - V_{off}} \tag{4.2}$$

The input voltage and the output voltage are directly measured by the MultiDAQ, but the offset voltage is unknown and the average value obtained by the dedicated test circuit is not precise enough to get a reliable value of open loop gain.
However, considering the input voltage as dependent variable and the output voltage as independent variable, it is possible to write the relation between these two variables as a linear function in which the slope depends on the open loop gain and the y-intercept depends on both the offset voltage and the gain.

$$V_{in} = A_v^{OL} \left(\frac{R_2}{R_2 + R_3} \cdot V_{out} - V_{off} \right) = A_v^{OL} \cdot \frac{R_2}{R_2 + R_3} \cdot V_{out} - A_v^{OL} \cdot V_{off} \tag{4.3}$$

Mathematically, two measurements at different V_{in} values are sufficient to extrapolate both A_v^{OL} and V_{off}. To make the estimation more reliable, the procedure I proposed consist in several measurements at various V_{in} values followed by the maximum likelihood estimation of the parameters. The two estimated parameters are related to A_v^{OL} and V_{off} as follows.

$$\begin{cases} \hat{\theta}_1 = A_v^{OL} \cdot V_{off} \\ \hat{\theta}_2 = A_v^{OL} \cdot \frac{R_2}{R_2+R_3} \end{cases} \tag{4.4}$$

The estimation of these two parameters is done by linear regression: considering $\bar{V}_{in}$ the vector of the input voltages and $\bar{V}_{out}$ the vector of the output voltages, the relation can be written in the matrix form.

$$V_{in} = \hat{\theta}_1 + \hat{\theta}_2 \cdot V_{out} \Rightarrow \bar{V}_{in} = \Phi \cdot \hat{\theta} \tag{4.5}$$

With

$$\Phi = \begin{bmatrix} 1 & V_{out_1} \\ 1 & V_{out_2} \\ \vdots & \vdots \\ 1 & V_{out_n} \end{bmatrix} \text{ and } \hat{\theta} = \begin{bmatrix} \hat{\theta}_1 \\ \hat{\theta}_2 \end{bmatrix} \tag{4.6}$$

Finally, the estimated parameters are calculated using the standard linear regression formula in matrix form.

$$\hat{\theta} = \left(\Phi^T \Phi\right)^{-1} \Phi^T \bar{V}_{out} \tag{4.7}$$

4.1.2 Uncertainty in the Measurements

The comparison between degradation profiles of the same device acquired in different radiation environments is made by comparing the values obtained by averaging the responses of the devices subjected to the same environment and taking into account also the variance of the profiles.
I calculated the mean and the variance of the profiles point-wise with the unbiased estimators reported in Equations 4.8 and 4.9.

$$\mu = \frac{\sum y_i}{N} \tag{4.8}$$

$$\sigma^2 = \frac{\sum (y_i - \mu)^2}{N-1} \tag{4.9}$$

With y_i samples and N number of samples. From now on, μ refers to the estimation of the mean and σ^2 to the estimation of the variance.
All the measurement acquired by the MultiDAQ are affected by random errors due to the thermal noise, the voltage noise of the DUT and the uncertainty of the measurement instrument. These errors don't affect the estimation of the mean because their expectancy is zero.

$$Y_M = Y + \varepsilon \Rightarrow E[Y_M] = E[Y] + E[\varepsilon] = E[Y] \tag{4.10}$$

With Y_M measured variable, Y ideal variable and ε measurement error.
But these errors affect the estimation of the variance that becomes larger than expected.

$$Var(Y_M) = \sigma_Y^2 + \sigma_\varepsilon^2 \tag{4.11}$$

However, this is not a big issue because the variability of the degradation profiles of the devices under test is usually larger than the variance associated to the measurement error.

Each measure is associated to a cumulative ionizing dose value obtained through the RadMON deported module placed close to the test boards. The error on the dosimetry estimation is approximately $\varepsilon_{\%} = 10\%$. Since the measures are performed at the same time, they are affected by the same outcome of the random variable that can represent the dosimetry uncertainty. As a consequence, the variance estimation of the run is not impacted by this error. But in a comparison of measurements done in different runs this error plays a crucial role. In fact, different runs corresponds to different realization of the dosimetry error random variable. For this reason, I took into account the dosimetry error as error of the mean considering the $\varepsilon_{\%}$ as one standard deviation.

$$\sigma^2_{\mu|TID} = \sigma^2_{\mu} + \sigma^2_{TID} \tag{4.12}$$

With μ the unbiased estimation of the mean of the samples Y.
In case of dose measurements, as in the case of abrupt degradation, the uncertainty is simply added.

$$\sigma^2_{\mu|TID} = \sigma^2_{\mu} + \sigma^2_{TID} = \frac{\sigma^2}{n} + (\mu \cdot \varepsilon_{\%})^2 \tag{4.13}$$

In case of gradual degradation, the impact of the dosimetry uncertainty can be translated into measure uncertainty by exploiting the error propagation.

$$\sigma^2_{TID} = \left(\frac{d\mu}{dTID} \cdot TID \cdot \varepsilon_{\%} \right)^2 \tag{4.14}$$

This error is added to the variance of the mean as follows.

$$\sigma^2_{\mu|TID} = \sigma^2_{\mu} + \sigma^2_{TID} = \frac{\sigma^2}{n} + \left(\frac{d\mu}{dTID} \cdot TID \cdot \varepsilon_{\%} \right)^2 \tag{4.15}$$

All the shaded ranges above and below the mean value profiles plotted in the following section represent a standard deviation calculated as the square root of Equation 4.15.

4.1.3 Synergistic Effects Evaluation

The general procedure I adopted to evaluate the presence of synergistic effects is the hypothesis testing: the null hypothesis (H_0) is the absence of synergistic effects and the aim of the test is to verify if this hypothesis can be rejected.
The first step is to define mathematically the null hypothesis. I made the following assumption: in absence of synergistic effects the degradation profile is the result of the additive contributions of TID and DD. This is the simpler way of proceeding, if two devices are located into different LHC locations and one has higher DDEF/TID ratio, it is reasonable assuming that at same ionizing dose, the device that suffered more displacement damage is the more degraded. The simpler way to account for that is to divide the overall degradation into two additive contributions.

$$\Delta P(TID, DDEF) = f(TID) + g(DDEF) \tag{4.16}$$

With P degraded parameter and f and g generic functions of TID and DDEF.
I can determine the left side of the equation by testing in a mixed-field facility (CHARM), and the first factor of the right side of the equation with the gamma irradiation tests at Cobalt 60 facility:

$$\Delta P_{CC60}(TID) = f(TID) \tag{4.17}$$

Then, I can extrapolate the contribution of the displacement damage by subtracting the TID contribution to the overall damage exhibited in the mixed field environment.

$$\Delta P_{CHARM}(TID, DDEF) - \Delta P_{CC60}(TID) = g(DDEF) \tag{4.18}$$

In absence of synergistic effects, regardless the position in which the test is done, the DD contribution to the damage is the same. Differences in the DD profiles suggest the presence of synergistic effects.

$$g_{R1}(DDEF) = g_{R8}(DDEF) = g_{R11}(DDEF) \Rightarrow \text{No synergistic effects} \tag{4.19}$$

The hypothesis testing in this case is performed with the Welch's t-test or the Analysis of Variance (ANOVA) depending on the number of groups of samples.
If the number of tested groups is two, the Welch t-test is the best choice. In this case the null hypothesis consists in the equivalence between the two estimated means.

$$H_0 : \mu_1 = \mu_2$$

The expected value of the difference between the estimated means is zero and the result follows t-student probability distribution.

$$t = \frac{\mu_1 - \mu_2}{\sqrt{\frac{\sigma_1^2}{n_1} + \frac{\sigma_2^2}{n_2}}} \tag{4.20}$$

With degree of freedom df.

$$df = \frac{\left(\frac{\sigma_1^2}{n_1} + \frac{\sigma_2^2}{n_2}\right)^2}{\left(\frac{\sigma_1^2}{n_1}\right)^2 \frac{1}{n_1 - 1} + \left(\frac{\sigma_2^2}{n_2}\right)^2 \frac{1}{n_2 - 1}} \tag{4.21}$$

With $\mu_{1,2}$ the estimated means, $\sigma_{1,2}^2$ the estimate variances and $n_{1,2}$ the numbers of samples of the two groups.
But the formula as it is doesn't take into account the dosimetry uncertainty because, as already mentioned, it affects the variance of the mean but not the sample variance. To include this uncertainty it can be noticed that the denominator of Equation 4.22 is nothing but the square root of the sum of the variances of the means. Therefore, I modified the formula by substituting the variance of the means with the variances reported in Equation 4.15 that takes into account the dosimetry uncertainty.

$$t = \frac{\mu_1 - \mu_2}{\sqrt{\sigma_{\mu_1|TID}^2 + \sigma_{\mu_2|TID}^2}} \tag{4.22}$$

The obtained t value is associated to the p-values that corresponds to the probability of having equal or more extreme t values. If the p-value is lower then a threshold the null hypothesis can be rejected.

If there are more than two groups to compare, another test can be used: Analysis of Variance (ANOVA) test. In this case, the null hypothesis is that all the means are equal.

$$H_0 : \mu_1 = \mu_2 = \cdots \mu_k$$

The idea of the test is to check whether the variances within the different groups is compatible with the variance between groups considering the groups as belonging to the

same population.
The first step is the calculus of the general mean μ_G: the estimation of the mean as if all the samples belong to the same population.

$$\mu_G = \frac{\sum n_i \mu_i}{\sum n_i} \tag{4.23}$$

With μ_i estimated mean and n_i number of samples of the group i.
The second step is the calculus of the numerator and denominator of the result, the numerator is an estimation of the variance as if all the samples belong to the same population, the denominator is a combination of the variances of the different tested groups.

$$F = \frac{\frac{\sum_i n_i(\mu_i - \mu_G)^2}{k-1}}{\frac{\sum_i (n_i-1)\sigma_i^2}{N-k}} \tag{4.24}$$

In this case, I considered the uncertainty of the dosimetry by making the sample variance such that the estimated variance of the mean is equal to $\sigma^2_{\mu|TID}$:

$$\sigma^2 \text{ t.c. } \sigma^2_\mu = \frac{\sigma^2}{n} = \sigma^2_{\mu|TID} \Leftrightarrow \sigma^2 = \sigma_i + n_i \cdot \sigma^2_{TID} \tag{4.25}$$

As a consequence, the formula is modified as follows:

$$F = \frac{\frac{\sum_i n_i(\mu_i - \mu_G)^2}{k-1}}{\frac{\sum_i (n_i-1)\sigma_i^2}{N-k} + \frac{\sum_i n_i(n_i-1)\sigma^2_{TID}}{N-k}} \tag{4.26}$$

The obtained value belongs to the probability distribution $F(k-1, N-k)$ from which it is possible to derive a p-value that represent the probability of having equal or more extreme F values. Also in this case, if the p-value is lower than a threshold, the null hypothesis can be rejected.
Intuitively, in both tests the addition of the dosimetry uncertainty increases the variance of each tested group, the result is a decrease of the F or t value and, consequently, the increase of the p-value. It is a conservative approach: the p-values tends to be higher if the denominator becomes larger.
The p-value obtained in both the t-test and the ANOVA test is a function of the displacement damage equivalent fluence (DDEF) because the evaluation is performed point-wise. Since all the results are very similar and the information can be extracted from the last points of the profiles, only one example will be showed in the next paragraphs, the other results will be reported numerically.

If there is an abrupt degradation of the tested parameter the subtraction of the CC60 profile can be ineffective, in this case I made another assumption: the abrupt degradation is due to the degradation of a device parameter that cannot be directly measured. Then, I supposed the degradation of this unknown parameter as linear and when it overcomes a threshold, the observable parameter exhibits an abrupt change. In this case the dependency on TID and DD in absence of synergistic effects results in the sum of TID and DDEF multiplied by two scaling factors k and h. Equation 4.27 represents the condition in which the parameter (P_{int}) overcomes a threshold (P_{TH}), this condition is associated to a couple of values of cumulated ionizing dose (TID_{BK}) and displacement damage equivalent fluence ($DDEF_{BK}$).

$$\begin{aligned} \Delta P_{int}(TID, DDEF) &= k \cdot TID_{BK} + h \cdot DDEF_{BK} = P_{TH} \\ &\Rightarrow \frac{1}{TID_{BK}} = k' + h' \cdot \frac{DDEF}{TID} \end{aligned} \tag{4.27}$$

Consequently, in the absence of synergistic effects, the relation between the inverse of the dose at which the device fails and the ratio DDEF/TID is linear. It is the simplest model that can be used and it is a reasonable assumption because at same cumulated ionizing dose, higher displacement damage results in earlier failure.
More complex relations between $1/TID_{BK}$ and $DDEF/TID$ suggest the presence of synergistic effects.

In the cases in which the presence of synergistic effects appears as linear relation between the data and the DDEF/TID ratio, I evaluated it with the reduced χ^2 test. This procedure verifies if the linear fit is a good choice for the available data.

$$\chi^2 = \sum_i \frac{(O_i - E_i)^2}{\sigma_i^2} \tag{4.28}$$

With O_i observations, E_i expected values and σ_i^2 variance of the observation.
The sum of the ratio between the squared difference of observation and expected value and the variance of the measurement has a χ^2 probability distribution with degrees of freedom df.

$$df = n - m \tag{4.29}$$

With n number of samples and m number of estimated parameters.
The reduced χ^2 is calculated as follows.

$$\chi^2_{df} = \frac{\chi^2}{df} \tag{4.30}$$

If the p-value associated to the χ^2 is lower than a threshold, the null hypothesis is rejected: the data cannot be fitted with a straight line and, consequently, there are evidences of synergistic effects.
For all the statistical tests, I chose the significance level equal to 5%: considering the null hypothesis true, if the probability of having equal or more extreme measured data is lower than 5% and, thus, a p-value lower than 5%, the null hypothesis can be rejected.

4.2 ELDRS evaluation of OP07

As described in section 3.3.3, I tested the auxiliary amplifier OP07 for Enhanced Low Dose Rate Sensitivity to validate the results of the paper [24] in terms of radiation tolerance. The parameters chosen for the test were the input bias current, the input offset voltage and the open loop gain.
The evaluation of the enhancement factors is restricted to the maximum dose achieved during the low dose rate test: 240Gy.
For each parameter, I calculated the enhancement factor as follows:

$$EF = \frac{\Delta P(TID)_{LDR}}{\Delta P(TID)_{HDR}} \tag{4.31}$$

The result is a function of the cumulated ionizing dose. I obtained the standard deviation of the calculated values with the error propagation formula.

$$\sigma_{EF} = \sqrt{\left(\frac{\sigma_{LDR}}{\Delta P(TID)_{HDR}}\right)^2 + \left(\frac{\Delta P(TID)_{LDR} \cdot \sigma_{HDR}}{\Delta P(TID)^2_{HDR}}\right)^2} \tag{4.32}$$

With σ_{HDR} and σ_{LDR} the estimated variances of the HDR and LDR samples respectively.

The input bias current degradation is depicted in Figure 4.1, the enhancement factor at the end of the irradiation is stable at 1.1 ± 0.6.

The behaviour of the offset voltage is different, as visible in Figure 4.2, the degradation

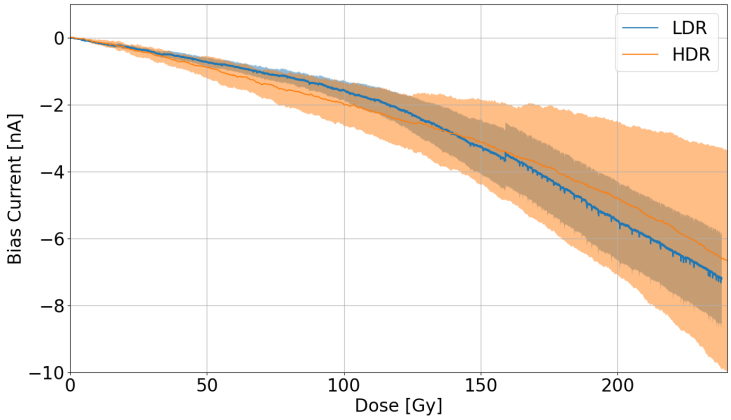

Figure 4.1: Comparison between the input bias current degradation of the operational amplifier OP07 at high dose rate (HDR) and low dose rate (LDR).

at low dose rate is negative, while the high dose rate profile can be divided into two parts: an initial part in which the degradation is negative and a second part (starting from 100 Gy) in which the degradation is positive. However, after the first part of the curve in which the behaviour of the HDR curve makes the enhancement factor explode because of the zero crossing, the EF becomes stable after 200 Gy at -1.9 ± 1.4.

Finally, the open loop gain decrease is depicted in Figure 4.3, it is slightly higher in the

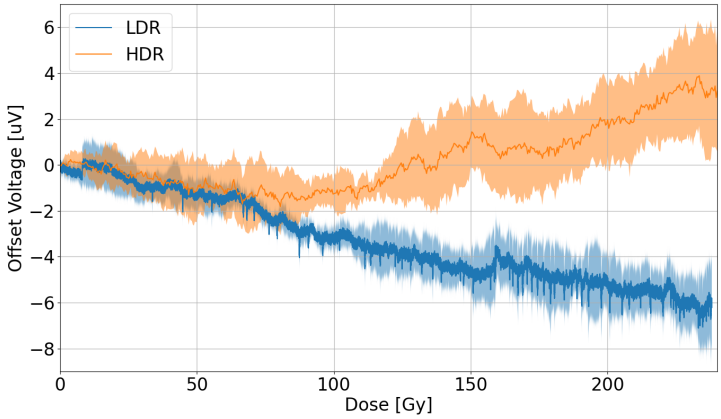

Figure 4.2: Comparison between the input offset voltage degradation of the operational amplifier OP07 at high dose rate (HDR) and low dose rate (LDR).

high dose rate condition and the enhancement factor is stable at 0.7 ± 0.1.

In conclusion, the operational amplifier OP07 does not exhibit a strong enhanced low dose rate sensitivity, all the tested parameters show low enhancement factors. The results on the open loop gain testing obtained with the contribution of the OP07 can be considered valid since its tolerance to mixed fields was demonstrated in [24] and the influence of the dose rate was refuted by these results.

Table 4.1 is a summary of the results in terms of enhancement factors, it is shown also the worst case scenario taking into account the upper bound enhancement factors. Even

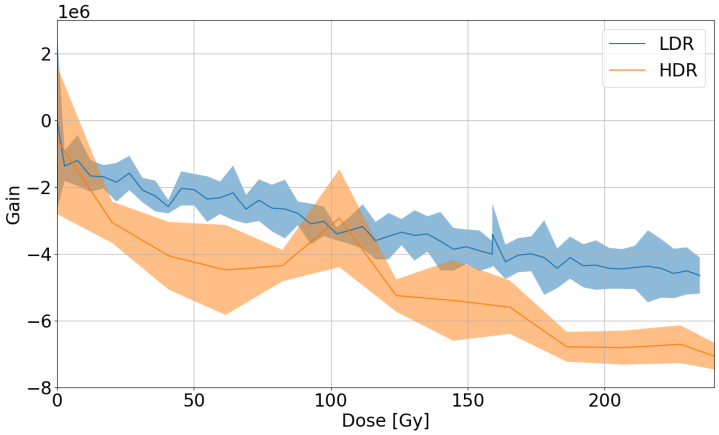

Figure 4.3: Comparison between the open loop gain degradation of the operational amplifier OP07 at high dose rate (HDR) and low dose rate (LDR).

considering those values the degradation of the parameters is negligible for the purpose of the amplifier.

Parameter	EF	$\lvert EF\rvert_{95\%}$	Degradation at 500Gy
Input bias current	1.1 ± 0.6	< 2.4	$\lvert\Delta I_{bias}(500Gy)\rvert < 48\ nA$
Input offset voltage	-1.9 ± 1.4	< 5	$\lvert\Delta V_{offset}(500Gy)\rvert < 75\ \mu V$
Open loop gain	0.7 ± 0.1	< 1	$G > 100\ dB$

Table 4.1: Summary of the ELDRS test of the OP07 on the three parameters.

4.3 Operational Amplifiers

4.3.1 Input Bias Current

The input bias current of the three bipolar operational amplifiers (AD829, LM358AD and LT1013) exhibits a gradual increase in absolute value. On the contrary, the BiCMOS device MAX4238 does not degrade during irradiation, its bias current remains in the order of few pico-Ampere. This difference is due to the technology: the input bias current in the BiCMOS devices is constituted by the gate currents of the input stage MOSFETs.
The AD829 exhibits a sublinear increase of the bias current that can be related to the effect of the ionizing dose alone, in Figure 4.4 can be noticed that the degradation profiles in all the CHARM test positions (R1, R8 and R11) are superimposed to the result obtained at CC60 (gamma irradiation).

The increase of the bias current of the LM358AD as a function of the cumulated dose in the different test positions is depicted in Figure 4.5, it is representative also of the LT1013 degradation that follows a very similar profile. Also the LM358AD and the LT1013 show a sublinear increase of the bias current, but in these cases it depends also on the displacement damage: the higher the displacement damage, the higher the degradation. As a consequence, the profiles that corresponds to the tests at CHARM represent higher input bias current as a function of the cumulated dose in ascending order from the lowest DDEF/TID value to the highest DDEF/TID value. For example, in position R1 the devices are subjected to higher displacement damage with respect to the other test positions, for this reason the degradation is higher. In position R1, in which the DDEF/TID is higher,

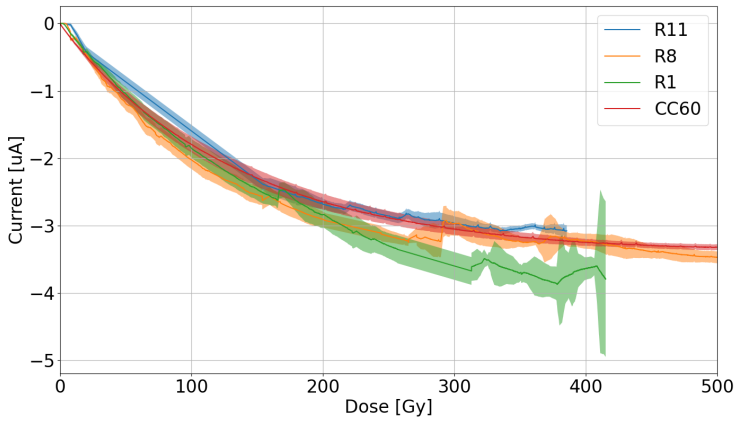

Figure 4.4: Input bias current degradation of the operational amplifier AD829 at different ratios DDEF/TID. The degradation can be attributed to the ionizing dose.

the entity of the displacement damage contributions is slightly higher than 50%, in the other locations the contributions are lower than 50%.

Figure 4.6 shows the displacement damage contributions extracted by subtracting the

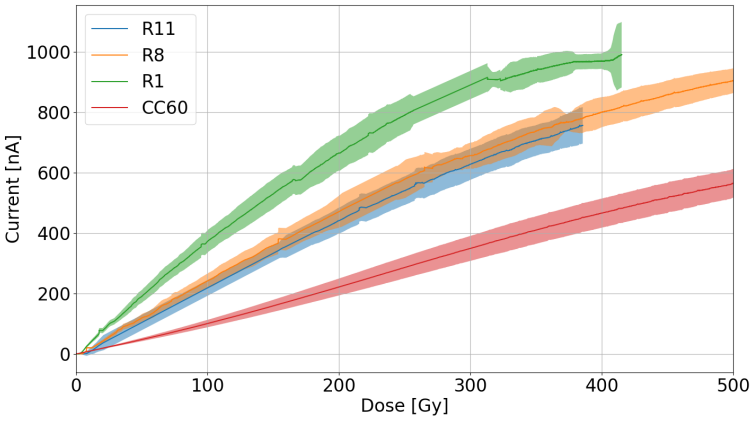

Figure 4.5: Input bias current degradation of the operational amplifier LM358AD at different ratios DDEF/TID.

TID component (Equation 4.18), these profiles are superimposed in the first part of the degradation and tend to differ as the TID increases. It is interesting to notice that the DD contributions seem to exhibit a saturation phenomenon, the saturation is reached earlier at low DDEF/TID values (the slope of the R11 profile is the highest) and later at higher DDEF/TID values (the slope of the R1 profile is the lowest). As explained in section 2.3, the increase of the bias current is likely due to the increase of the base current of the input stage transistors. While the increase due to TID will saturates, the displacement damage contribution is not expected to reach saturation. There can be two possible explanations: synergy between TID and DD that causes a reduction of the influence of the displacement damage as the dose increases, or a circuit level moderation of the increase that could be due to the bias circuit of the input differential pair. If the bias circuit degrades, the current flowing into the drains of the differential pair decreases and, consequently, also the base current decreases. It is an opposing effect respect to the input transistor degradation.

On the contrary, the overall degradation of the LT1013 exhibits a saturation phenomenon that is independent on the DDEF/TID ratio, the final current value is equal to the one

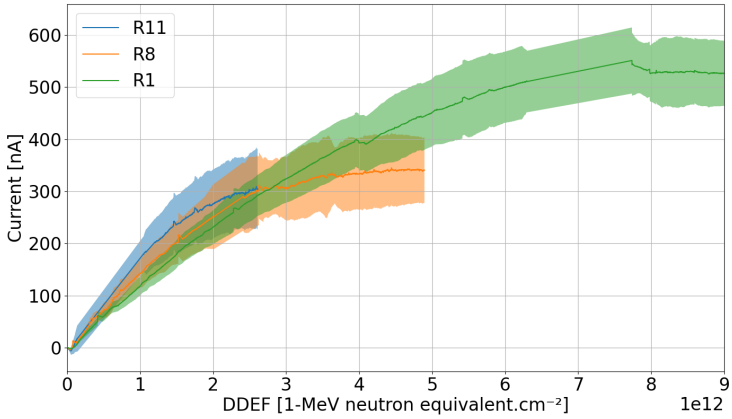

Figure 4.6: Displacement damage contributions to the input bias current degradation of the operational amplifier LM358AD at different ratios DDEF/TID.

obtained during gamma irradiation. For this reason, the DD contributions to the damage are superimposed in the first part and go to zero when the saturation occurs.
Since the profiles of the DD contributions are superimposed independently on the DDEF/TID ratio, the p-values associated to the ANOVA test (Equation 4.26) for the LM358AD and to the t-test (Equation 4.22) for the LT1013 are higher than 5%, the null hypothesis cannot be rejected, the degradation depends on both TID and DD, but their contributions are additive.

4.3.2 Input Offset Voltage

The input offset voltages of the AD829 and the LM358AD gradually degrade and they exhibit synergistic effects of TID and DD in a very similar way. In both cases the degradation is due to the combined effects of ionizing and non-ionizing dose, the damage in mixed-field environments is higher than that observed during gamma irradiation. An example of these profiles is depicted in Figure 4.7 that represents the behaviour of the LM358AD in different test conditions.

The result of the separation of the displacement damage contributions from the overall

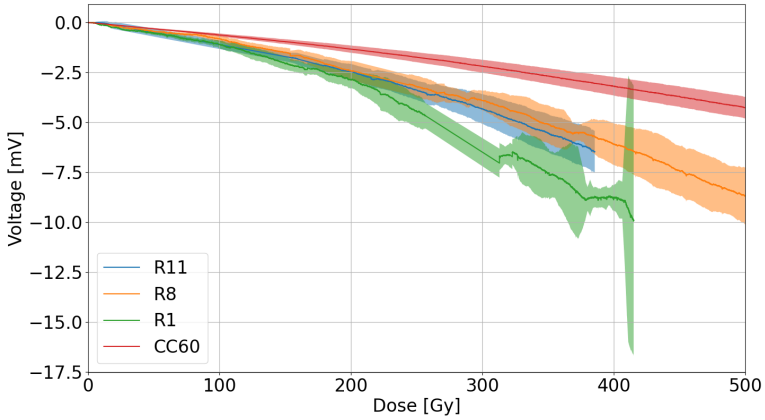

Figure 4.7: Input offset voltage degradation of the operational amplifier LM358AD at different ratios DDEF/TID.

damage is reported in Figure 4.8 concerning the LM358AD, The DD contributions range

from roughly 50% (in R8 and R11) to around 70% (in R1). For the AD829, the displacement damage contributes for less than 50% of the overall damage in all the test positions. The higher is the DDEF/TID ratio, the lower is the degradation, the difference between the three profiles is the cumulated ionizing dose associated to the DDEF, in other words, the devices tested in R11 that reached $2 \cdot 10^{12}$ $1MeVn - eq/cm^2$ accumulated more than three times the ionizing dose with respect to the devices tested in R1 that reached the same DDEF. Since the total ionizing dose contribution to the damage is already removed from these profiles, it means that the overall degradation cannot be separated into two additive TID and DD contributions. The ionizing dose causes the enhancement of the displacement damage effects on the tested parameter.

This conclusion is supported by the result of the ANOVA test performed on the DD

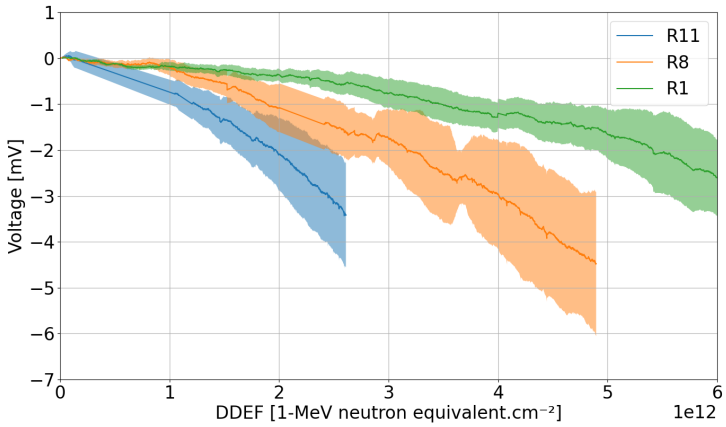

Figure 4.8: Displacement damage contributions to the input offset voltage degradation of the operational amplifier LM358AD at different ratios DDEF/TID.

contributions profiles. Figure 4.9 shows the p-value associated to the ANOVA test concerning the LM358AD input offset voltage. At the end of the profile the value becomes lower than 5%, meaning that the probability that the three DD contributions have the same mean is lower than 5%. The same result is obtained for the input offset voltage of the AD829.

On the other hand, the operational amplifier LT1013 shows a slight degradation of the

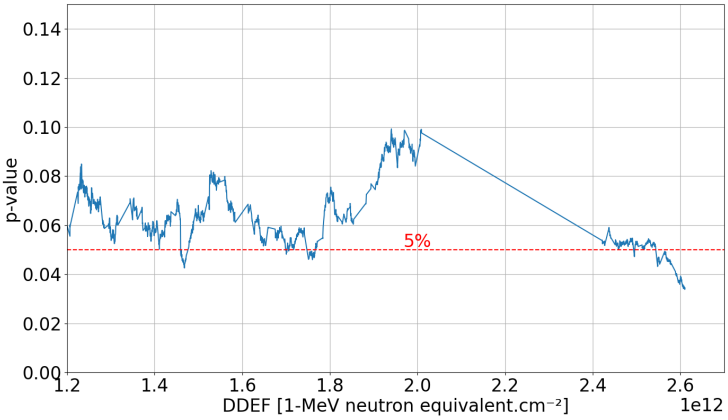

Figure 4.9: Profile of the p-value associated to the ANOVA test as a function of the displacement damage equivalent fluence concerning the input voltage degradation of the operational amplifier LM358AD.

offset voltage until the complete failure of the device. The degradation is more evident

in environments full of neutrons (R1 and R8) with respect to the gamma irradiation similarly to the case shown in Figure 4.5. The displacement damage accounts for the 86% in R1 and 75% in R8 considering the damage as a function of the cumulated dose. In this case, the contributions of the displacement damage as a function of the DDEF are equal in both mixed-field environments regardless the DDEF/TID ratio as can be seen in Figure 4.10, there are no synergistic effects and the damage can be separated into two additive contributions of ionizing and non-ionizing dose.

Finally, the MAX4238 don't exhibit any degradation of the input offset voltage up to

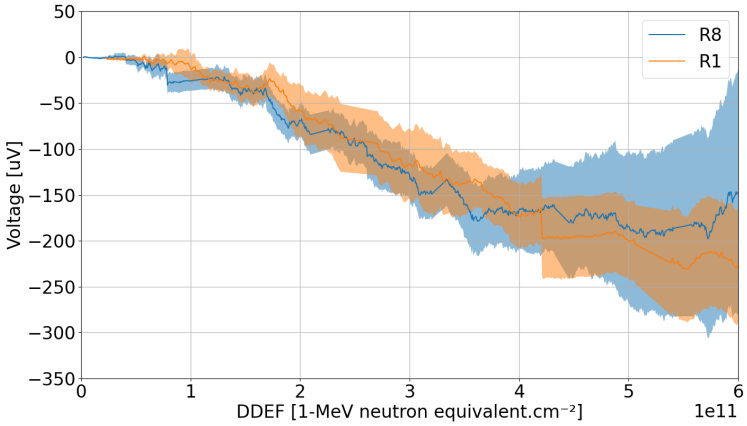

Figure 4.10: Displacement damage contributions to the degradation of the input offset voltage of the operational amplifier LT1013.

the complete failure of the device.

4.3.3 Open Loop Gain

The open loop gain of the AD829 is depicted in Figure 4.11 as a function of the cumulated dose at different levels of DDEF/TID ratio. The degradation in presence of displacement damage is higher with respect to the ionizing dose alone and it is consistent with the typical gain degradation of the operational amplifier that is due to the degradation of the current gain of the internal transistors caused by TID and DD.

The displacement damage contributions are illustrated in Figure 4.12, they are all super-

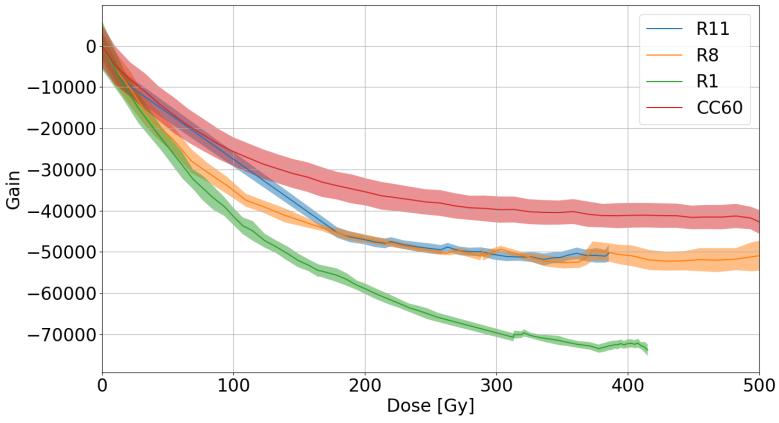

Figure 4.11: Open loop gain degradation profiles of the operational amplifier AD829 at different DDEF/TID ratios.

imposed at the beginning of the profiles, the responses in R8 and R11 remains equal until

the end of the irradiation, while the R1 response differs. In this case, in contrast to the behavior observed regarding the offset voltage, the profile corresponding to the highest cumulated ionizing dose is the less degraded, this behaviour suggest that the TID causes the moderation of the effects of the displacement damage on the open loop gain.

This conclusion is supported by the t-test performed on the R8 and R1 profiles, the

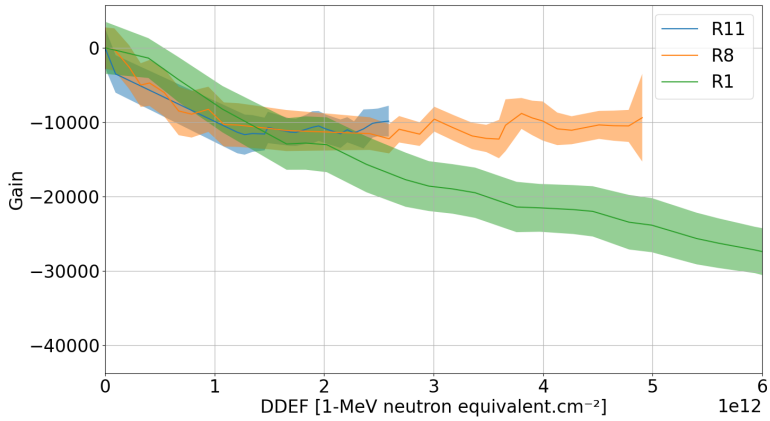

Figure 4.12: Displacement damage contributions to the degradation of the open loop gain of the operational amplifier AD829.

obtained p-value is lower than 5% indicating a low probability of belonging to the same population.

However, since the open loop gain degradation is likely caused by the reduction of the internal BJT current gain decrease and since this decrease can be explained with Equations 1.6 and 1.7, there is another way of extrapolating the displacement damage contributions.

$$\frac{1}{Gain_{DD}} = \frac{1}{Gain_{TID|DD}} - \frac{1}{Gain_{TID}} \tag{4.33}$$

The resulting profiles are shown in Figure 4.13 for the AD829. The slope of the DD

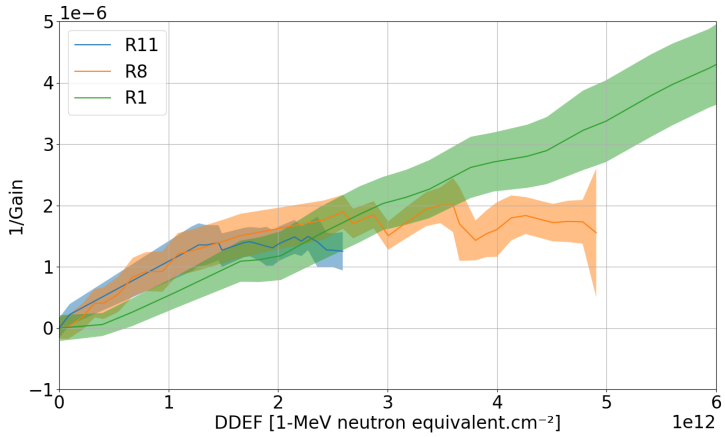

Figure 4.13: Displacement damage contributions to the degradation of the open loop gain of the operational amplifier AD829 calculated as in Equation 4.33.

contribution increase is almost equal regardless the DDEF/TID ratio, the R8 and R11 profiles reach a saturation value probably due to the saturation of the ionizing dose effects on the base current increase of the internal transistors. The R1 profile does not exhibit

the saturation because at same DDEF it is subjected to lower TID values. Considering this different way of extrapolating the displacement damage contributions, the t-test performed on the R8 and R1 profiles results in a p-value higher than 5%: it is not possible to confirm the presence of synergistic effects.
The degradation of the LM358AD is very similar to the AD829 one, in that case the displacement damage contributions are superimposed during the entire irradiation.
The behaviour of the open loop gain of the LT1013 is depicted in Figure 4.14, even if the mean values of the measurements in combined TID-DD environments suggest an higher degradation respect to the TID-only profile, the variance of the measurements does not allow the separation of the contributions, the degradation can be completely explained with the effects of the ionizing dose alone.

However, the LT1013 exhibited an abrupt change of the output voltage to the positive

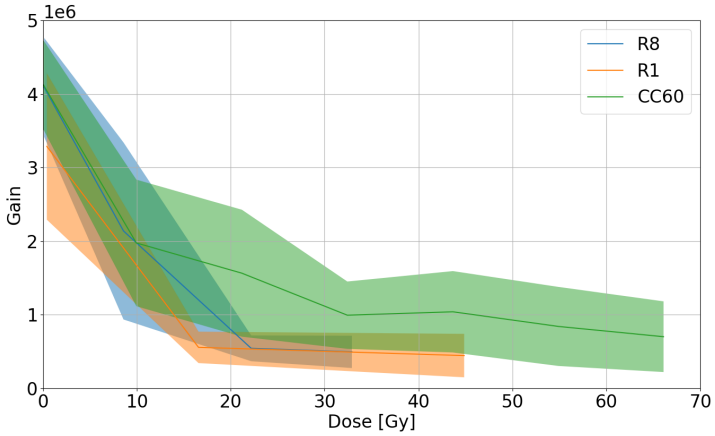

Figure 4.14: Degradation of the open loop gain of the operational amplifier LT1013 up to the complete failure of the device.

supply. Figure 4.15 shows the output voltage of the open loop gain test circuit, the relation between the output voltage of the test circuit and the output voltage of the device under test is explained in section 3.1.3. If the output voltage of the DUT increases until reaching the supply voltage regardless the input voltage, the output voltage of the auxiliary amplifier becomes lower and lower to compensate trying to compensate the increase by imposing a negative voltage at the input of the DUT, since the DUT does not respond to the input, the output voltage of the auxiliary amplifier reaches the negative supply voltage, as visible in Figure 4.15. If the output voltage of the DUT increases until it matches the supply voltage, the output voltage of the auxiliary amplifier gradually decreases. This decrease occurs as the amplifier attempts to compensate the rising output voltage of the DUT by applying a negative voltage at the DUT's input. However, since the DUT is unresponsive to the input, the output voltage of the auxiliary amplifier continues to drop until it reaches the negative supply voltage, as shown in the Figure.

It is possible to evaluate the presence of synergistic effects by checking whether the output voltage overcomes a threshold that determines the failure of the device, as explained in the section 4.1.3. Assuming that the failure is due to an internal parameter, the inverse of the mean doses at which the devices fail can be fitted with a linear function (Equation 4.27). The resulting plot is depicted in Figure 4.16. The p-value associated to the reduced χ^2 test (Equation 4.28) performed on the linear regression is equal to 11%. The fit is very poor, there are few data and a sublinear equation could fit better the data, it would mean again that low DDEF/TID ratios result in higher degradation with respect to the high DDEF/TID ones. But the null hypothesis cannot be rejected: there are no synergistic

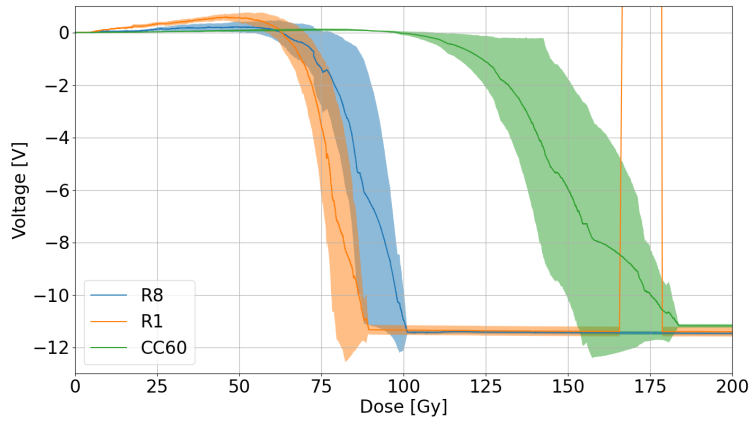

Figure 4.15: Output voltage degradation profiles of the operational amplifier LT1013 at different DDEF/TID ratios.

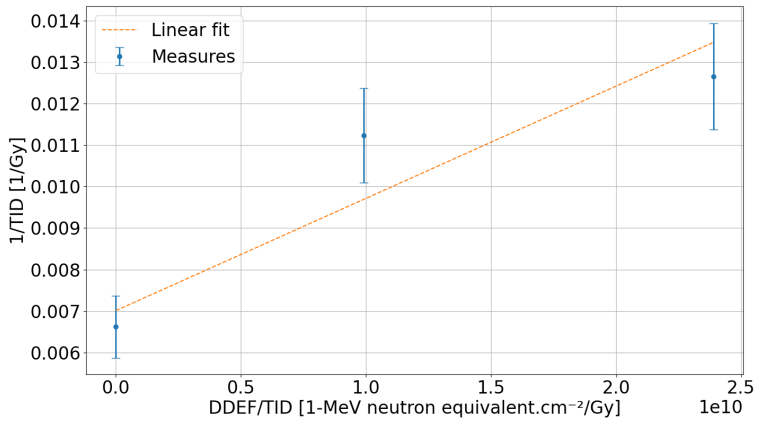

Figure 4.16: Inverse of the breakdown dose associated to the output voltage abrupt degradation of the operational amplifier LT1013 as a function of the ratio DDEF/TID.

effects.
Since all the graphical representations of this type of analysis are very similar and all of them consists into data points as a function of the DDEF/TID ratio, this picture can be representative of all the following analysis.

4.4 Instrumentation Amplifiers

Before going into the details of the failure profiles of the different instrumentation amplifiers, it is important to mention the results of the INA326 that was tested at CHARM and at PSI in previous campaigns and showed a strange behaviour reported in Figure 2.10. During the current study, it was exposed to mixed-field and gamma irradiation. At Cobalt 60 it stops working completely between 500 Gy and 600 Gy as visible in Figure 4.17. In the other test positions, the device exhibits high sensitivity to single event effects, in particular single event transients and latchups. Figure 4.18 shows the evolution of the output voltage during the irradiation in position R8 at CHARM. The presence of high energy hadrons induces the sudden increase of the voltage up to the supply voltage (2.5 V). These phenomena occurs also in the bias current and offset voltage test circuits. For this reason it is impossible to evaluate the degradation profiles of the device in different radiation environments. This device cannot be used at all in the LHC. Noticeably, the

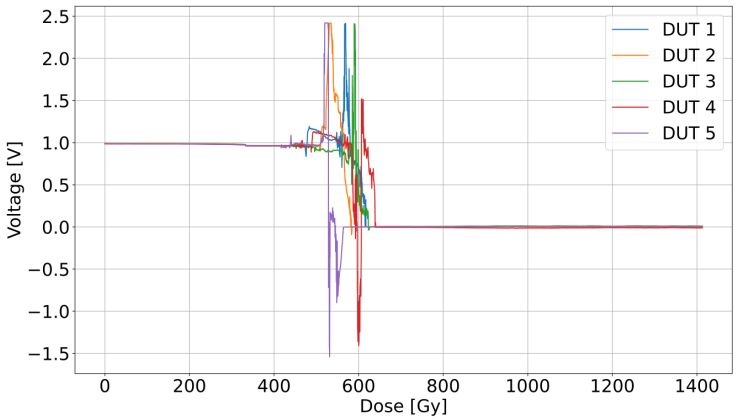

Figure 4.17: Output voltage degradation of the instrumentation amplifier INA326 exposed to gamma irradiation.

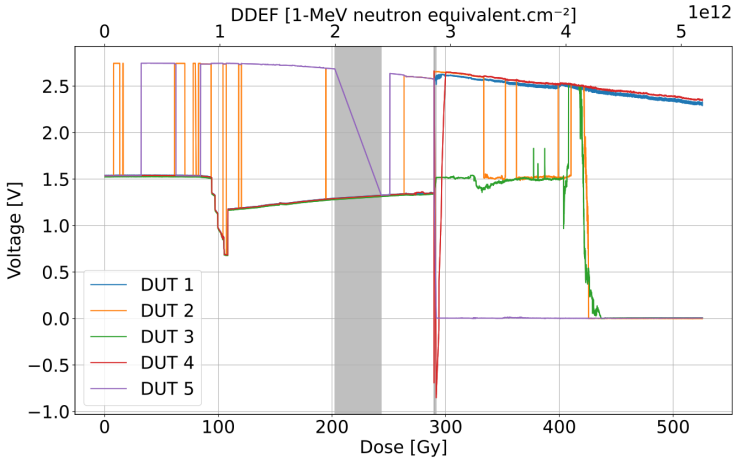

Figure 4.18: Output voltage degradation of the instrumentation amplifier INA326 exposed to mixed-field irradiation in position R8 at CHARM.

gradual voltage decrease in Figure 4.18 is due to the decrease of the supply voltage caused by the increase of the supply current and the resistance of the cable chain ($\sim 10\ \Omega$).

4.4.1 Input Bias Current

As in the case of the operational amplifiers, the input bias current degradation of the instrumentation amplifiers depends on the technology: the two bipolar devices AD621 and AD8420 show a gradual degradation, while the BiCMOS device MAX4208 exhibits very low degradation in the order of tens of pico-Amperes.
The input bias current of the AD621 shows an initial gradual degradation followed by the increase of the degradation rate. As visible in Figure 4.19 the degradation is due to the combined effect of ionizing and non-ionizing dose and the higher is the ratio DDEF/TID, the earlier is the failure. The abrupt increase of the bias current can be analyzed as previously done in the case of the LT1013 output voltage, for each test position the average dose at which the bias current overcomes a threshold is calculated, the inverse of these dose values can be related to the DDEF/TID ratio. The p-value associated to the reduced χ^2 test is equal to 8%, the fit is not good, also in this case a sublinear relation seems to be more appropriate, but the p-value is not low enough to reject the null hypothesis: there are no synergistic effects.
Focusing on the first part of the degradation, the displacement damage accounts for

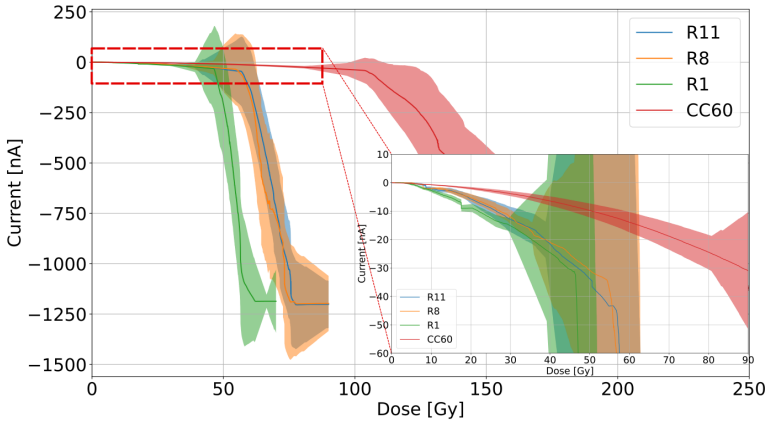

Figure 4.19: Input bias current degradation profiles of the instrumentation amplifier AD621 at different DDEF/TID ratios.

approximately the 70% of the current increase in all the tested positions considering the profiles as a function of the cumulated dose. The DD contributions extracted from those profiles are depicted in Figure 4.20 as a function of the displacement damage equivalent fluence. Since the curve associated to the lowest DDEF/TID ratio (R11) is the most degraded, the image suggests the presence of synergistic effects equivalent to the ones encountered in the evaluation of the LM358AD and AD829 offset voltage: the ionizing dose causes the enhancement of the effect of the displacement damage. However, the

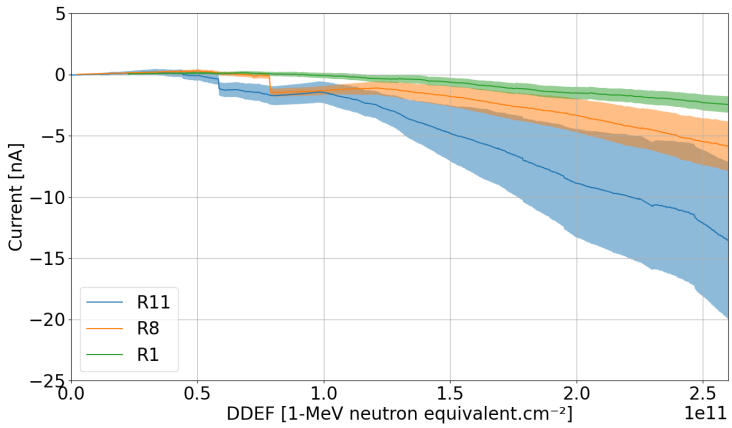

Figure 4.20: Displacement damage contributions to the degradation of the initial part of the input bias current of the instrumentation amplifier AD621.

p-value associated to the ANOVA test is higher than 5% in all the profile, the three contributions are not enough separated to have a strong evidence on the presence of synergistic effects.

The AD8420, in contrast with all the other tested devices, exhibits a bias current increase caused exclusively by the displacement damage, the degradation observed during gamma irradiation is approximately two order of magnitude lower than the degradation observed in mixed-field environments. Figure 4.21 shows the displacement damage contributions to the degradation of the bias current, as already seen in previous cases, this distribution of profiles is a symptom of the enhancement caused by TID of the DD effects. The p-value associated to the ANOVA test is lower than 5% and confirms this conclusion.

The BiCMOS amplifier MAX4208 exhibits a very low input bias current in the order of pA

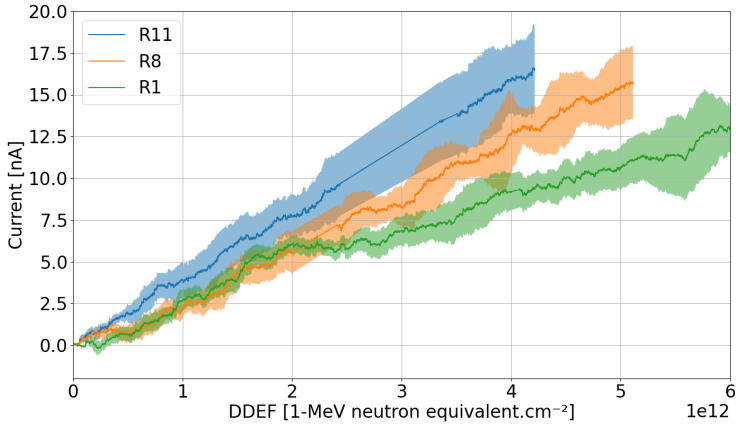

Figure 4.21: Displacement damage contributions to the degradation of the input bias current of the instrumentation amplifier AD8420.

because of a CMOS input stage and a consequently low bias current degradation, as visible in Figure 4.22. The increase of the bias current in different radiation conditions suggests the same type of synergistic effect encountered previously: the ionizing dose enhances the effects of the displacement damage. Without removing the TID contribution, the higher degradation of the bias current at lower DDEF/TID ratios is a strong evidence of synergistic effects. In fact, it is expected to degrade more the devices placed in positions with higher DDEF/TID because at same cumulated dose they are subjected to more displacement damage. If they degrade less, it means that there are interactions between the ionizing and non-ionizing dose. In this case, instead of extrapolating the displacement

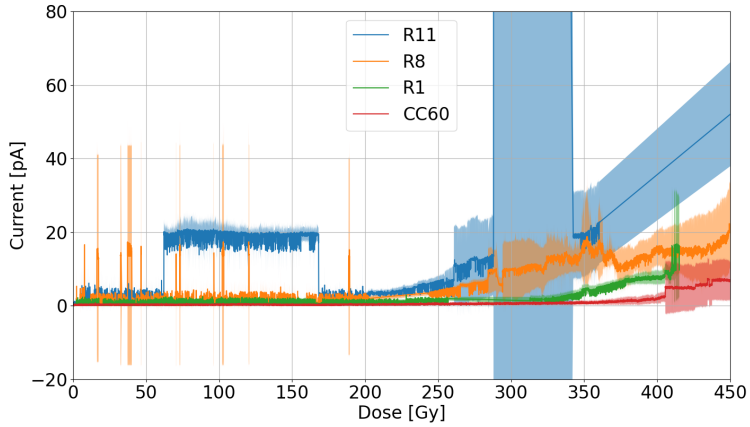

Figure 4.22: Input bias current degradation profiles of the instrumentation amplifier MAX4208 at different DDEF/TID ratios.

damage contribution to the degradation, it is better to consider the mean doses at which a bias current threshold is overcome and fit the inverse of these resulting doses with a linear function of the DDEF/TID ratio. The p-value associated to the reduced χ^2 test is 0.2%, the data cannot be fitted by a straight line, the presence of synergistic effects are confirmed.

4.4.2 Input Offset Voltage

The input offset voltage degradation profiles are very different between the instrumentation amplifiers: the offset voltage of the AD621 does not degrade up to the complete failure of the device, the one of the AD8420 increases with the dose, but it is mainly caused by the displacement damage (as in the case of the input bias current, its TID contribution to the damage is negligible) and the MAX4208 exhibits a step increase of the offset voltage.
The DD contributions extracted from the offset voltage degradation of the AD8420 are depicted in Figure 4.23. Because of the high variability between devices, the profiles are superimposed, consequently, there are no synergies between TID and DD in the offset voltage increase.

Figure 4.24 shows the evolution of the input offset voltage of the MAX4208, it exhibits

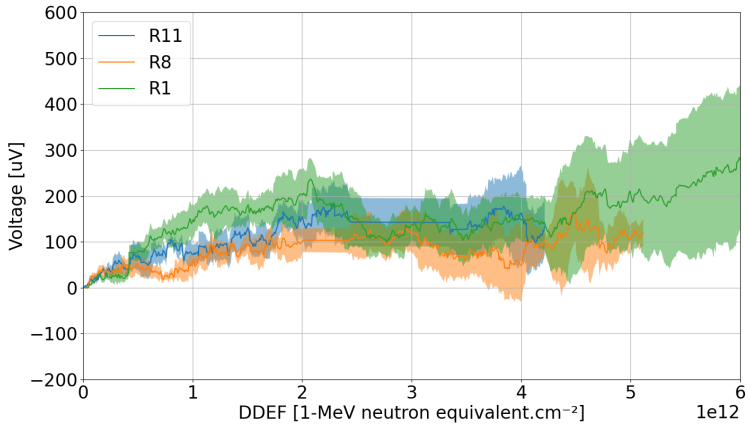

Figure 4.23: Displacement damage contributions to the degradation of the input offset voltage of the instrumentation amplifier AD8420.

a step increase between 250 Gy and 400 Gy. The p-value associated to the ANOVA test, performed by considering for each test position the mean dose at which the step happens, is 7%: there is the 7% of probability that all the steps doses belong to the same population. The degradation can be considered as driven by the ionizing dose.

Noticeably, the difference in the degradation profiles could be related to the different

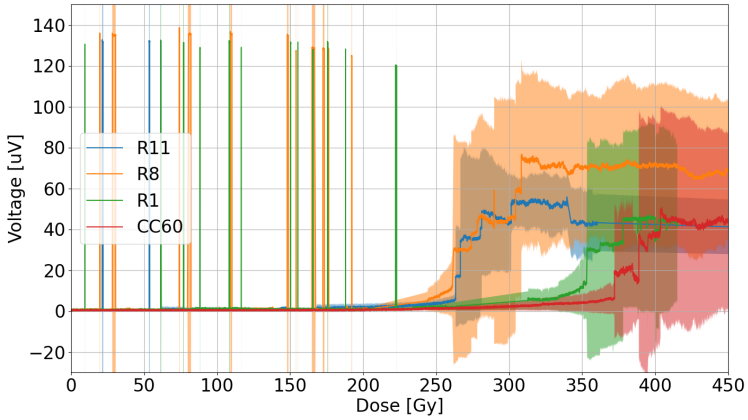

Figure 4.24: Input offset voltage degradation profiles of the instrumentation amplifier MAX4208 at different DDEF/TID ratios.

technology: while the bipolar amplifiers exhibit gradual degradation, the BiCMOS one

shows a step increase of the tested parameter. Moreover, the voltage spikes that precede the step are likely due to the temporary activation of the internal CMOS circuitry caused by striking particles (Single Event Transients). Could be interesting further investigate these differences in future works, it cannot be done in this thesis due to the scarcity of chosen BiCMOS ICs.

4.4.3 Output Voltage

The tested instrumentation amplifiers don't exhibit output voltage degradation during the entire irradiation, except the AD621. This device shows a sudden drop of the output voltage that leads to the complete failure. The drop is likely due to the decrease of the gain of the BJTs that compose the device, while the preceding peaks could be related to the increase of the resistivity of the semiconductor that could lead to higher output resistance and consequently to higher gain as explained in [38].

As an example, Figure 4.25 shows the behaviour of the five AD621 tested at CHARM

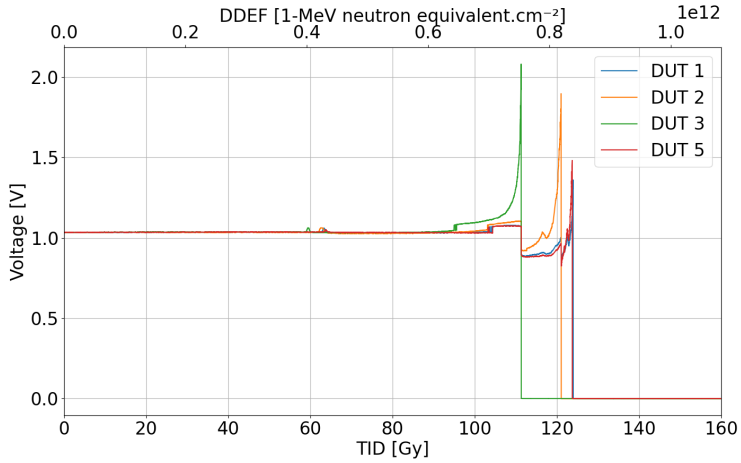

Figure 4.25: Output voltage degradation profiles of the instrumentation amplifier AD621 at CHARM in position R11.

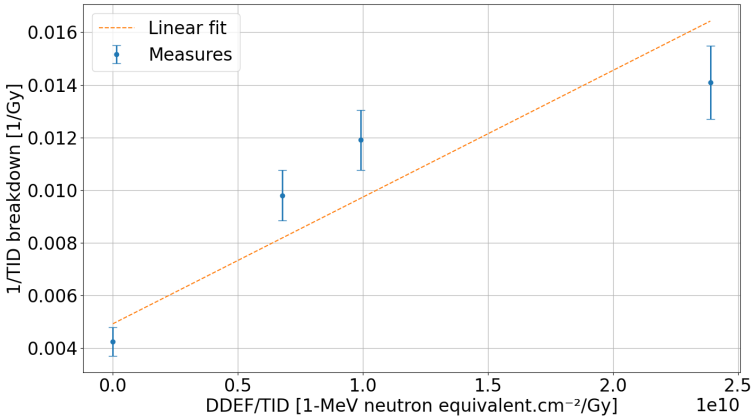

Figure 4.26: Inverse of the output voltage breakdown doses of the instrumentation amplifier AD621 as a function of the ratio DDEF/TID

in position R11. After an initial increase of the output voltage, it drops suddenly to zero volt causing also the increase of the input current. The mean doses associated to the sudden failure of the devices in each test position as a function of the DDEF/TID ratio

are reported in Figure 4.26. The reduced χ^2 test of goodness of fit results in a p-value equal to 6%, it is a very low result, but not enough to reject the null hypothesis. Even if the sublinear distribution of the data suggests an enhancement of the DD contribution due to TID, it is not possible to confirm this conclusion.

4.5 Voltage Regulators

4.5.1 Output Voltage

The degradation of the output voltage of the voltage regulators can be classified into two categories: gradual degradation and sudden drop. The tested devices exhibit both behaviours.
The voltage regulator MIC29302 exhibits negligible output voltage degradation until the complete failure of the device. Figure 4.27 shows the evolution of the output voltage of one device for each test position, noticeably, in all the positions the devices show abrupt degradation of the output voltage with a clear dependency on both the displacement damage and the ionizing dose: the higher the displacement damage, the earlier the drop happens. This behaviour is due to the increase of the start-up voltage that will be discussed in the next paragraph, when it overcomes the maximum input voltage, the device stops to regulate and the output voltage drops to zero. In addition, the displacement damage is the only responsible for the increase of the output voltage up to the supply shortly before the failure. A possible motivation is given in [42]: the increase of the leakage current of one of the transistors composing the internal voltage reference circuit leads to the increase of the output voltage. To confirm the hypothesis a simulation is required, but it is likely that this leakage current is caused mainly by displacement damage, as reported in [25].
As already done for the output voltage of the AD621, the inverse of the mean doses at

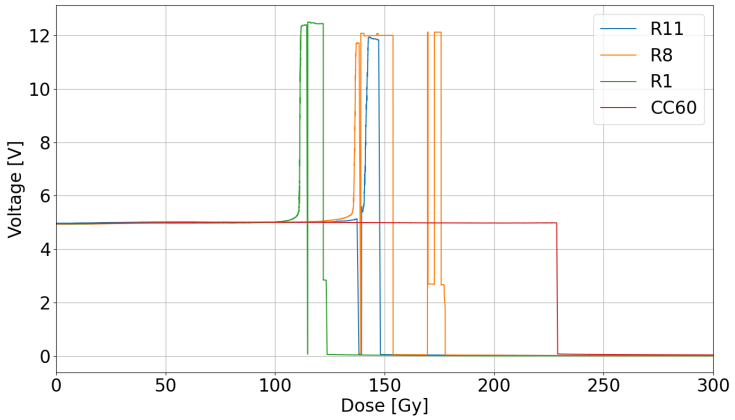

Figure 4.27: Example of output voltage degradation profiles of the voltage regulator MIC29302 at different DDEF/TID ratios.

which the sudden drop happens is fitted with a linear function of the ratio DDEF/TID. The p-value associated to the reduced χ^2 test is equal to 15%, the null hypothesis cannot be rejected, the earlier drop of the output voltage can be explained with a linear combination of DD and TID contributions (Equation 4.27).
The LM2936 exhibit an initial gradual degradation and a sudden drop after a certain value of cumulated dose, in the initial part, the displacement damage accounts for less than 40% of the overall degradation. The displacement damage contributions to the output voltage

degradation of the initial part of the profiles as a function of the DDEF are shown in Figure 4.28. The devices degradation in position R8 with a lower DDEF/TID ratio is higher with respect to the one in position R1, this behaviour suggests that the ionizing dose enhances the displacement damage contribution. However, the p-value associated to

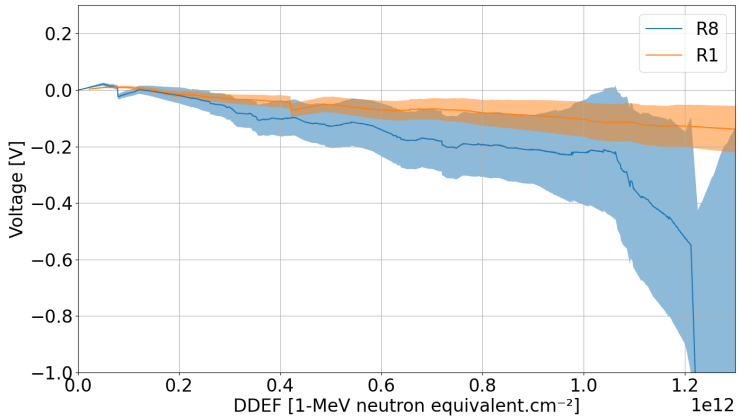

Figure 4.28: Displacement damage contributions to the degradation of the output voltage in the first part of the profile of the voltage regulator LM2936.

the Welch's t-test performed on these two profiles is higher than 5%, as visible in Figure 4.29, there is an high probability that these two responses belong to the same population and have the same mean value.

The sudden drop can be analyzed as already done with the MIC29302, for each test

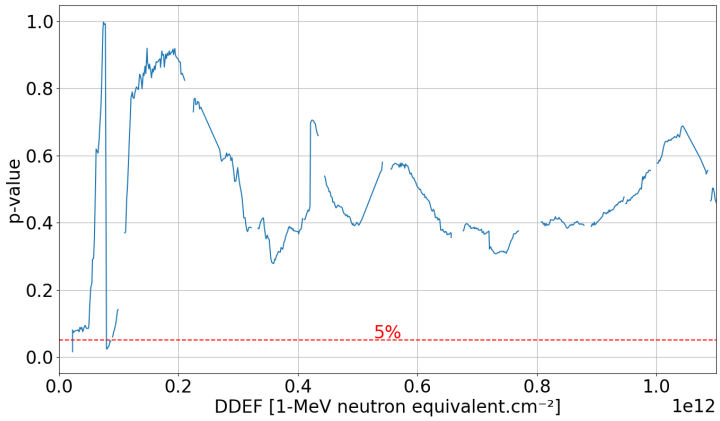

Figure 4.29: Profile of the p-value associated to the Welch's t-test as a function of the displacement damage equivalent fluence of the voltage regulator LM2936.

position, the inverse of the mean dose at which the output voltage overcomes a threshold can be fitted with a linear function to check whether the synergistic effects are present or not. In the case of the LM2936, the p-value associated to the reduced χ^2 test is equal to 41%: the data can be fitted with a linear function and there are no synergistic effects.
Also the LT1085, whose response is depicted in Figure 4.30, exhibits an initial gradual degradation and a sudden drop of the output voltage, except for the CC60 profile, that continues to degrade gradually until the end of the irradiation (1.4 kGy). The underlying phenomena to this behaviour are the same mentioned for the MIC29302. Although the sudden increase and drop of the output voltage appears only during mixed-field irradiation and, thus, it is strongly related to the presence of neutrons in the environment, it

is due to the combined effects of TID and DD. In fact, even considering the profiles as a function of the displacement damage equivalent fluence the sudden drops don't coincide. As for the MIC29302, the output voltage drop corresponds moment in which the start-up voltage overcomes the maximum input voltage. In the following paragraph will be shown that this increase occurs only in mixed-field radiation environments. By fitting the in-

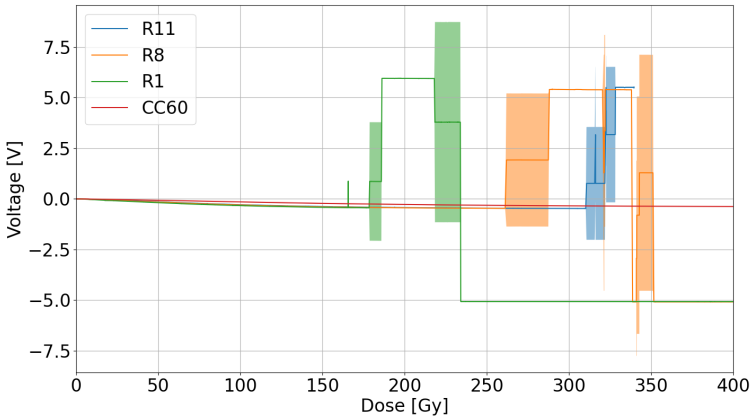

Figure 4.30: Output voltage degradation of the voltage regulator LT1085 at different DDEF/TID ratios.

verse of the doses at which the sudden drop happens with a linear function of the ratio DDEF/TID, the p-value resulting from the reduced χ^2 test is equal to 95%. The data are well fitted by the linear function and there are no synergistic effects.
Concerning the initial part of the profiles, the degradation is due to the combined effects of TID and DD: the devices exposed to the mixed-field environment exhibit stronger degradation. The displacement damage contributions to the degradation initially suggest an enhancement of the DD effects due to TID: the degradation is faster at low DDEF/TID ratios, considering intermediate DDEF, the degradation is higher at low DDEF/TID. However, all the profiles reach a saturation value at approximately $1.5 \cdot 10^{12}$ $1 - MeVneq/cm^2$ independent on the DDEF/TID and it is equal to the 35% of the overall degradation. The DD contributions are shown in Figure 4.31.

The LT1763 exhibits a positive degradation in all the test positions, the main contri-

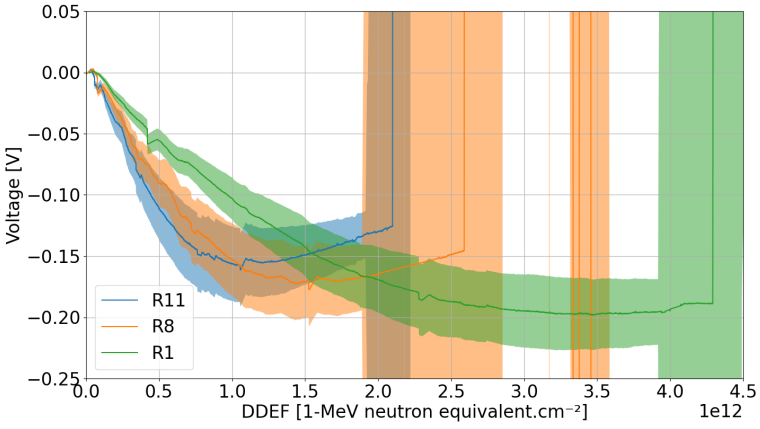

Figure 4.31: Displacement damage contributions to the degradation in the first part of the profile of the voltage regulator LT1085.

bution to the damage is the ionizing dose: from 90% in R11 to 70% in R1. The output

voltage reaches a saturation value after approximately 300 Gy independently on the test position, the saturation value of the voltage increase goes from +0.5 V at CC60 to +0.6 V in R1. The contributions due to the displacement damage shown in Figure 4.32 suggest the presence of synergistic effects of the opposite nature of the ones encountered previously: the DD contributions measured in environments in which the ionizing dose is more dominant (lower DDEF/TID ratio) exhibit less degradation at same DDEF with respect to the ones measured at higher DDEF/TID ratios. The ionizing dose moderates the effects of the displacement damage. However, the profiles depicted in Figure 4.32 are not enough separated to confirm the presence of these synergy between TID and DD. The p-value associated to the ANOVA test performed on the DD contributions is higher than 5%.

The degradation of the voltage regulator MAX8881 is gradual and positive in all the

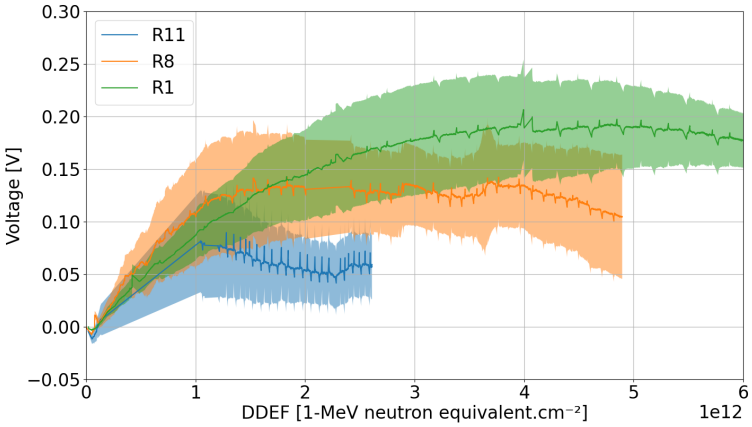

Figure 4.32: Displacement damage contributions to the degradation of the voltage regulator LT1763.

tested positions, differently from the previous case, the output voltage increase does not reach a saturation value. The contribution of the ionizing dose on the overall degradation goes from the 40% in R11 to the 25% in R8. The degradation in R1 is unexpectedly lower than that in R8, even if at same cumulated dose the first is exposed to higher levels of displacement damage equivalent fluence. The DD contributions to the damage are shown in Figure 4.33

This is a particular example of synergy between ionizing and non-ionizing dose: remem-

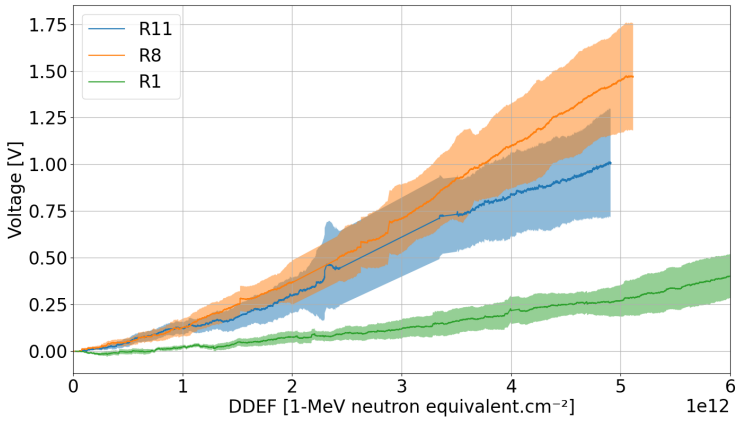

Figure 4.33: Displacement damage contributions to the degradation of the voltage regulator MAX8881.

bering that R1, R8 and R11 are in descending order of DDEF/TID ratio, it can be noted that the R8 profile is the most degraded one. Even though R8 and R11 are very close to each other, the profiles suggest a non-linearity of the ionizing dose enhancement of the displacement damage. The enhancement is clear from R1 and R8, as the ionizing dose increase, the displacement damage contribution increases. But from R8 to R11 the increase of the cumulated ionizing dose results in a slight reduction of the displacement damage contribution.
Although the contributions corresponding to the positions R8 and R11 are partially superimposed in Figure 4.33 (the p-value associated to the t-test is approximately 30%), their large difference with the R1 contribution makes evident the presence of synergistic effects. The p-value associated to the ANOVA test is well below 5%.
The last voltage regulator is the TPS73033, the output voltage degradation of this device

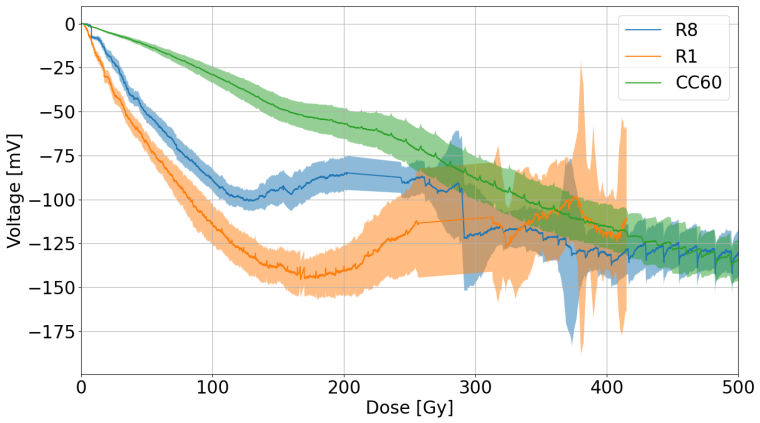

Figure 4.34: Output voltage degradation profiles of the voltage regulator TPS73033 at different DDEF/TID ratios.

depends initially on the combined effects of ionizing and non-ionizing dose, after 350 Gy it reaches a saturation value of approximately -125 mV regardless of the test location as visible in Figure 4.34. The overall degradation can be completely predicted by the gamma irradiation.
In addition, considering the initial part in which also the displacement damage plays a

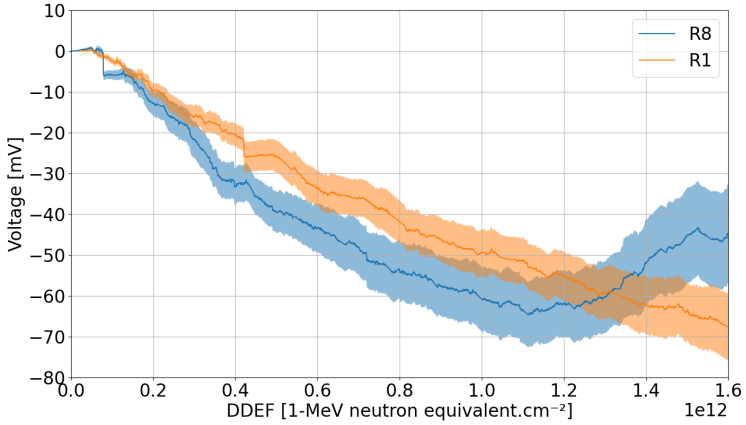

Figure 4.35: Displacement damage contributions to the degradation of the voltage regulator TPS73033

role in the degradation, the contributions extracted for each CHARM test position and depicted in Figure 4.35 suggest the presence of a positive influence of the ionizing dose on

the displacement damage contributions. However, the profiles are not enough separated to confirm this hypothesis, the p-value associated to the Welch's t-test is higher than 5%.

4.5.2 Start-up voltage

The start-up voltage is defined as the input voltage at which the device starts to regulate the output, in order to obtain a numerical value it is necessary to select a threshold voltage above which the device is considered operational. I chose a threshold voltage equal to the 95% of the final output voltage. All the tested regulators exhibit a rapid increase of the start-up voltage, for this reason the evaluation of the presence of synergistic effects is performed by fixing a threshold in the start-up voltage and analyzing the relation between the doses at which the start-up voltage overcomes this threshold and the ratio DDE-F/TID. Figure 4.36 shows a typical input characteristic of the voltage regulators under

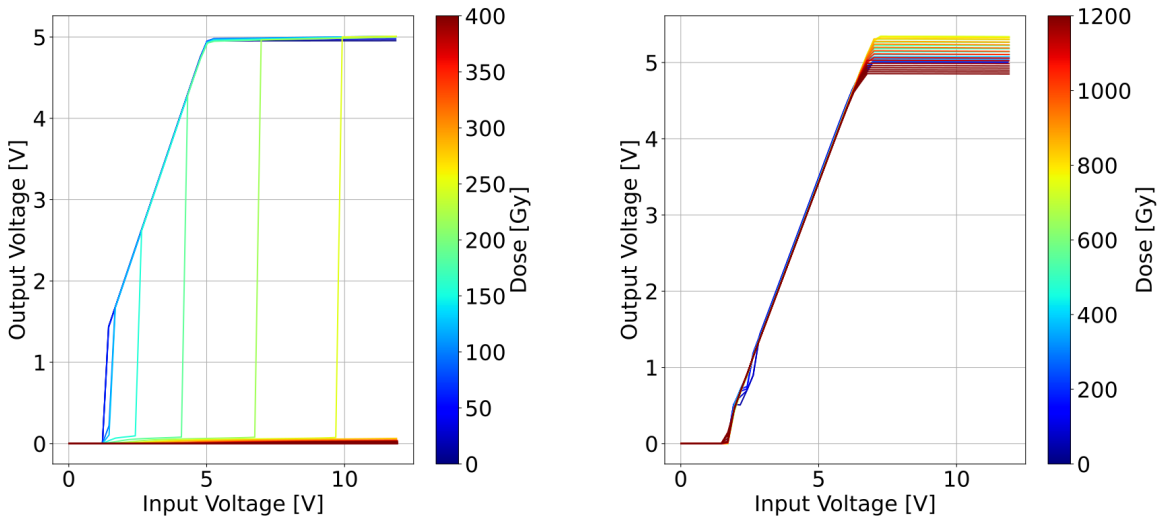

(a) (b)

Figure 4.36: Typical input characteristic of a voltage regulator. (a) Effect of the increase of the start-up voltage. (b) Device whose start-up voltage is insensitive to radiation.

irradiation, if the regulator is sensitive to the increase of the start-up voltage, the point in which the device starts to regulate slowly increases with the cumulated dose up to the maximum input voltage value as visible in Figure 4.36(a), after that point the regulator stops working. Figure 4.36(b) shows a device insensitive to start-up voltage degradation, the input characteristic remains constant until the end of the irradiation. Similarly to the case of the increase in the output voltage, the increase in the start-up voltage can also be related to the increase in the leakage current of one of the internal transistors [25], but the validation of this hypothesis in the case of the tested devices would require circuit simulations that are not the objectives of this thesis. Since the behaviours are very similar, only two visual examples are provided: the LT1085 and the MIC29302.
The evolution of the start-up voltage of the LT1085 is illustrated in Figure 4.37, the profile associated to the gamma irradiation (red line in figure) is constant up to 1.4 kGy, the increase is strongly related to the presence of displacement damage. As already mentioned, this behaviour is correlated to the output voltage drop shown in Figure 4.30, the increase of the start-up voltage above the maximum input voltage causes the complete failure of the device. A confirmation is the absence of output voltage drop associated to the gamma irradiation, since in that condition the start-up voltage remains below the

input voltage value, the sudden drop does not occur. Even if the increase of the start-up voltage occurs only in mixed-field environments and seems to be related to the presence of neutrons, it is actually due to the combined effects of TID and DD. In fact, if the profiles corresponding to the results obtained at CHARM are plotted as a function of the DDEF, the curves don't coincide. For this reason the analysis is performed as mentioned before

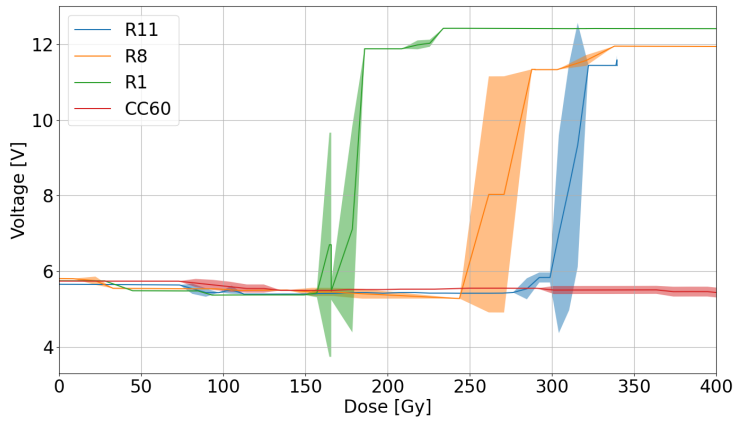

Figure 4.37: Start-up voltage degradation profiles of the voltage regulator LT1085 at different DDEF/TID ratios.

by considering the relation between the start-up voltage and the ratio DDEF/TID. In this case, the linear fit of the data is a good choice, the p-value associated to the reduced χ^2 test is equal to 73%, there are no synergistic effects of ionizing and non-ionizing dose. For this device the effect of the ionizing dose on the start-up voltage increase occurs only in presence of both ionizing and non-ionizing dose, condition in which the two contributions are additive.
Similarly to the LT1085, the MIC29302 shows a rapid increase of the start-up voltage in all the test positions, the profiles are illustrated in Figure 4.38. But in this case also the curve associated to the gamma irradiation (red in figure) exhibits an increase after 200 Gy. The correlation between the increase of the start-up voltage and the sudden drop of the output voltage depicted in Figure 4.27 is clear: the consequence of the increase of the start-up voltage in all the irradiation conditions is the sudden drop of the output voltages of all the devices tested in all the conditions. The same analysis previously per-

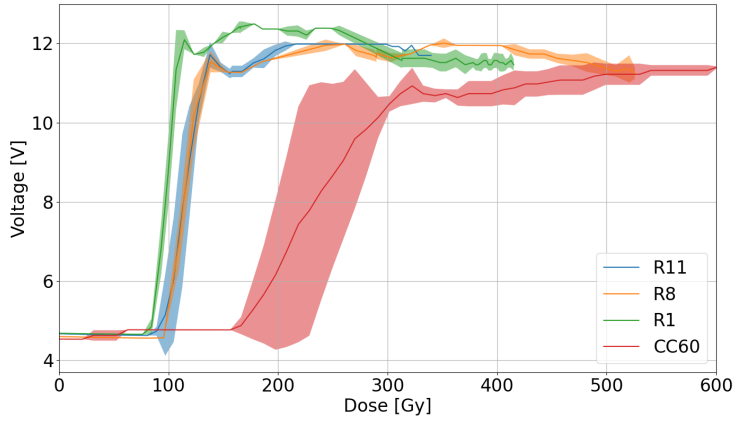

Figure 4.38: Start-up voltage degradation profiles of the voltage regulator MIC29302 at different DDEF/TID ratios.

formed to the LT1085 can be applied to the MIC29302 as visible in Figure 4.39. The

p-value associated to the reduced χ^2 test is equal to 9%, a sublinear function would fit better the data, but the p-value is not low enough to exclude the linear relation: there are no synergistic effects of total ionizing dose and displacement damage.

Concerning the remaining voltage regulators, they are all analyzed in the same way al-

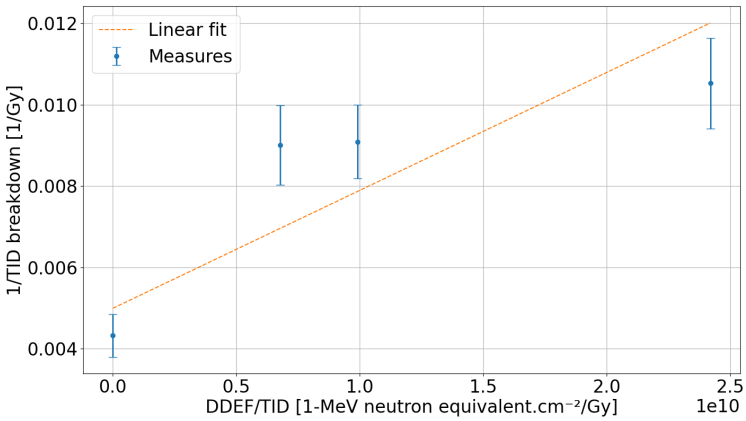

Figure 4.39: Relation between the breakdown dose of the LT1085 start-up voltage and the ratio DDEF/TID.

ready explained. The LM2936 exhibits synergistic effects in the start-up voltage increase: the p-value associated to the reduced χ^2 test performed on its data is lower than 5%. The ionizing dose causes the enhancement of the displacement damage effects on the increase of the start-up voltage. On the other hand, the p-value associated to the test of the LT1763 is equal to 97%, its relation between start-up increase and ratio DDEF/TID is strongly linear, the LT1763 does not show synergistic effects. Finally, the start-up voltage of the TPS73033 does not degrade during irradiation.

4.6 Voltage References

4.6.1 Output Voltage

In general, the voltage references exposed to radiation environments behave similarly to the voltage regulators in terms of profiles, but they degrade less in terms of magnitude. The references are more robust to radiation.

The output voltage evolution of the voltage reference AD435 is depicted in Figure 4.40. It is possible to notice two opposite trends: initially the output voltage decreases with the dose as visible in the zoom of the image, after a certain dose value the voltage increases until it reaches a peak. As proposed in [44], this behaviour is likely due to the combination of the voltage reference cell degradation and the internal operational amplifier degradation. The presence of the displacement damage does not change the shape, but it enhances the two behaviours: the higher the displacement damage, the higher the initial decrease and the earlier the peak.

Considering the first part of the degradation profiles the obtained DD contributions to the damage are shown in Figure 4.41. Also in this case, the ionizing dose enhances the effects of the displacement damage on the output voltage degradation. In fact, at same cumulated dose, the lower the DDEF/TID ratio, the higher the degradation. The ANOVA test of the three resulting profiles results in a p-value lower than 5%: the presence of synergistic effects is confirmed.

The second voltage reference is the MAX6350, the output voltage degradation is repre-

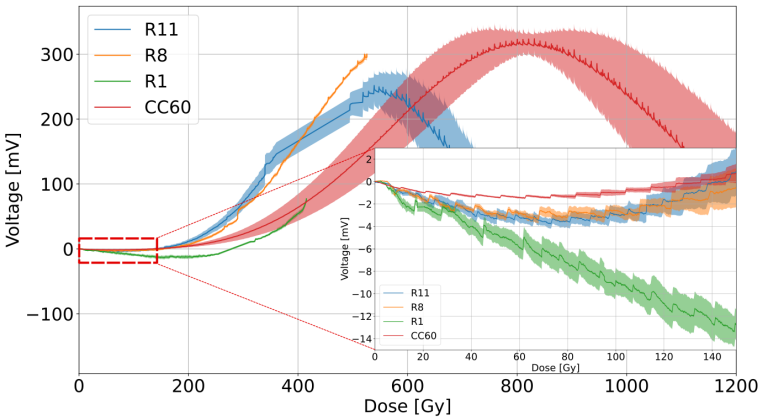

Figure 4.40: Output voltage degradation of the voltage reference ADR435 at different DDEF/TID ratios with a zoom of the initial part of the profiles.

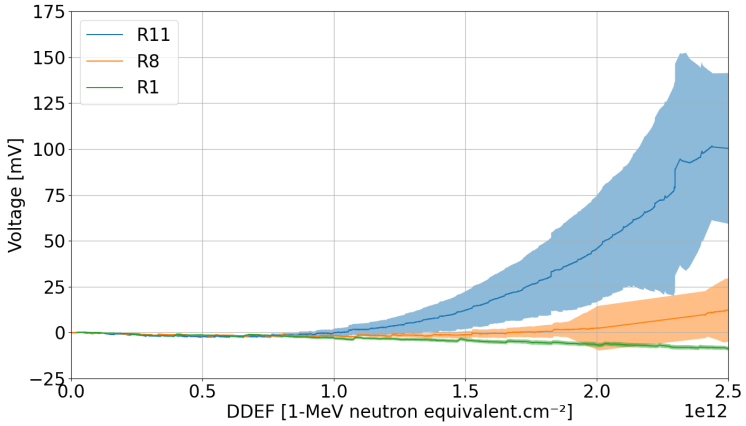

Figure 4.41: Displacement damage contributions to the degradation of the voltage reference ADR435.

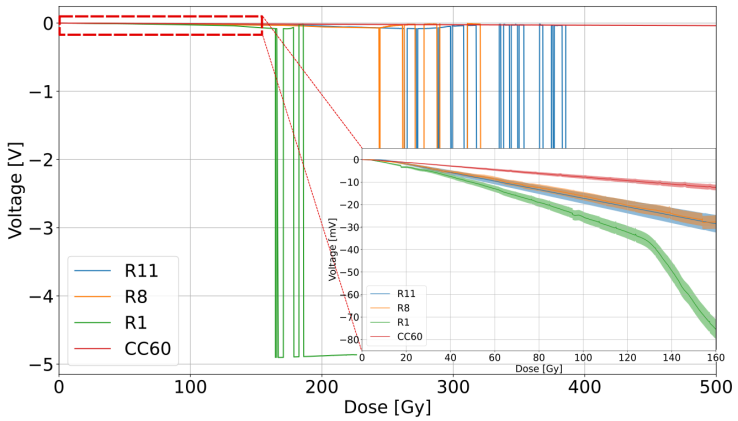

Figure 4.42: Output voltage degradation of the voltage reference MAX6350 at different DDEF/TID ratios with a zoom of the initial part of the profiles.

sented in Figure 4.42. The initial part of the curves is a gradual decrease of the output voltage followed by the sudden drop of the voltage. Both behaviours are due to the combination of ionizing and non-ionizing dose, the higher is the displacement damage, the worse the initial degradation and the earlier the drop. The only exception is the red

curve, corresponding to the gamma irradiation, that does not show any sudden drop. The relation between the inverse of the mean doses at which the sudden drop occurs and the ratio DDEF/TID can be fitted with a linear function of the ratio DDEF/TID. The p-value associated to the reduced χ^2 test is equal to 62%: the reduction of the breakdown dose can be explained by the additive combination of TID and DD, there are no synergistic effects.

On the other hand, the initial gradual degradation can be separated into TID and DD

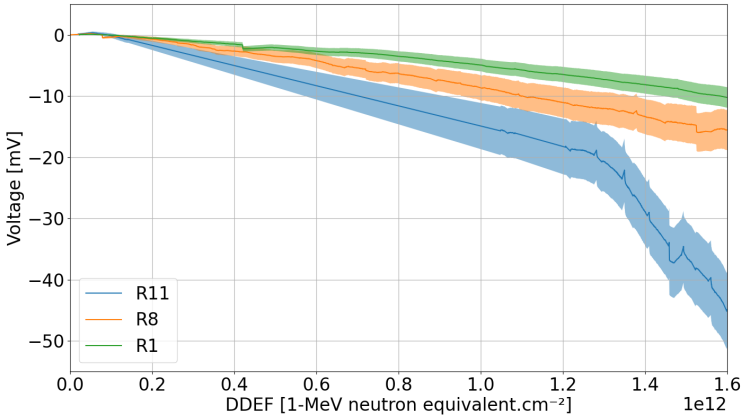

Figure 4.43: Displacement damage contributions to the degradation of the voltage reference MAX6350.

contributions, the DD contributions are shown in Figure 4.43. Similarly to previous cases, the profiles suggest the presence of a positive impact of the ionizing radiation on the displacement damage effects. In fact, devices that are subjected to higher TID at same DDEF (low DDEF/TID ratio) exhibit higher degradation contribution due to displacement damage. The p-value associated to the ANOVA test performed to the three profiles is below 5%: also in this case the presence of synergistic effects is confirmed.

4.6.2 Start-up Voltage

Concerning the start-up voltage of the voltage references, all the analysis and the considerations done for the voltage regulators apply also in this case.

The start-up voltage of the ADR435 does not degrade during the irradiation regardless the test positions and the amount of displacement damage they suffered.

On the contrary, the increase of the start-up voltage of the MAX6350 depicted in Figure 4.44 appears only during mixed-field irradiation. At equal cumulated dose, the higher the displacement damage, the earlier the degradation. But, as in previous cases, it is not only due to the presence of displacement damage, the degradation profiles don't coincide if they are reported as a function of the displacement damage equivalent fluence. The degradation is due to the combined effects of TID and DD.

Also in this situation, the presence of synergistic effects is evaluated by fixing a threshold on the start-up voltage to obtain for each test position the mean doses at which the voltage overcomes the threshold. The resulting doses are fitted with a linear function of the ratio DDEF/TID. The p-value associated to the reduced χ^2 test of the fit is equal to 49%: the null hypothesis cannot be rejected, there are no synergistic effects on the increase of the start-up voltage.

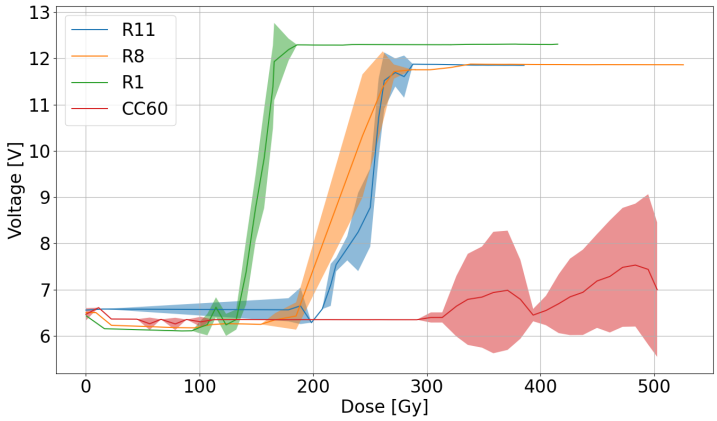

Figure 4.44: Start-up voltage degradation profiles of the voltage reference MAX6350 at different DDEF/TID ratios.

4.7 IGBTs

4.7.1 Threshold Voltage

Similarly to the MOSFET under irradiation, the IGBTs exhibit a decrease of the threshold voltage due to the charge accumulated in the gate oxide. While the displacement damage can deteriorate the structure of the device, in particular the output BJT stage, leading to more complex degradation profiles. In fact, a decrease in the current gain can lead to an increase in the base current required to turn on the device, with a consequent shift of the input characteristic towards higher input voltages and an increase in the measured threshold voltage. Figure 4.45 shows the input characteristics ($I_{collector}$ vs V_{gate}) of the two tested references AUIRG4PH50S and IKW13N120BH6. As the cumulated dose increases, the transition between non-conductive and conductive state occurs earlier. In both cases the threshold voltage becomes negative before the end of the irradiation, in this condition it is impossible to turn off the devices.

The shift of the AUIRG4PH50S threshold voltage as a function of the ionizing dose

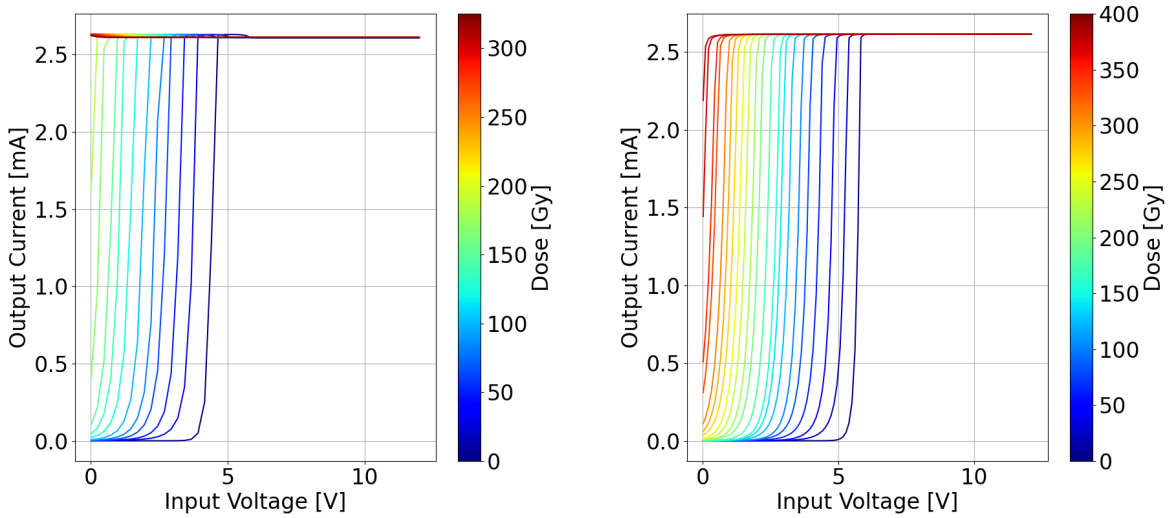

Figure 4.45: Typical input characteristic of an IGBT under irradiation: (a) AUIRG4PH50S and (b) IKW13N120BH6.

is depicted in Figure 4.46 for each test position. The degradation is stronger in mixed field environment, but, surprisingly, the degradation in position R1 with the highest ratio DDEF/TID is lower than that in positions R11 and R8. This behaviour is unexpected because at higher displacement damage corresponds lower degradation, the contribution of the displacement damage evaluated in the profiles as a function of the TID does not reach the 25%. The IKW13N120BH6 behaves in the same way and its displacement damage contributions range from 20% to 40%. The threshold voltage shift in both devices is driven mainly by the ionizing dose. From the degradation profiles it is possible to extract

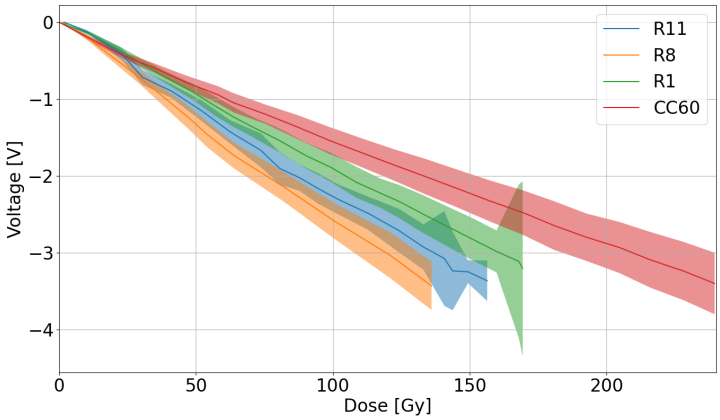

Figure 4.46: Threshold voltage degradation profiles of the IGBT AUIRG4PH50S at different DDEF/TID ratios.

the displacement damage contributions illustrated in Figure 4.47. The DD contributions in positions R11 and R8 coincide during the entire irradiation, while the contribution associated to the position R1 is very different from the others and it is close to zero. In the considered DDEF range, the R1 and the CC60 profiles are superimposed, the degradation can be explained as the effect of the ionizing dose only.
Due to the great difference between the R1 profile and the other two, the p-value associated to the ANOVA test performed on the DD contributions to the damage of the AUIRG4PH50S (shown in Figure 4.47) is lower than 5%. The presence of synergistic effects is confirmed, the ionizing dose enhances the effects of the displacement damage.
On the other hand, even if the IKW13N120BH6 exhibits the same behaviour regarding

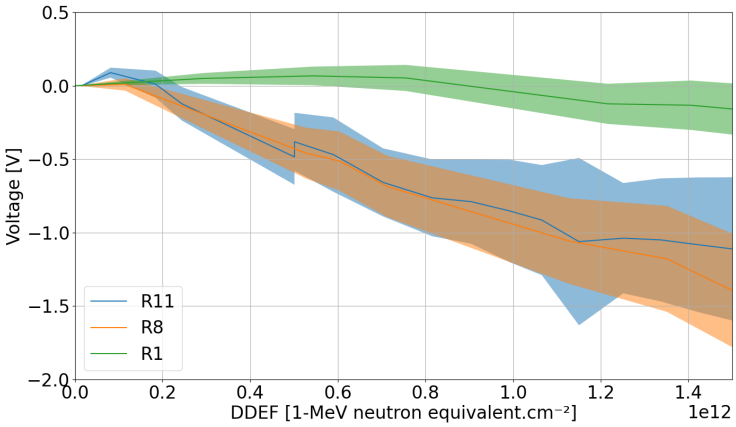

Figure 4.47: Displacement damage contributions to the degradation of the threshold voltage of the IGBT AUIRG4PH50S.

the lower degradation in the R1 position, the displacement damage contributions to the

threshold voltage shift are not enough separated to confirm the synergy between TID and DD, the p-value of the ANOVA test is higher than 5%.

4.8 PhotoMOS

4.8.1 Start-up Current

The start-up current increase of the PhotoMOS is mostly caused by the efficiency reduction of the input LED, the damage of the lattice of the LED material leads to lower light intensity at same applied current. For this reason it is important to know what is the material that composes the LED. The value of displacement damage equivalent fluence measured by the RadMON deported module refers to the damage in Silicon, since the LED material is usually different from Silicon, the value of DDEF is not correct for the evaluation of the PhotoMOS. Except for the AQW210S whose LED material is unknown, the LED material of the tested devices is GaAlAs. Fortunately, the characterization of

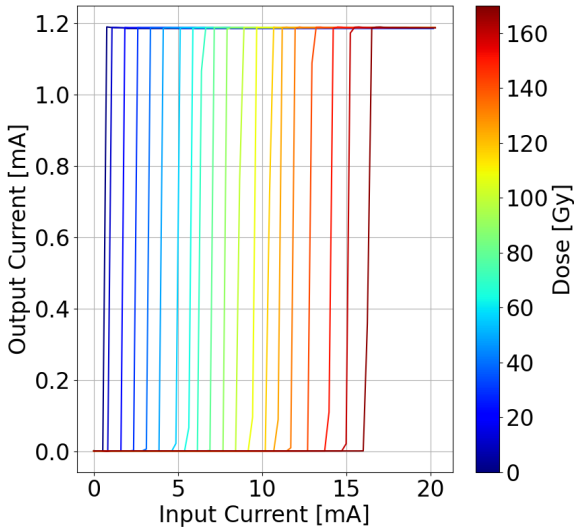

Figure 4.48: Input characteristic of the PhotoMOS AQW210S under mixed-field irradiation.

some CHARM positions for the GaAlAs has been done in [53], the displacement damage equivalent fluence evaluated in Silicon must be scaled with a factor calculated as ratio between the hardness factor of the GaAlAs and the hardness factor of Silicon.

$$DDEF(GaAlAs) = \frac{\kappa(GaAlAs)}{\kappa(Si)} DDEF(Si) \tag{4.34}$$

The hardness factors (κ) are calculated taking into account the radiation environment in the different CHARM positions in terms of type of particles and energies. The resulting scaling factors are shown in Table 4.2.

Figure 4.48 shows the evolution of the input characteristic (I_{out} vs I_{in}) of the PhotoMOS AQW210S that is representative of the devices whose start-up current is sensitive to radiation, it is visible the evident increase of the minimum input current needed to turn on the device.

The start-up current of all the tested references degrades during the irradiation, except the ASSR-1218-003E whose start-up current does not degrade regardless the test position and the ratio DDEF/TID.

	CHARM R1	CHARM R8	CHARM R11
$\frac{\kappa(GaAlAs)}{\kappa(Si)}$	1.96	2.88	6.81

Table 4.2: Ratio between the hardness factors of GaAlAs and Silicon in the three CHARM test positions.

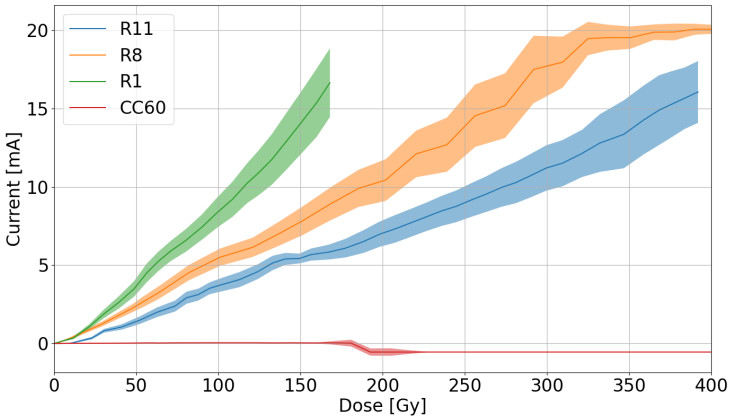

Figure 4.49: Start-up current degradation profiles of the PhotoMOS AQW210S at different DDEF/TID ratios.

The start-up current increase of the PhotoMOS AQW210S is depicted in Figure 4.49 as a function of the cumulated dose and at different DDEF/TID ratios. While at CC60 (gamma irradiation) the start-up current does not increase during all the irradiation, it increases strongly under mixed-field irradiation with an evident dependence on the displacement damage. The degradation profiles as a function of the displacement damage

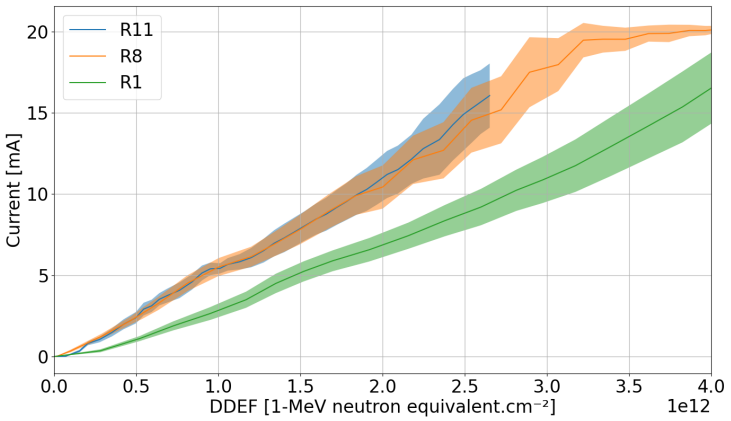

Figure 4.50: Displacement damage contributions to the start-up current degradation of the PhotoMOS AQW210S.

equivalent fluence are illustrated in Figure 4.50. The devices tested in positions R8 and R11 respond to the displacement damage in a very similar way, the profiles are superimposed. On the contrary, the devices tested in position R1 suffered a lower degradation as a function of the DDEF. The ionizing dose enhances the effects of the displacement damage, the devices exposed to higher amount of ionizing dose exhibit higher degradation. The p-value associated to the ANOVA test performed on the three profiles is lower than 5%, the presence of synergistic effects is confirmed. However, it is important to remember once again that the LED material of the AQW210S is unknown and this result is limited

by that ignorance.
The start-up current of the PVA3354 is depicted in Figure 4.51, as in the previous case, the gamma irradiation does not cause the increase of the current, it is visible only in mixed-field environments where the displacement damage is present. The degradation

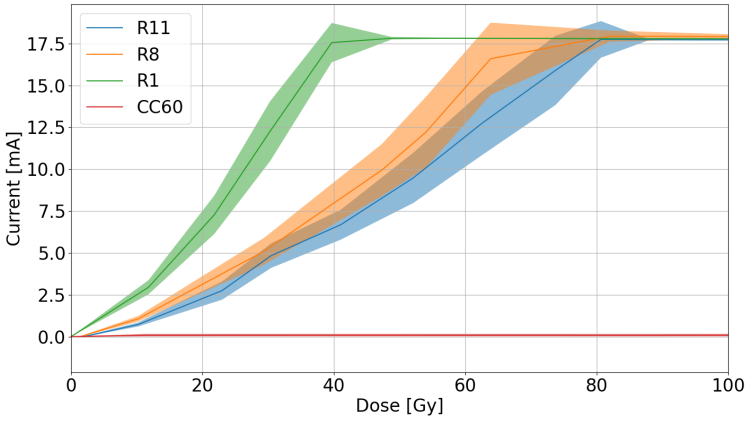

Figure 4.51: Start-up current degradation profiles of the PhotoMOS PVA3354 at different DDEF/TID ratios.

profiles as a function of the DDEF scaled for the GaAlAs are visible in Figure 4.52. Although in R1 and R8 start-up current degradation is almost equal, the profile in R11 is very different from the others. The degradation is lower at higher DDEF/TID ratio. This case of synergistic effect is a moderation of the displacement damage contribution due to the ionizing dose. However, this difference can be due to the uncertainty of the scaling factor for the position R11. In fact, in that position the displacement damage is mainly due to protons and pions whose NIEL is not well simulated.

Interestingly, if the scaling factor associated to the R11 position is reduced to 3.5, the

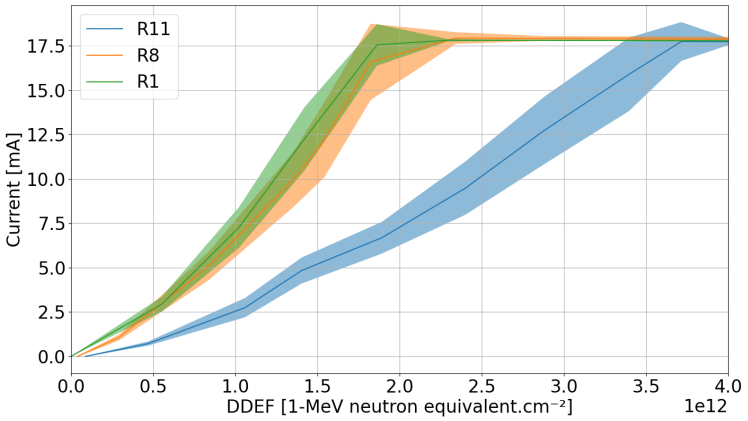

Figure 4.52: Displacement damage contributions to the start-up current degradation of the PhotoMOS PVA3354 as a function of the DDEF in GaAlAs.

three profiles are exactly superimposed. In addition, if the DDEF axis of the AQW210S is scaled as if its LED is made of GaAlAs with the adjusted R11 factor, also the start-up current increase of the AQW210S superimpose almost perfectly. Since the input LED of the photoMOS is separated from the rest of the circuit, these results suggest that the increase of the start-up current actually depends only on displacement damage, that the DDEF scaling factor from Silicon to GaAlAs is incorrectly calculated, and that the LED

material of the AQW210S is most likely GaAlAs.
On the other hand, the VOR1142 behaves very differently from the other three references: it exhibits a slight increase of the start-up current that reaches at maximum 3.5 mA while in the other two degraded references the increase is higher than 15 mA. In addition, VOR1142 degrades when subjected to mixed field radiation, but in R8 it surprisingly does not degrade as visible in Figure 4.53. Figure 4.54 shows the degradation profiles of

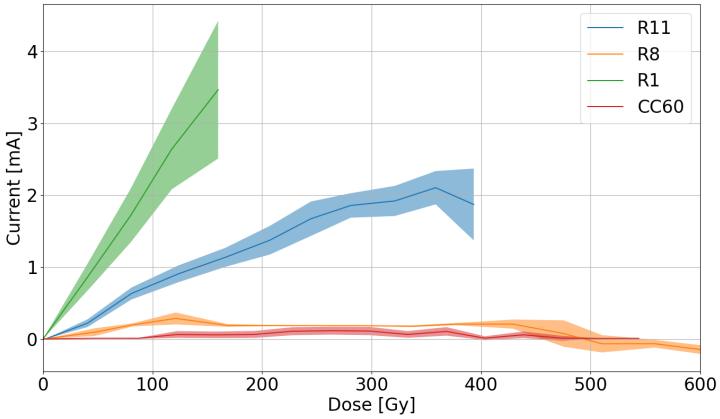

Figure 4.53: Start-up current degradation profiles of the PhotoMOS VOR1142 at different DDEF/TID ratios.

the VOR1142 start-up current in positions R1 and R8 as a function of the displacement damage equivalent fluence in GaAlAs. The result is equal to the one obtained as a

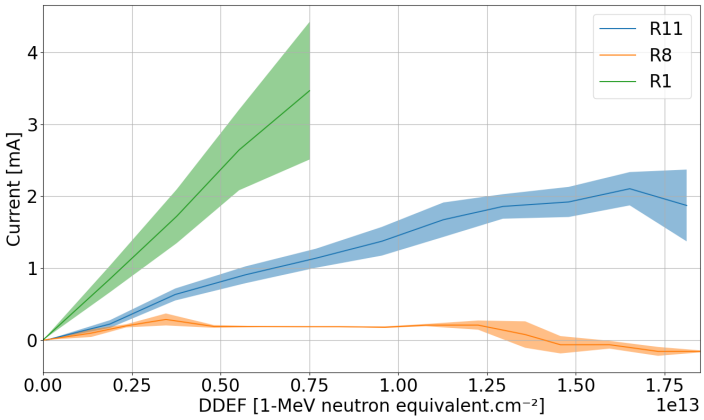

Figure 4.54: Displacement damage contributions to the start-up current degradation of the PhotoMOS VOR1142 as a function of the DDEF in GaAlAs.

function of the ionizing dose: the profile corresponding to the test in position R8 is close to zero, while the one corresponding to the test in R1 increases up to $\sim$ 3.5 mA. The strong difference between the two behaviours confirm the presence of synergistic effects, but in this case the degradation is higher at high value of DDEF/TID ratio, suggesting a moderation of displacement damage due to the ionizing dose. In fact, the devices tested in position R8 are subjected to a higher ionizing dose than those tested in R1. If, for the same DDEF, the devices in R8 are less degraded, it means that the ionizing dose acts as a moderator of the displacement damage.

4.8.2 Leakage Current

The drain leakage current of the PhotoMOS under irradiation is the result of the decrease of the threshold voltage of the output MOSFET. For this reason it is mainly due to the ionizing dose causing the charge trapping the MOSFET gate oxide. Figure 4.55 shows the input characteristic of the PhotoMOS AQW210S under gamma irradiation. As explained previously, the start-up current does not increase, the threshold between non-conductive and conductive state is stable at 0.6 mA. But the output current flowing when the input current is below the threshold increases with the dose reaching at the end of the irradiation its saturation value (1.2 mA). This phenomenon leads to the permanent conductive state of the device.

By measuring the drain current when the input current is zero it is possible to evaluate

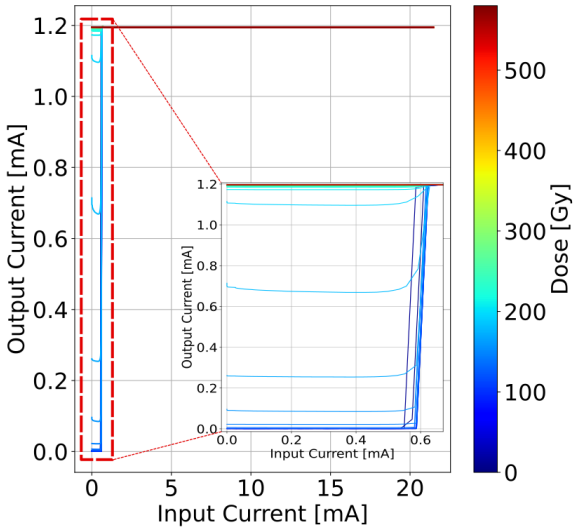

Figure 4.55: Input characteristic of the PhotoMOS AQW210S under gamma irradiation.

the degradation of the threshold voltage of the output MOSFET. Since the profiles are similar, only two examples are reported: AQW210S and ASSR-1218.

The AQW210S and the PVA3354 exhibit the increase of the drain current at zero imposed

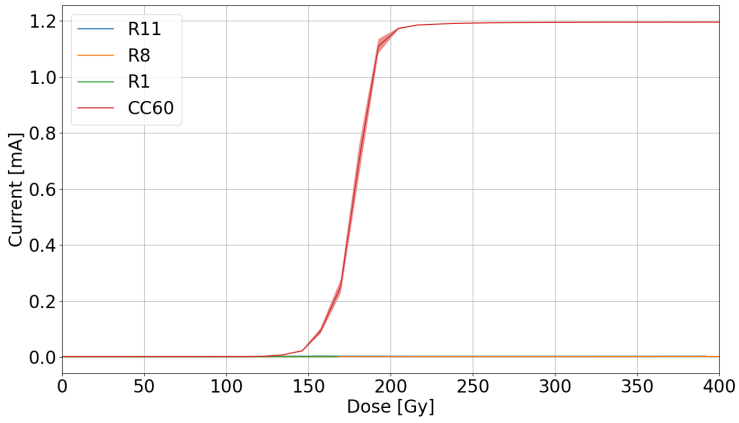

Figure 4.56: Drain leakage current profiles of the PhotoMOS AQW210S at different DDEF/TID ratios.

current only during gamma irradiation with the only difference on the dose value. The

AQW210S profile is shown in Figure 4.56, the transition of the threshold voltage from positive values to negative values happens between 150 Gy and 200 Gy. In the case of the PVA3354, the transition happens after 400 Gy with higher variability. Noticeably, these two references are the same whose start-up current does not degrade at CC60, while it degrades very quickly in mixed-field environments. As a consequence, at a certain cumulated dose value at CHARM, the imposed input current is not sufficient to turn on the output MOSFET, during the remaining part of the irradiation the output MOSFET is turned off leading to lower electric field inside the gate oxide, less charge separation and trapping and, consequently, lower degradation of the threshold voltage. Since at CC60 the start-up current is not affected, the output MOSFET remains conductive during all the irradiation leading to the threshold voltage shift and to the drain current increase.
On the other hand, the ASSR-1218 and the VOR1142 exhibit an increase of the drain current also during mixed-field irradiation. The increase of the VOR1142 happens at high ionizing dose, due to test time constraints the only visible increase is the one showed at CHARM in position R8 after 550 Gy. At CC60 the current was starting to increase, but the irradiation was stopped. However, the later increase of the current at CC60 suggest a combined effect of TID and DD on the drain leakage, the higher the displacement damage, the earlier the increase. Similarly to the previous case, the increase of the drain current is related to the start-up current increase, since both at CHARM and at CC60 the increase of the start-up current is absent (ASSR-1218) or very limited (VOR1142), the output MOSFET remains conductive during all the irradiation leading to a greater threshold voltage shift and drain current increase. The drain current profiles of the ASSR-1218 are

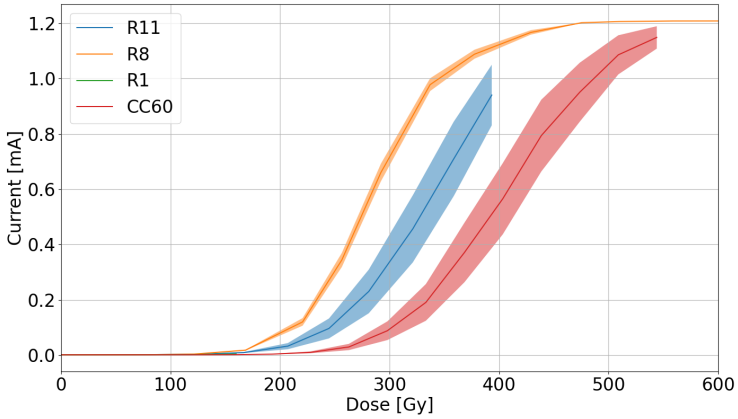

Figure 4.57: Drain leakage current profiles of the PhotoMOS ASSR1218 at different DDEF/TID ratios.

visible in Figure 4.57. As previously suggested for the VOR1142, both TID and DD cause the increase of the drain current at zero applied current, the results of the irradiation in the different test positions is a combined effect of ionizing and non-ionizing dose. In this case it is possible to evaluate the presence of synergistic effects by fixing a threshold drain current and calculating for each test position the mean ionizing dose at which the threshold is overcome. In absence of synergistic effects the relation between the inverse of the dose and the ratio DDEF/TID is linear (Equation 4.27). The p-value associated to the reduced χ^2 test is equal to 46%, the data can be fitted with a linear function of DDEF/TID and there are no synergistic effects.

4.9 Summary of the Results

The degradation of all the tested devices is due to the combination of total ionizing dose and displacement damage at least for one observed parameter, for those parameters the dominant contribution varies greatly from device to device. Seven out of twenty-two devices exhibit complete failure during the irradiation. Table 4.3 summarizes the results I obtained in terms of presence of synergistic effects in the tested devices. The presence of those effects is confirmed only if at least one tested parameter showed synergy between ionizing and non-ionizing dose.
Interestingly, almost the 50% of the tested devices exhibits synergistic effects in one parameter without any difference in distribution between all the types of devices. Consequently, there are no types of devices that can be excluded a priori from the analysis of synergistic effects in a radiation qualification procedure.
Another important notice is that among the ten BiCMOS references, five of them are affected by synergistic effects.More studies should be carried out to evaluate any differences between the two technologies, but the data obtained in this study suggest that the distribution of the sensitivity to synergistic effects is equal in bipolar and BiCMOS devices.

Type	**Reference**	**Synergy**	**Reference**	**Synergy**
Operational Amplifier	AD829	✓	LM358AD	✓
	MAX4238AUT+T	X	LT1013	X
Instrumentation Amplifier	INA326	X	AD621	X
	AD8420	✓	MAX4208	✓
Voltage Reference	MAX6350	✓	AD435TRZ-EP	✓
Voltage Regulator	LM2936MP-5.0	✓	LT1085	X
	TPS73033	X	MAX8881EUT50	✓
	LT1763IS8	X	MIC29302	X
IGBT	AUIRG4PH50S	✓	IKW15N120BH6	X
PhotoMOS	PVA3354NS	X	AQW210S	✓
	VOR1142M4	✓	ASSR-1218-003E	X

Table 4.3: Summary of the results on the presence of synergistic effects in the tested components. The presence of synergy is confirmed if at least one parameter shows synergistic effects.

4.10 Impact on CERN RHA

As demonstrated in the previous paragraphs, the degradation of the tested devices is caused by the combination of total ionizing dose and displacement damage in at least one performance parameter. Not all the devices exhibit synergistic effects of ionizing and non-ionizing dose, the degradation profile of some of them can be effectively separated into two additive contributions of TID and DD. On the other hand, most of the devices showing a sensitivity to synergistic effects exhibit a similar behavior when varying the DDEF/TID ratio: the smaller the ratio, the larger the displacement damage contribution to degradation. The ionizing dose causes the enhancement of the displacement damage effects on the device parameter. In addition, as mentioned previously, the presence of

synergistic effects is distributed uniformly among all the tested devices, thus, during the qualification procedure, there are no types of devices that can be excluded from the analysis of those effects.
The impact of these conclusions on the CERN Radiation Hardness Assurance is encouraging. In the case of devices insensitive to synergistic effects, the two contributions can be extracted by performing a couple of tests: one at CC60 and one at CHARM, or at CHARM in two different test positions having different DDEF/TID ratio. If the time constraints don't allow this first approach, one test must be performed in a mixed-field environment (CHARM) and a safety margin can be applied to the results. In the specific case of the tested devices, since the displacement damage contributions represent at most 50% of the total degradation in position R11 (except for the AD8420 whose degradation is completely due to displacement damage), the margins could be very high. In some LHC locations, the ratio DDEF/TID could be hundred times the one in R13. As a consequence, the degradation encountered in R13 must be multiplied by 50 (if we consider the damage caused in equal part by TID and DD) and then scaled with the ratio between the required TID levels in operation and the TID cumulated under test.
Concerning the components that exhibit synergistic effects, the nature of the synergy between TID and DD is beneficial for the RHA for several reasons. First, the position in which the CERN systems are usually tested for the evaluation of the radiation tolerance is the CHARM position R13, it is the position with higher dose rate (it is the closest to the target) and lower DDEF/TID ratio. It means that the current test procedure is conservative in case of synergistic effects because it overestimates the displacement damage contribution. Second, applying safety margins as if the devices are not affected by synergistic effects is a conservative approach. In fact, if the margin used to cover the increase in degradation due to DD in positions with a DDEF/TID ratio higher than that of position R13 is appropriate for devices not affected by synergistic effects, it will certainly be suitable for devices affected by synergies that will exhibit less degradation.
Although these effects will not lead to the worst case scenario in which a qualified device cannot withstand the radiation levels to which is subjected, they may become a problem with the increase of the luminosity of the LHC or the FCC. In fact, in these situations it may be difficult to find COTS devices that pass the qualification because of the overestimation of the damage. A more accurate analysis of the device degradation may be necessary by testing in a radiation environment representative of the operation environment in terms of DDEF/TID ratio or by testing at several DDEF/TID ratios to extrapolate a dependence of the degradation profile and lifetime on such ratio.

Conclusions

The aim of my thesis was to verify the sensitivity to synergistic effects between ionizing dose and displacement damage of bipolar and BiCMOS devices and how these effects could affect the radiation qualification procedure of the devices operating in the LHC at CERN.
The project was divided into several steps. First, I selected the bipolar and BiCMOS components considered as good candidates for the project. After the choice of the tested parameters for each type of device, I designed three test boards to be compatible with the irradiation facilities and the available equipment. I selected the test facilities to allow testing in different conditions: Cobalt 60 for the pure TID irradiation and CHARM for the mixed-field (TID+DD) irradiation. After planning the tests and producing the necessary equipment, such as the stand-alone rack, the cable chain and the connector adapters, I performed the irradiation tests.
The main focus of the activity was the test campaigns: I carried out the evaluation of the synergistic effects by exposing the devices to different radiation environments in terms of ratio between displacement damage equivalent fluence and total ionizing dose. From the four degradation profiles obtained at Cobalt 60 and in three test positions at CHARM I extrapolated the displacement damage contributions to the overall degradation. Any differences in those contributions suggested the presence of synergistic effects of ionizing and non-ionizing dose.
The analysis of the results obtained from the intensive test campaigns demonstrates the existence of synergistic effects of TID and DD in approximately the 50% of the devices with a uniform distribution between different types of devices and different technology (bipolar and BiCMOS). In most of the cases, the displacement damage contribution extracted from the overall degradation profile increases as the DDEF/TID ratio decreases, in other words, the DD profile extracted from the measurements in CHARM position R11 (DDEF/TID=$6.8 \cdot 10^9$ $1MeVn - eq/cm^2/Gy$) is higher then that extracted from the measurements in CHARM position R1 (DDEF/TID=$2.4 \cdot 10^{10}$ $1MeVn - eq/cm^2/Gy$) showing an enhancement of the DD contribution when the device is exposed to higher levels of ionizing dose. The physical mechanisms and the circuit level causes of the synergies are not the objectives of this thesis and would required a deeper analysis for each tested device with simulations of the internal circuit. However, in a qualification perspective a "low-level" approach would be inefficient: it would require a lot of time and effort to understand if a single device can be used. For this reason, an "high-level" approach like the one proposed is more suitable for the time constraints due to the qualification process and the high demand of components to be qualified.
These types of synergistic effects do not currently constitute a problem for the qualification procedure: since testing at low DDEF/TID is the worst case scenario, the current way of performing the qualification tests (position R13 at CHARM) results in the overestimation of the displacement damage contribution for most of the LHC positions. By applying safety margin to take into account the higher displacement damage equivalent

fluence, there is no risk of qualifying a device that cannot withstand such radiation levels. However, the safety margins could be very high depending on the displacement damage contribution to the overall degradation. On the other hand, there is the opposite risk in term of qualification: some devices can be excluded from the systems design even if they could tolerate the radiation levels in operation only because the test and the margin are overestimating the damage. This is a minor issue, but in a future scenario where HL-LHC or FCC are operational, it could become a major issue due to higher radiation levels leading to narrower margins for qualification. The large quantity of devices that will be necessary for the improvement of the accelerator complex will lead to the development of new qualification procedures that will take into account the synergistic effects of the ionizing and non-ionizing dose to obtain a more realistic prediction of the behavior of the devices under irradiation.

Bibliography

[1] Rubén García Alía, Markus Brugger, Francesco Cerutti, Salvatore Danzeca, Alfredo Ferrari, Simone Gilardoni, Yacine Kadi, Maria Kastriotou, Anton Lechner, Corinna Martinella, et al. Lhc and hl-lhc: Present and future radiation environment in the high-luminosity collision points and rha implications. IEEE Transactions on Nuclear Science, 65(1):448–456, 2017.

[2] Michael Benedikt, Alain Blondel, Patrick Janot, Michelangelo Mangano, and Frank Zimmermann. Future circular colliders succeeding the lhc. Nature Physics, 16(4):402–407, 2020.

[3] Rudy Ferraro. Development of Test Methods for the Qualification of Electronic Components and Systems Adapted to High-Energy Accelerator Radiation Environments. PhD thesis, Université Montpellier, 2019.

[4] Timothy R Oldham and FB McLean. Total ionizing dose effects in mos oxides and devices. IEEE transactions on nuclear science, 50(3):483–499, 2003.

[5] HJ Barnaby. Total-ionizing-dose effects in modern cmos technologies. IEEE transactions on nuclear science, 53(6):3103–3121, 2006.

[6] James R Schwank, Marty R Shaneyfelt, Daniel M Fleetwood, James A Felix, Paul E Dodd, Philippe Paillet, and Véronique Ferlet-Cavrois. Radiation effects in mos oxides. IEEE Transactions on Nuclear Science, 55(4):1833–1853, 2008.

[7] DM Schmidt, DM Fleetwood, RD Schrimpf, RL Pease, RJ Graves, GH Johnson, KF Galloway, and WE Combs. Comparison of ionizing-radiation-induced gain degradation in lateral, substrate, and vertical pnp bjts. IEEE Transactions on Nuclear Science, 42(6):1541–1549, 1995.

[8] S.L. Kosier, R.D. Schrimpf, R.N. Nowlin, D.M. Fleetwood, M. DeLaus, R.L. Pease, W.E. Combs, A. Wei, and F. Chai. Charge separation for bipolar transistors. IEEE Transactions on Nuclear Science, 40(6):1276–1285, 1993.

[9] D.M. Schmidt, A. Wu, R.D. Schrimpf, D.M. Fleetwood, and R.L. Pease. Modeling ionizing radiation induced gain degradation of the lateral pnp bipolar junction transistor. IEEE Transactions on Nuclear Science, 43(6):3032–3039, 1996.

[10] SL Kosier, WE Combs, A Wei, RA Schrimpf, DM Fleetwood, M DeLaus, and RL Pease. Bounding the total-dose response of modern bipolar transistors. IEEE transactions on nuclear science, 41(6):1864–1870, 1994.

[11] Ronald L Pease, Philippe Claude Adell, Bernard G Rax, Xiao Jie Chen, Hugh J Barnaby, Keith E Holbert, and Harold P Hjalmarson. The effects of hydrogen on the enhanced low dose rate sensitivity (eldrs) of bipolar linear circuits. IEEE Transactions on Nuclear Science, 55(6):3169–3173, 2008.

[12] Ronald L Pease, Ronald D Schrimpf, and Daniel M Fleetwood. Eldrs in bipolar linear circuits: A review. In 2008 European Conference on Radiation and Its Effects on Components and Systems, pages 18–32. IEEE, 2008.

[13] J Boch, Frédéric Saigné, RD Schrimpf, J-R Vaille, L Dusseau, and E Lorfevre. Physical model for the low-dose-rate effect in bipolar devices. IEEE transactions on nuclear science, 53(6):3655–3660, 2006.

[14] Susan Wood, NJ Doyle, JA Spitznagel, WJ Choyke, RM More, JN McGruer, and RB Irwin. Simulation of radiation damage in solids. IEEE Transactions on Nuclear Science, 28(6):4107–4112, 1981.

[15] JR Srour and JW Palko. Displacement damage effects in irradiated semiconductor devices. IEEE Transactions on Nuclear Science, 60(3):1740–1766, 2013.

[16] Andrew Holmes-Siedle and Len Adams. Handbook of radiation effects. Oxford university press, 2002.

[17] KF Galloway, RL Pease, RD Schrimpf, and DW Emily. From displacement damage to eldrs: Fifty years of bipolar transistor radiation effects at the nsrec. IEEE Transactions on Nuclear Science, 60(3):1731–1739, 2013.

[18] Sananda Velacheri, LW Massengill, and Sh E Kerns. Single-event-induced charge collection and direct channel conduction in submicron mosfets. IEEE transactions on nuclear science, 41(6):2103–2111, 1994.

[19] A. Ochoa, F. W. Sexton, T. F. Wrobel, G. L. Hash, and R. J. Sokel. Snap-back: A stable regenerative breakdown mode of mos devices. IEEE Transactions on Nuclear Science, 30(6):4127–4130, 1983.

[20] Fred W Sexton. Destructive single-event effects in semiconductor devices and ics. IEEE Transactions on Nuclear Science, 50(3):603–621, 2003.

[21] E. L. Petersen. Single-event data analysis. IEEE Transactions on Nuclear Science, 55(6):2819–2841, 2008.

[22] H.J. Barnaby, R.D. Schrimpf, A.L. Sternberg, V. Berthe, C.R. Cirba, and R.L. Pease. Proton radiation response mechanisms in bipolar analog circuits. IEEE Transactions on Nuclear Science, 48(6):2074–2080, 2001.

[23] HJ Barnaby, SK Smith, RD Schrimpf, DM Fleetwood, and RL Pease. Analytical model for proton radiation effects in bipolar devices. IEEE Transactions on Nuclear Science, 49(6):2643–2649, 2002.

[24] Liu Yan, Chen Wei, Yang Shanchao, Jin Xiaoming, and He Chaohui. Synergistic effect of mixed neutron and gamma irradiation in bipolar operational amplifier op07. Nuclear Instruments and Methods in Physics Research Section A: Accelerators, Spectrometers, Detectors and Associated Equipment, 831:334–338, 2016. Proceedings of the 10th International "Hiroshima" Symposium on the Development and Application of Semiconductor Tracking Detectors.

[25] Rudy Ferraro, Rubén García Alía, Salvatore Danzeca, and Alessandro Masi. Analysis of bipolar integrated circuit degradation mechanisms against combined tid–dd effects. IEEE Transactions on Nuclear Science, 68(8):1585–1593, 2021.

[26] Rudy Ferraro, Salvatore Danzeca, Chiara Cangialosi, Rubén García Alía, Francesco Cerutti, Andrea Tsinganis, Luigi Dilillo, Markus Brugger, and Alessandro Masi.

Study of the impact of the lhc radiation environments on the synergistic displacement damage and ionizing dose effect on electronic components. IEEE Transactions on Nuclear Science, 66(7):1548–1556, 2019.

[27] Alessandro Zimmaro. Radiation Effects and System-Level Testing: Application to Wireless Communications. Effets Des Radiations Et Tests Au Niveau Système: Application Aux Communications Sans Fil, 2024. Presented 23 Jan 2024.

[28] TT Böhlen, Francesco Cerutti, MPW Chin, Alberto Fassò, Alfredo Ferrari, P Garcia Ortega, Andrea Mairani, Paola R Sala, George Smirnov, and Vasilis Vlachoudis. The fluka code: developments and challenges for high energy and medical applications. Nuclear data sheets, 120:211–214, 2014.

[29] G Spiezia, P Peronnard, A Masi, M Brugger, M Brucoli, S Danzeca, R Garcia Alia, R Losito, J Mekki, P Oser, et al. A new radmon version for the lhc and its injection lines. IEEE Transactions on Nuclear Science, 61(6):3424–3431, 2014.

[30] Eva Barbara Holzer, Bernd Dehning, Ewald Effinger, Jonathan Emery, Gianfranco Ferioli, Jose Luis Gonzalez, Edda Gschwendtner, Gianluca Guaglio, Michael Hodgson, Daniel Kramer, et al. Beam loss monitoring system for the lhc. In IEEE Nuclear Science Symposium Conference Record, 2005, volume 2, pages 1052–1056. IEEE, 2005.

[31] Radiation Working Group. Radiation test database - radwg tests.

[32] RL Pease. Total ionizing dose effects in bipolar devices and circuits. IEEE Transactions on Nuclear Science, 50(3):539–551, 2003.

[33] Thomas Borel, F Roig, Alain Michez, B Azais, S Danzeca, NJ-H Roche, F Bezerra, P Calvel, and L Dusseau. Atypical effect of displacement damage on lm124 bipolar integrated circuits. IEEE Transactions on Nuclear Science, 65(1):71–77, 2017.

[34] Stephen Buchner, Dale McMorrow, Nicholas Roche, Laurent Dusseau, and Ron L Pease. The effects of low dose-rate ionizing radiation on the shapes of transients in the lm124 operational amplifier. IEEE Transactions on Nuclear Science, 55(6):3314–3320, 2008.

[35] CI Lee and AH Johnston. Comparison of total dose effects on micropower op-amps: bipolar and cmos. In 1998 IEEE Radiation Effects Data Workshop. NSREC 98. Workshop Record. Held in conjunction with IEEE Nuclear and Space Radiation Effects Conference (Cat. No. 98TH8385), pages 132–136. IEEE, 1998.

[36] FJ Franco, Yi Zong, and Juan A Agapito. Degradation of power bipolar operational amplifiers in a mixed neutron and gamma environment. IEEE Transactions on Nuclear Science, 54(4):982–988, 2007.

[37] Nicolas J-H Roche, Laurent Dusseau, Julien Mekki, Stephanie Perez, Jean-Roch Vaille, Yago Gonzalez Velo, Jérome Boch, Frédéric Saigné, Ronan Marec, Philippe Calvel, et al. Impact of switched dose-rate irradiation on the response of the lm124 operational amplifier to pulsed x-rays. IEEE Transactions on Nuclear Science, 58(3):960–968, 2011.

[38] FJ Franco, J Lozano, JP Santos, and JA Agapito. Degradation of instrumentation amplifiers due to the nonionizing energy loss damage. IEEE Transactions on Nuclear Science, 50(6):2433–2440, 2003.

[39] JA Agapito, JP Santos, FJ Franco, J Lozano-Bahilo, AH Cachero, NP Barradas, A Paz, P Gomes, A Fernandes, IC Gonçalves, et al. Radiation tests on commercial instrumentation amplifiers, analog switches & dac's. 2001.

[40] A Privat, PW Davis, HJ Barnaby, and PC Adell. Total dose effects on negative and positive low-dropout linear regulators. IEEE Transactions on Nuclear Science, 67(7):1332–1338, 2020.

[41] J Beaucour, T Carriere, A Gach, and D Laxague. Total dose effects on negative voltage regulator. IEEE transactions on nuclear science, 41(6):2420–2426, 1994.

[42] V Ramachandran, B Narasimham, DM Fleetwood, RD Schrimpf, WT Holman, AF Witulski, RL Pease, GW Dunham, JE Seiler, and DG Platteter. Modeling total-dose effects for a low-dropout voltage regulator. IEEE transactions on nuclear science, 53(6):3223–3231, 2006.

[43] Jiri Hofman, Richard Sharp, and Jiri Haze. In-situ measurement of total ionising dose induced degradation of various commercial voltage references. In 2016 16th European Conference on Radiation and Its Effects on Components and Systems (RADECS), pages 1–4. IEEE, 2016.

[44] FJ Franco, Y Zong, JA Agapito, and AH Cachero. Radiation effects on xfet voltage references. In IEEE Radiation Effects Data Workshop, 2005., pages 138–143. IEEE, 2005.

[45] Boubekeur Tala-Ighil, J-L Trolet, Hamid Gualous, P Mary, and Stéphane Lefebvre. Experimental and comparative study of gamma radiation effects on si-igbt and sic-jfet. Microelectronics Reliability, 55(9-10):1512–1516, 2015.

[46] M Marceau, C Brisset, and M Da Costa. Study of dose effects on igbt-type devices subjected to gamma irradiation. IEEE Transactions on Nuclear Science, 46(6):1680–1685, 1999.

[47] Young Hwan Lho, Sang Yong Lee, and Phil-Hyun Kang. Radiation effects on igbt under γ irradiation. In 2007 International Conference on Control, Automation and Systems, pages 893–896. IEEE, 2007.

[48] Rudy Ferraro, Panagiotis Gkountoumis, Gilles Foucard, Antonio Ventura, Antonio Scialdone, Alessandro Zimmaro, Bruno Glecer, Sokratis Koseoglou, Cai Arcos Botias, Alessandro Masi, et al. 2023 compendium of radiation-induced effects for candidate particle accelerator. In 2023 IEEE Radiation Effects Data Workshop (REDW)(in conjunction with 2023 NSREC), pages 1–8. IEEE, 2023.

[49] Zheng Yuzhan, Lu Wu, Ren Diyuan, and Guo Qi. A new accelerated method for evaluating the eldrs of bipolar operational amplifiers: Temperature switching approach. In 2013 14th European Conference on Radiation and Its Effects on Components and Systems (RADECS), pages 1–4. IEEE, 2013.

[50] Adam Thornton. CHARM Facility Test Area Radiation Field Description. 2016.

[51] J. Mekki, M. Brugger, R. G. Alia, A. Thornton, N. C. Dos Santos Mota, and S. Danzeca. Charm: A mixed field facility at cern for radiation tests in ground, atmospheric, space and accelerator representative environments. IEEE Transactions on Nuclear Science, 63(4):2106–2114, 2016.

[52] Fabio Pozzi, Ruben Garcia Alia, Markus Brugger, Pierre Carbonez, Salvatore Danzeca, Blerina Gkotse, Martin Richard Jaekel, Federico Ravotti, Marco Silari,

and Maris Tali. Cern irradiation facilities. Radiation protection dosimetry, 180(1-4):120–124, 2018.

[53] Rudy Ferraro, Gilles Foucard, Angelo Infantino, Luigi Dilillo, Markus Brugger, Alessandro Masi, Rubén García Alía, and Salvatore Danzeca. Cots optocoupler radiation qualification process for lhc applications based on mixed-field irradiations. IEEE Transactions on Nuclear Science, 67(7):1395–1403, 2020.